Design, Modeling, and Power Electronic Control for Transient Stabilization of Power Grids Using Flywheel Energy Storage Systems

Submitted in partial fulfillment of the requirements for

the degree of

Doctor of Philosophy

in

Electrical & Computer Engineering

Kevin D. Bachovchin

B.S., Electrical & Computer Engineering, Carnegie Mellon University
M.S., Electrical & Computer Engineering, Carnegie Mellon University

Carnegie Mellon University
Pittsburgh, PA

August 2015

Acknowledgements

I express my sincere gratitude to my advisors, Professor Marija Ilic and Professor James Hoburg, for their time and guidance. I began doing research for Professor Hoburg as an undergraduate, and I thank him for making me interested in electromagnetics and in pursuing a doctorate degree. I thank Professor Ilic for her enormous passion in power systems, and I appreciate her helping me find a suitable and interesting dissertation topic given my different background and experience from most of the students in her group. I am also grateful to my other thesis committee members, Ray Beach, Vaibhav Donde, and Professor Erik Ydstie, for their valuable feedback during my thesis proposal and during other interactions.

Furthermore, I would also like to thank my colleagues and friends in the Carnegie Mellon Electric Energy Systems Group. It was a very rewarding experience to be part of such a diverse and interactive group, and I learned a lot from them. I am especially grateful to Milos Cvetkovic for his valuable help with power system modeling and control. I also would like to specifically thank Xia Miao and Ping Luo for being great officemates and friends.

Finally, I offer my enormous gratitude to my family and dedicate my thesis to them for everything they have done for me. I thank my wonderful wife Elaine for all the enjoyable times we have shared together. I also thank my parents for their endless support and advice throughout my life, which made it possible for me to pursue my goals. I cannot imagine anyone having better parents or a better wife.

Abstract

There is much interest in implementing more wind power plants in future electric energy systems. However, because wind power is unpredictable and difficult to control, large sudden disturbances in wind power generation can cause high deviations in frequency and voltage or even transient instabilities. To address these concerns, one possible solution is to add fast energy storage, such as flywheel energy storage systems. Flywheels can respond faster than conventional generators and could stabilize the system until slower generators can respond.

The following approach for transient stabilization using flywheels is proposed. First, the dynamic model for the interconnected system is obtained so that control using the flywheel can be designed and tested for provable performance. Next, flywheels are placed at each bus with wind generators, which are the potential disturbance locations. Then, a variable speed drive controller for flywheels is designed using time-scale separation and nonlinear passivity-based control logic. Switches in the power electronics interfacing between the flywheel and the rest of the power grid are controlled in order to regulate both the flywheel speed and the power electronic currents. The controller set points are chosen so that the flywheel absorbs the wind power disturbance and the rest of the system is minimally affected. Finally, the power electronics are sized to ensure that the flywheel can handle a certain range of disturbances.

Due to the complex nature of large interconnected power systems, automated methods are implemented for both the modeling and control of power systems. An automated approach is presented for symbolically deriving the dynamic model of power systems using the Lagrangian formulation from classical mechanics, where the model is described in terms of the energy functions of the system. Another automated method is introduced for symbolically deriving the control law using passivity-based control, where the control law is derived from desired closed-loop energy functions.

Finally, in the actual implementation of flywheels, one major design challenge is to support the high speed rotor. A passive magnetic bearing design is presented and the resultant magnetic fields and forces are computed, demonstrating that stable levitation of the flywheel in all directions is achieved.

Table of Contents

List of Tables

List of Figures

1. Introduction

1.1. Thesis Motivation

There is much interest in replacing conventional generators, such as coal and nuclear power plants, with wind power plants and other renewable energy sources in future electric power systems. Renewable energy sources have the potential to reduce greenhouse gas emissions and reduce the consumption of fossil fuels [1]. However, because wind power is difficult to predict and control, there are concerns that large sudden disturbances in wind power generation could cause negative impacts on the power system, such as transient instabilities, high deviations in frequency and voltage, frequent service interruptions, and wear and tear on generators.

Furthermore, wind generators typically have less inertia than conventional generators and have smaller mechanical and electromagnetic time constants. While power systems with high-inertia machines would react very slowly and almost negligibly to fast temporary disturbances, power systems with many low-inertia wind power plants would response faster to a given disturbance and be more prone to transient instabilities [2].

1.2. State-of-the-Art Industry Practices

Current industry practices for maintaining stability during large disturbances and faults are either inefficient or do not guarantee stability. Often, in industry today, the power system is operated suboptimally in order to improve the stability margin [3]. A system operator first runs an economic dispatch optimization to maximize the social welfare using the physical limits in the system as constraints. Next, the system operator performs dynamic simulations to assess the stability for many different possible disturbances. If unstable responses are detected, the system operator runs the economic dispatch optimization again with additional constraints to ensure stability for certain disturbances [2]. The main drawback with this method is that it is very suboptimal during normal conditions.

Another industrial practice for handling large disturbances is to use Remedial Action Schemes (RAS), which reconfigure the grid topology in real-time and disconnect certain components or parts of the system

to preserve stability [4]. While the reconfigured grid topology is designed to have a new equilibrium, there is no guarantee that the system will converge to this new equilibrium. The state variables may deviate too much prior to the reconfiguration for the system to converge to the new equilibrium since the dynamics of the power system are inherently nonlinear. Other drawbacks are that more components than necessary may be disconnected and that building additional infrastructure for reconfiguration, which only is used during disturbances and faults, is very expensive and inefficient.

In industry today, conventional generators have governor control [5] and excitation control with power system stabilizers [3]. Both controllers are decentralized and respond only to their own state variables. However, drawbacks with these controllers are that they are relatively slow and can be far away from the source of the disturbance. Additionally, since these controllers are only tuned against their static worse-case grid equivalents, it is very hard to guarantee that dynamic interactions will not occur within large complex systems.

1.3. Flywheel Energy Storage Systems

An alternative solution for maintaining stability is to add fast energy storage, such as flywheel energy storage systems, along with the renewable energy sources into future power grids. A flywheel energy storage system stores mechanical energy by accelerating a rotor called the flywheel to a very high speed. The flywheel is connected to an electric machine to control its rotational speed. Flywheels can respond faster than conventional generators and could stabilize the system in response to a large disturbance until slower generators can respond. Additionally, using flywheels would reduce the wear-and-tear on generators by decreasing the amount of times the generators have to suddenly change their power output and would also allow generators to produce closer to their economically optimal power [6].

Flywheels are not an appropriate storage choice for large-scale power system applications, such as economic dispatch, because other types of storage, such as pumped hydro, have a much greater energy capacity. However, for small-scale applications, flywheels have many benefits. They are environmentally benign, and they are more efficient and have smaller time constants than most other

types of storage [7]. While chemical batteries have roughly the same time constant as flywheels, flywheels have approximately twice the lifespan of chemical batteries and, unlike chemical batteries, are not limited to a certain number of charge-discharge cycles [7]. Additionally, compared to flexible alternating current transmission systems (FACTS) devices [2], flywheels have the benefit of being able to store active power in steady-state and hence can handle longer disturbances than FACTS devices [8].

1.4. Thesis Contributions

Much previous research on the modeling and control of flywheels has been done when assuming the flywheel is a standalone device [9,10,11]. However, in practice the dynamics of the rest of the power grid are interconnected with the dynamics of the flywheel. Therefore, in order to fully assess the effectiveness of a flywheel controller in transiently stabilizing an interconnected power system in response to wind power disturbances, the dynamics of the entire power system must be considered. Additionally, it should be emphasized that nonlinear dynamics and nonlinear control are needed because large sudden wind disturbances can displace the system far enough away from equilibrium where linearized models are no longer accurate.

The following approach for transient stabilization using flywheels is proposed in this thesis. First, the nonlinear dynamic model for the interconnected power system is derived in standard state space form, so that control using the flywheel can be designed and tested for provable performance. Next, the potential disturbance locations, which are the locations with wind generators, are identified, and flywheels are placed at each of these locations. Then, nonlinear power electronic control logic for the flywheels is designed so that the flywheels absorb the wind power disturbances and the rest of the system is minimally affected. Finally, parameters for the power electronics are chosen to ensure that the flywheel can handle a certain range of disturbances.

A novel automated computer-aided method is presented in Chapter 2 for symbolically deriving the nonlinear dynamics of an interconnected power system using the Lagrangian formulation from classical mechanics where the model is derived from the physical energies of the system. With this automated

approach, the user specifies the power system topology and the code symbolically solves for the dynamics in standard state space form using the Lagrangian approach [12]. The automation of this modeling process is valuable because even for a small interconnected power system, it is a complex and tedious process to derive the state space model by hand. One advantage of the Lagrangian formulation is that it provides a unified energy-based framework for analyzing mixed energy systems [13], such as power systems, which contain coupled electrical and mechanical subsystems, and this formulation also explicitly captures the coupling between subsystems. Another advantage is that the Lagrangian formulation has been shown to be useful at the nonlinear control design stage. For the passivity-based control logic [14] used in this thesis, closed-loop energy functions with desirable properties are chosen and the control law is then derived from those closed-loop energy functions.

To improve the computational efficiency of the automated modeling of power system dynamics, an alternative modular computer-aided method, is described in Chapter 3. Using this modular approach, first the dynamics for each individual module are derived using the Lagrangian approach and expressed in a common form, and then, given the interconnection between modules, the state space model of the interconnected system is solved for in an automated manner [15].

Chapter 4 introduces a novel automated computer-aided method for symbolically deriving the control law using passivity-based control logic for electrical systems. Passivity-based control is a nonlinear control method where the control law is derived from desired closed-loop energy functions. In this automated method, the control designer specifies the original state space model, the set point equations, the desired closed-loop energy function, and the desired closed-loop dissipation function, and the automated method symbolically derives the control law [16]. Again, the automation of this process is important because deriving the control law by hand for a large system would be very tedious.

Next, a novel variable speed drive controller for flywheels is developed in Chapter 5 using time-scale separation and this automated passivity-based control logic. Switches in the power electronics are controlled in order to regulate the speed of the flywheel (and hence the energy stored in the flywheel) to a different frequency than the grid frequency. To simplify the control design and reduce the amount of

communications needed, this controller takes advantage of the natural time-scale separation between the power electronics, the electrical machine variables, and the mechanical machine variables (the power electronic dynamics are the fastest while the mechanical machine variable dynamics are the slowest) in order to design a nested three-layer controller which can regulate both the flywheel speed and the power electronic currents to desired set points [17].

It should be emphasized that the fast dynamics of the inductors and capacitors in the power electronics are included when designing the control. Much previous literature on flywheels neglects the dynamics of the power electronics and models the flywheel as an ideal power source [18,19]. However, when using flywheels for transient stabilization on a very fast time-scale, it is necessary to include the fast dynamics. Otherwise, potential instabilities on a very fast time-scale will not be captured.

Chapter 6 discusses using this flywheel variable speed drive controller for transient stabilization of an interconnected power system in response to wind power disturbances. The controller set points are chosen so that the flywheel absorbs the disturbance and the rest of the system is minimally affected [20]. Three different specific methods for choosing the set points are described and compared. Chapter 7 then examines how changing the parameters of the power electronic inductors, capacitors, and resistors will affect the control performance. Recommendations are given for sizing these components based on the size of the disturbance.

Chapter 8 demonstrates using this controller for transient stabilization of larger power systems, consisting of multiple wind generators and multiple flywheels, in response to multiple wind power disturbances. A flywheel controller is placed at each bus with one or more wind generators, and each flywheel is responsible for absorbing all the wind power disturbances on that bus so that the rest of the system is minimally affected. It should be emphasized that this is a competitive control strategy, as opposed to the cooperative control strategy pursued in [8] where a FACTS controller in one region is used to transient stabilize the system in response to a disturbance or fault in a different region. Simulation results are shown demonstrating the effectiveness of flywheels and this control logic for transient stabilization of the Sao Miguel island power system using real-world data.

Wind power disturbances are considered in this thesis because they are the most common type of disturbance in power systems, but it should noted that the flywheel variable speed drive controller could be used to transient stabilize the system in response to other types of disturbances as well. Additionally, it should be noted that while flywheels are analyzed in this thesis, most of the modeling and the control design in this thesis would be applicable to other types of fast storage as well. The Lagrangian-based modeling of the dynamics and the passivity-based control logic provide a general energy-based framework for analyzing systems with different types of energy [21].

Finally, in the actual implementation of flywheels, one major design challenge is to support the high speed rotor. It is advantageous to use magnetic bearings to support the flywheel instead of conventional mechanical bearings in order to decrease frictional energy losses. Magnetic bearings are contactless and therefore can exhibit a much higher efficiency. Most commercial magnetic bearings are active magnetic bearings, which use position sensors and electronic circuits that control electromagnets to achieve stable levitation of the rotating element. However, active magnetic bearings are more expensive than passive magnetic bearings, which do not have any sensors or control.

Therefore, in Chapter 9, a novel passive magnetic bearing design is analyzed. A significant challenge with passive magnetic bearings results from Earnshaw's Theorem, which states that it is not possible to stably levitate an object in all directions using any configuration of only permanent magnets. To overcome this problem, a Halbach array stabilizer, which induces currents in stabilization coils, is added to the levitation magnet system. The resultant magnetic fields and forces of the magnetic bearing system are computed using electromagnetic theory, demonstrating that stable levitation of the flywheel in all directions is achieved with this design [22,23,24].

2. Automated Energy-Based Modeling of Power System Dynamics

In order to design control logic using flywheels and test the control for provable performance, it is necessary to first obtain the dynamic model of the power system. Nonlinear dynamics and nonlinear control are needed because large wind disturbances can displace the system far enough away from the equilibrium where linearized models are no longer accurate. For large interconnected power systems components, it can be a very tedious and lengthy process to obtain the state space model for the system. For this reason, a new automated approach was implemented for symbolically deriving the state space model of general power systems, given the power system topology, using the Lagrangian formulation from classical mechanics [12,25].

Lagrangian mechanics and Hamiltonian mechanics are re-formulations of classical Newtonian mechanics [26]. While the dynamic equations of motion in Newtonian mechanics are derived from forces, the equations of motion in Lagrangian and Hamiltonian mechanics are derived from the potential and kinetic energies of the system. While the Lagrangian and Hamiltonian formulations were originally developed for mechanical systems, they can also be applied to other types of systems, as well to mixed energy systems, such as power systems, which contain coupled electrical and mechanical subsystems [21].

There are two main advantages to using the Lagrangian or Hamiltonian formulation for deriving the dynamics. First, these formulations provide a unified energy-based framework for analyzing differently subsystems in mixed energy systems and explicitly capture the coupling between subsystems. Second, in the passivity-based control described in Chapter 4, desired closed-loop energy functions are chosen, and it is necessary to derive the resulting error dynamics from those closed-loop energy functions in order to derive the control law.

When applying the Lagrangian and Hamiltonian formulations to electrical systems or subsystems, the magnetic energy stored in inductors is analogous to the kinetic energy for mechanical systems, and the electric energy stored in capacitors is analogous to the potential energy for mechanical systems [21]. The Lagrangian and Hamiltonian approaches are equivalent, but the electrical state variables resulting from

7

the Lagrangian approach are the capacitor charges and the inductor currents while the electrical state variables that arise from the Hamiltonian approach are the capacitor charges and the inductor fluxes. In [27], automated methods were introduced for deriving the dynamic equations of electric circuits using each formulation, and the Lagrangian formulation was shown to be more computationally efficient than the Hamiltonian formulation. This is because the Hamiltonian approach requires the inductance matrix of the system to be inverted and the constraints for circuits, as well as for power systems, are fundamentally in terms of currents, not fluxes [27]. Hence, the Lagrangian formulation is used in this thesis.

In this chapter, it is first described how the Lagrangian formulation is applied to electrical systems. Then, it is demonstrated how the Lagrangian formulation is applied to electromechanical systems, such as power systems.

2.1. Lagrangian Formulation Applied to Electrical Systems

Much previous literature describes applying the Lagrangian formulation to electric circuits [13,28,29]. Extending this previous work, a novel automated computer-aided method is described in this section for symbolically deriving the dynamic equations in standard state space form of an electric circuit using the Lagrangian formulation, given user input about the circuit topology. It should be noted that many existing circuit simulators, such as CADENCE Design Systems, SPICE, and PSPICE [30], can simulate the behavior of a circuit but do not return the state space model of a circuit. Hence, these tools cannot be used for control design with provable performance.

This automated method is demonstrated for deriving the state space model of an ac/dc/ac converter. Control for this converter will then be developed in Section 4.2 using passivity-based control logic. Ac/dc/ac converters are widely used and proposed in variable speed drives for flywheel energy storage systems [31,32,33,34].

2.1.1. Automated State Space Model Derivation Methodology

The automated method was first introduced in [27] for deriving the state space equations for linear electric circuits with any number of voltages sources, resistors, capacitors, and inductors, as well as

mutual inductance between inductors. The automated approach was then extended to include power electronic circuits with switches in [16]. This automated method uses the internal MATLAB 'syms' and 'solve' commands in order to symbolically solve for the dynamic equations in standard state space form given user input about the circuit topology.

It should be emphasized that the automated method expresses the dynamics in standard state space form as an ODE (ordinary differential equation) system. In order to do this, logic is implemented in the automated methods to check for all-inductor cutsets, which occur when one of the inductor currents can be expressed as a linear combination of the other inductor currents, and all-capacitor loops, which occur when one of the capacitor charges can be expressed as a linear combination of the other capacitor charges. When there are all-inductor cutsets or all-capacitor loops, the dynamics will initially be a DAE (differential algebraic equation) system. In order to convert the DAE system to an ODE system, the automated method eliminates one of the inductor currents in each all-inductor cutset and one of the capacitor charges in each all-capacitor loop using the algebraic relationships.

It is desired to express the dynamics in standard state space form as an ODE system because this is the only form directly useful for applying many existing control techniques [35], such as Linear-Quadratic Regulator (LQR) control [36]. Also, standard state space form is needed for checking whether the system is fully observable and fully controllable, as well as for deciding the placement of sensors for control design [35]. Additionally, simulating DAEs with an index greater than one is very difficult, as discussed in [37].

For the automated method, the user should take the following steps to provide information about the circuit topology:

1. For each of the B branches of the circuit, label and define the directions of the currents. A branch is defined as a continuous path where the same current must flow. (The charge q_k on each branch is defined by $dq_k / dt = i_k$.)

2. For a circuit with *J* junctions, choose one arbitrary junction to be ground and label the voltages at the other *J*-1 junctions as λ_1, λ_2,…, λ_{J-1}. (These junction voltages are the Lagrange multipliers when applying the Lagrangian equation.)   A junction is defined as the intersection of three or more branches. Write Kirchhoff's current law (KCL) equations at the non-ground junctions starting with the junction labeled λ_1 and ending with the junction labeled λ_{J-1}. Use the following convention when writing the KCL equations:

$$-\sum i_{\text{into junction}} + \sum i_{\text{out of junction}} = 0 \tag{2.1}$$

For a power electronic circuit with switches, the KCL equations are a function of the control inputs (switch positions) [14].

3. Define all parameters and controllable inputs, as well as all the charges and currents on each branch, as MATLAB 'syms' (symbolic objects).

4. Form *B*x1 symbolic vectors for the current **I** and the charge **Q** consisting of the symbolic currents and charges on the individual branches.

5. Form 1x*B* symbolic vectors for the capacitance vector **C**, the resistance vector **R**, and the voltage source vector **V**, consisting respectively of the capacitances, resistances, and voltage sources on each branch. (For the voltage source vector, if the direction of the current is such that it leaves the positive terminal of the voltage source, then the sign is positive. Otherwise, the sign is negative.)

6. Form a *B*x*B* symbolic matrix for the inductance matrix **L** where the self-inductances of each branch are given on the diagonal entries of the matrix and the mutual inductance between branches are given on the off-diagonal entries of the matrix.

7. Form the constraint matrix **G**, which is a (*J*-1)x*B* matrix. $\mathbf{GI} = 0$ gives the KCL equations. For a power electronic circuit with switches, **G** will be a function of the switch positions.

8. Form the Lagrange multiplier **Λ** vector, which is a 1x(*J*-1) symbolic vector, consisting of the voltages at the *J*-1 non-ground junctions.

Given the circuit topology defined by the matrices $\mathbf{I}$, $\mathbf{Q}$, $\mathbf{C}$, $\mathbf{R}$, $\mathbf{V}$, $\mathbf{L}$, $\mathbf{G}$, and $\mathbf{\Lambda}$, the computer solves for the dynamic equations by taking the following steps:

1. Find the total magnetic co-energy $W_m{'}$ stored in the inductors of the circuit, which is

$$W_m{'} = \frac{1}{2}\mathbf{I}^T\mathbf{L}\mathbf{I} \tag{2.2}$$

For an electrically linear system, the magnetic energy is numerically equal to the magnetic co-energy, although the magnetic energy is expressed in terms of fluxes while the magnetic co-energy is expressed in terms of currents [38].

2. Find the total electric energy W_e stored in the capacitors of the circuit, which is

$$W_e = \sum_{1 \le k \le B, \mathbf{C}(k) \ne 0} \frac{1}{2}\frac{\mathbf{Q}(k)^2}{\mathbf{C}(k)} \tag{2.3}$$

It is important to do the summation for only those branches containing a capacitor to avoid dividing by zero.

3. Find the Lagrangian $\mathcal{L}$, which is

$$\mathcal{L} = W_m{'} - W_e \tag{2.4}$$

4. Find the Rayleigh dissipation function $\mathcal{R}$, which is

$$\mathcal{R} = \sum_{k=1}^{B} \frac{1}{2}\mathbf{R}(k)\mathbf{I}(k)^2 \tag{2.5}$$

5. Form the Lagrange equations of the first kind [28]

$$\frac{d}{dt}\left[\frac{\partial\mathcal{L}}{\partial\mathbf{I}(k)}\right] - \frac{\partial\mathcal{L}}{\partial\mathbf{Q}(k)} + \frac{\partial\mathcal{R}}{\partial\mathbf{I}(k)} - \mathbf{V}(k) - \frac{\partial\mathbf{\Lambda}\mathbf{G}\mathbf{I}}{\partial\mathbf{I}(k)} = 0 \qquad \text{for } k = 1, 2, \ldots B \tag{2.6}$$

The Lagrange equations for electric systems specify that the voltage across each branch must be equal to the difference between the two junction voltages adjacent to that branch. The first, second, and third terms of (2.6) are the voltage drops across the inductors, capacitors, and resistors of branch k respectively. The fourth term contains the voltage sources on branch k, and the fifth term is the voltage difference between the connecting junctions adjacent to branch k.

The benefit of using the Lagrange equations rather than the conventional Kirchhoff's voltage law (KVL) equations is that in the passivity-based control described in Chapter 4, closed-loop energy functions with desirable properties are chosen. The Lagrange equations are used to derive the resulting error dynamics and then the control law from those closed-loop energy functions. This would not be possible using the KVL equations.

6. Add the KCL equations, $\mathbf{GI} = 0$, to these equations in order to form the initial set of equations.

7. For branches containing both a capacitor and an inductor, add another equation to the system:

$dq_k / dt = i_k$.

8. For branches containing a capacitor but not an inductor, substitute in dq_k / dt for i_k.

At this point, there are $B+J\text{-}1+B_{both}$ equations and $B_{none}+2B_{ind}+2B_{cap}+4B_{both}+J\text{-}1$ unknowns where B_{none} is the number of branches with neither an inductor nor a capacitor, B_{ind} is the number of branches with an inductor but not a capacitor, B_{cap} is the number of branches with a capacitor but not an inductor, and B_{both} is the number of branches with both a capacitor and an inductor. The unknowns are the voltages at the non-ground junctions, the currents in branches containing neither an inductor nor a capacitor, the currents and the derivatives of currents in branches containing only an inductor, the charges and the derivatives of charges in branches containing only a capacitor, and the currents, the derivative of the currents, the charges, and the derivative of the charges in branches containing both an inductor and a capacitor. There are $B_{ind}+B_{cap}+2B_{both}$ (the number of storage devices) more unknowns than equations.

If there are no all-inductor cutsets or all-capacitor loops, using the MATLAB 'solve' function, the $B_{ind}+B_{cap}+2B_{both}$ derivatives of the state variables, as well as the $J\text{-}1$ λ's and the B_{none} currents, can be solved for in terms of the $B_{ind}+B_{cap}+2B_{both}$ state variables. However, if there are all-inductor cutsets or all-capacitor loops, the 'solve' function will produce a warning saying that no explicit solution can be found. Therefore, all-inductor cutsets and all-capacitor loops must be checked for before using the 'solve' function.

9. Check for any all-inductor cutsets. An all-inductor cutset occurs when one of the inductor currents is dependent and can be expressed as a linear combination of the other inductor currents. It is not sufficient to merely check for all-inductor cutsets at the J-1 junctions where the KCL equations were written. It is possible there could be an algebraic relationship between inductor currents at the ground junction or at a supernode. For a circuit with J junctions, there are 2^J-2 possible KCL equations that can be written [39], J-1 of which are independent. Half of these possible KCL equations are just negatives of each other, so it is necessary to check $(2^J$-2$)/2$ KCL equations for an all-inductor cutset. For each of these KCL equations, an all-inductor cutset occurs when all branches in the KCL equation contain an inductor.

If there is an all-inductor cutset, a current must be substituted by an expression in terms of the other currents in the all-inductor cutset. Also, the derivative of that current must be substituted by the derivative of that expression. Finally, the proper KCL equation must be eliminated from the system of equations.

10. Check for any all-capacitor loops. An all-capacitor loop occurs when one of the capacitor charges is dependent and can be expressed as a linear combination of the other capacitor charges. All possible KVL equations in the circuit (excluding ones that are merely negatives of each other) must be checked. For each of these KVL equations, an all-capacitor loop occurs when all branches in the loop contain only a capacitor or a voltage source (not an inductor or a resistor).

If there is an all-capacitor loop, a charge must be substituted by an expression in terms of the other charges and voltages sources in the loop. Also, the derivative of that charge must be substituted by the derivative of that expression as well. Finally, the Lagrange equation for the branch whose charge was substituted for must be eliminated from the system of equations.

11. At this point, there are $B+J$-1$+B_{both}$-D equations and $B_{none}+2B_{ind}+2B_{cap}+4B_{both}+J$-1-2$D$ unknowns where D is the number of dependent storage devices. There are $B_{ind}+B_{cap}+2B_{both}$-$D$ (the number of independent storage devices) more unknowns than equations.

13

To solve for the state space model, the derivatives of the state variables need to be expressed in terms of only the state variables (not the λ's or the currents in branches with no storage devices). Therefore, the MATLAB 'solve' function is used to symbolically solve for the $B_{ind}+B_{cap}+2B_{both}$-$D$ derivatives of the state variables, as well as the J-1 λ's and the B_{none} currents, in terms of the $B_{ind}+B_{cap}+2B_{both}$-$D$ state variables. The solution returned by the MATLAB 'solve' function is in the general state space form:

$$\dot{\mathbf{x}} = \mathbf{f}(x,u) \tag{2.7}$$

where $\mathbf{x}$ is the vector of state variables and $\mathbf{u}$ is the vector of controllable inputs. The state variables are the independent inductor currents and the independent capacitors charges.

2.1.2.   Example: AC/DC/AC Converter

As an example for the automated modeling methodology, consider the three-phase ac/dc/ac (alternating current/direct current/alternating current) converter shown in Figure 2.1. There is a three-phase voltage source at a constant frequency ω_1 on the left side of the converter, a dc-link capacitor in the middle, and a three-phase constant resistance and inductance load on the right side. The objective of the ac/dc/ac converter is to regulate the currents through the load to desired values at a different frequency than the voltage source. The controllable inputs are the positions of the twelve switches. For each of the six switch pairs, the control is designed so that, at any given time, either the top switch or the bottom switch is closed, but not both. The switching functions $u_{1a}, u_{1b}, u_{1c}, u_{2a}, u_{2b},$ and u_{2c} are defined as

$$u_{ik} = \begin{cases} 1 & S_{ik} \text{ closed} \\ -1 & \overline{S}_{ik} \text{ closed} \end{cases} \quad i=1,2 \ ; \ k=a,b,c \tag{2.8}$$

14
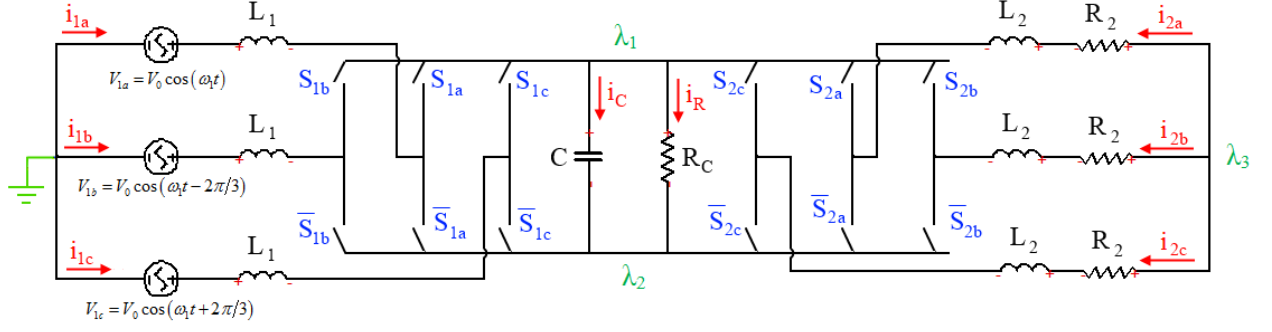
Figure 2.1: Circuit topology for ac/dc/ac converter.

Following the automated modeling methodology, first the currents are labeled on each of the eight branches of the circuit as shown in Figure 2.1. There are four junctions in the circuit. The left junction is chosen to be ground and the voltages at the other three junctions are labeled as shown in Figure 2.1. Using the convention in (2.1), the KCL equations at the three non-ground junctions are

$$\frac{-(1+u_{1a})}{2}i_{1a} - \frac{(1+u_{1b})}{2}i_{1b} - \frac{(1+u_{1c})}{2}i_{1c} + i_C + i_R - \frac{(1+u_{2a})}{2}i_{2a} - \frac{(1+u_{2b})}{2}i_{2b} - \frac{(1+u_{2c})}{2}i_{2c} = 0 \quad (2.9)$$

$$\frac{-(1-u_{1a})}{2}i_{1a} - \frac{(1-u_{1b})}{2}i_{1b} - \frac{(1-u_{1c})}{2}i_{1c} - i_C - i_R - \frac{(1-u_{2a})}{2}i_{2a} - \frac{(1-u_{2b})}{2}i_{2b} - \frac{(1-u_{2c})}{2}i_{2c} = 0 \quad (2.10)$$

$$i_{2a} + i_{2b} + i_{2c} = 0 \quad (2.11)$$

After defining all parameters, switching functions, currents, and charges as symbolic objects, the symbolic vectors **I** and **Q** are defined as

$$\mathbf{I} = \begin{bmatrix} i_{1a} & i_{1b} & i_{1c} & i_C & i_R & i_{2a} & i_{2b} & i_{2c} \end{bmatrix}^T \quad (2.12)$$

$$\mathbf{Q} = \begin{bmatrix} q_{1a} & q_{1b} & q_{1c} & q_C & q_R & q_{2a} & q_{2b} & q_{2c} \end{bmatrix}^T \quad (2.13)$$

The inductance matrix **L**, the capacitance vector **C**, the resistance vector **R**, and the voltage source vector **V** are defined as

$$\mathbf{L} = \begin{bmatrix}
L_1 & 0 & 0 & 0 & 0 & 0 & 0 & 0 \\
0 & L_1 & 0 & 0 & 0 & 0 & 0 & 0 \\
0 & 0 & L_1 & 0 & 0 & 0 & 0 & 0 \\
0 & 0 & 0 & 0 & 0 & 0 & 0 & 0 \\
0 & 0 & 0 & 0 & 0 & 0 & 0 & 0 \\
0 & 0 & 0 & 0 & 0 & L_2 & 0 & 0 \\
0 & 0 & 0 & 0 & 0 & 0 & L_2 & 0 \\
0 & 0 & 0 & 0 & 0 & 0 & 0 & L_2
\end{bmatrix} \quad (2.14)$$

15

$$\mathbf{C} = \begin{bmatrix} 0 & 0 & 0 & C & 0 & 0 & 0 & 0 \end{bmatrix} \tag{2.15}$$

$$\mathbf{R} = \begin{bmatrix} 0 & 0 & 0 & 0 & R_C & R_2 & R_2 & R_2 \end{bmatrix} \tag{2.16}$$

$$\mathbf{V} = \begin{bmatrix} V_{1a} & V_{1b} & V_{1c} & 0 & 0 & 0 & 0 & 0 \end{bmatrix} \tag{2.17}$$

The constraint matrix $\mathbf{G}$, which when multiplied by $\mathbf{I}$ yields the KCL equations, is

$$\mathbf{G} = \begin{bmatrix} -(1+u_{1a})/2 & -(1+u_{1b})/2 & -(1+u_{1c})/2 & 1 & 1 & -(1+u_{2a})/2 & -(1+u_{2b})/2 & -(1+u_{2c})/2 \\ -(1-u_{1a})/2 & -(1-u_{1b})/2 & -(1-u_{1c})/2 & -1 & -1 & -(1-u_{2a})/2 & -(1-u_{2b})/2 & -(1-u_{2c})/2 \\ 0 & 0 & 0 & 0 & 0 & 1 & 1 & 1 \end{bmatrix} \tag{2.18}$$

The Lagrange multiplier matrix $\mathbf{\Lambda}$, which contains the voltages at the three non-ground nodes, is

$$\mathbf{\Lambda} = \begin{bmatrix} \lambda_1 & \lambda_2 & \lambda_3 \end{bmatrix} \tag{2.19}$$

Given the circuit topology defined by the matrices $\mathbf{I}$, $\mathbf{Q}$, $\mathbf{L}$, $\mathbf{C}$, $\mathbf{R}$, $\mathbf{V}$, $\mathbf{G}$, and $\mathbf{\Lambda}$, the automated method solves for the dynamic equations using the Lagrangian formulation following the steps below.

The magnetic co-energy stored in the six inductors is

$$W_m' = \frac{1}{2} L_1 \left(i_{1a}^2 + i_{1b}^2 + i_{1c}^2 \right) + \frac{1}{2} L_2 \left(i_{2a}^2 + i_{2b}^2 + i_{2c}^2 \right) \tag{2.20}$$

The electric energy stored in the capacitor is

$$W_e = \frac{1}{2} \frac{q_C^2}{C} \tag{2.21}$$

The Lagrangian is

$$\mathscr{L} = W_m' - W_e = \frac{1}{2} L_1 \left(i_{1a}^2 + i_{1b}^2 + i_{1c}^2 \right) + \frac{1}{2} L_2 \left(i_{2a}^2 + i_{2b}^2 + i_{2c}^2 \right) - \frac{1}{2} \frac{q_C^2}{C} \tag{2.22}$$

The Rayleigh dissipation function is

$$\mathscr{R} = \frac{1}{2} R_2 \left(i_{2a}^2 + i_{2b}^2 + i_{2c}^2 \right) + \frac{1}{2} R_C i_R^2 \tag{2.23}$$

The Lagrangian equations from evaluating (2.6) are

$$\lambda_1 (1+u_{1a})/2 - V_{1a} + \lambda_2 (1-u_{1a})/2 + L_1 \frac{di_{1a}}{dt} = 0 \tag{2.24}$$

16

$$\lambda_1(1+u_{1b})/2 - V_{1b} + \lambda_2(1-u_{1b})/2 + L_1\frac{di_{1b}}{dt} = 0 \tag{2.25}$$

$$\lambda_1(1+u_{1c})/2 - V_{1c} + \lambda_2(1-u_{1c})/2 + L_1\frac{di_{1c}}{dt} = 0 \tag{2.26}$$

$$\lambda_2 - \lambda_1 + \frac{q_C}{C} = 0 \tag{2.27}$$

$$\lambda_2 - \lambda_1 + R_C i_R = 0 \tag{2.28}$$

$$\lambda_1(1+u_{2a})/2 - \lambda_3 + \lambda_2(1-u_{2a})/2 + L_2\frac{di_{2a}}{dt} + R_2 i_{2a} = 0 \tag{2.29}$$

$$\lambda_1(1+u_{2b})/2 - \lambda_3 + \lambda_2(1-u_{2b})/2 + L_2\frac{di_{2b}}{dt} + R_2 i_{2b} = 0 \tag{2.30}$$

$$\lambda_1(1+u_{2c})/2 - \lambda_3 + \lambda_2(1-u_{2c})/2 + L_2\frac{di_{2c}}{dt} + R_2 i_{2c} = 0 \tag{2.31}$$

Equations (2.24)-(2.31) and the KCL equations (2.9)-(2.11) form the initial system of equations. There are no branches with both an inductor and a capacitor, but there is one branch with a capacitor but not an inductor. Therefore, i_C is replaced by dq_C/dt in (2.9)-(2.11)and (2.24)-(2.31). There are no all-capacitor loops, but there are two all-inductor cutsets. KCL equation (2.11) forms an all-inductor cutset so i_{2c} is replaced by $-i_{2a} - i_{2b}$ and (2.11) is removed from the system of equations. The sum of KCL equations (2.9) and (2.10) also forms an all-inductor so i_{1c} is replaced by $-i_{1a} - i_{1b}$. Since the all-inductor cutset occurred in the sum of (2.9) and (2.10), either one could be removed from the system of equations. Equation (2.9) is chosen to be removed. After making these changes, the new system of equations is

$$\lambda_1(1+u_{1a})/2 - V_{1a} + \lambda_2(1-u_{1a})/2 + L_1\frac{di_{1a}}{dt} = 0 \tag{2.32}$$

$$\lambda_1(1+u_{1b})/2 - V_{1b} + \lambda_2(1-u_{1b})/2 + L_1\frac{di_{1b}}{dt} = 0 \tag{2.33}$$

$$\lambda_1(1+u_{1c})/2 - V_{1c} + \lambda_2(1-u_{1c})/2 - L_1\left(\frac{di_{1a}}{dt} + \frac{di_{1b}}{dt}\right) = 0 \qquad (2.34)$$

$$\lambda_2 - \lambda_1 + \frac{q_C}{C} = 0 \qquad (2.35)$$

$$\lambda_2 - \lambda_1 + R_C i_R = 0 \qquad (2.36)$$

$$\lambda_1(1+u_{2a})/2 - \lambda_3 + \lambda_2(1-u_{2a})/2 + L_2\frac{di_{2a}}{dt} + R_2 i_{2a} = 0 \qquad (2.37)$$

$$\lambda_1(1+u_{2b})/2 - \lambda_3 + \lambda_2(1-u_{2b})/2 + L_2\frac{di_{2b}}{dt} + R_2 i_{2b} = 0 \qquad (2.38)$$

$$\lambda_1(1+u_{2c})/2 - \lambda_3 + \lambda_2(1-u_{2c})/2 - L_2\left(\frac{di_{2a}}{dt} + \frac{di_{2b}}{dt}\right) - R_2\left(i_{2a} + i_{2b}\right) = 0 \qquad (2.39)$$

$$\frac{-(1-u_{1a})}{2}i_{1a} - \frac{(1-u_{1b})}{2}i_{1b} + \frac{(1-u_{1c})}{2}\left(i_{1a} + i_{1b}\right) - \frac{dq_C}{dt}$$
$$-i_R - \frac{(1-u_{2a})}{2}i_{2a} - \frac{(1-u_{2b})}{2}i_{2b} + \frac{(1-u_{2c})}{2}\left(i_{2a} + i_{2b}\right) = 0 \qquad (2.40)$$

In the new system the number of equations, $B+J-1+B_{both}-D$, is 9 while the number of unknowns, $B_{none}+2B_{ind}+2B_{cap}+4B_{both}+J-1$, is 14. (For this example $B = 8$, $B_{none} = 1$, $B_{ind} = 6$, $B_{cap} = 1$, $B_{both} = 1$, $J = 4$, and $D = 2$.) The unknowns are i_{1a}, i_{1b}, i_{2a}, i_{2b}, q_C, i_R, di_{1a}/dt, di_{1b}/dt, di_{2a}/dt, di_{2b}/dt, dq_C/dt, λ_1, λ_2, and λ_3. The MATLAB 'solve' function is used to symbolically solve for the state variable derivatives (di_{1a}/dt, di_{1b}/dt, di_{2a}/dt, di_{2b}/dt, dq_C/dt), as well as i_R, λ_1, λ_2, and λ_3 in terms of the state variables (i_{1a}, i_{1b}, i_{2a}, i_{2b}, q_C). In the standard state space form given by (2.7), the dynamic equations of the ac/dc/ac converter are

$$\frac{di_{1a}}{dt} = \frac{q_C}{6CL_1}\left(-2u_{1a} + u_{1b} + u_{1c}\right) - \frac{1}{3L_1}\left(-2V_{1a} + V_{1b} + V_{1c}\right) \qquad (2.41)$$

$$\frac{di_{1b}}{dt} = \frac{q_C}{6CL_1}\left(u_{1a} - 2u_{1b} + u_{1c}\right) - \frac{1}{3L_1}\left(V_{1a} - 2V_{1b} + V_{1c}\right) \qquad (2.42)$$

$$\frac{di_{2a}}{dt} = \frac{q_C}{6CL_2}\left(-2u_{2a} + u_{2b} + u_{2c}\right) - \frac{R_2}{L_2}i_{2a} \tag{2.43}$$

$$\frac{di_{2b}}{dt} = \frac{q_C}{6CL_2}\left(u_{2a} - 2u_{2b} + u_{2c}\right) - \frac{R_2}{L_2}i_{2b} \tag{2.44}$$

$$\frac{dq_C}{dt} = \frac{i_{1a}}{2}\left(u_{1a} - u_{1c}\right) + \frac{i_{1b}}{2}\left(u_{1b} - u_{1c}\right) + \frac{i_{2a}}{2}\left(u_{2a} - u_{2c}\right) + \frac{i_{2b}}{2}\left(u_{2b} - u_{2c}\right) - \frac{q_C}{CR_C} \tag{2.45}$$

The controllable inputs $u_{1a}, u_{1b}, u_{1c}, u_{2a}, u_{2b},$ and u_{2c} defined by (2.8) are discrete values. Since analysis of discrete control inputs is complex, one common approach is to use state space averaging [14,40,41,42]. Hence for the rest of the thesis, the switching functions $u_{1a}, u_{1b}, u_{1c}, u_{2a}, u_{2b},$ and u_{2c} are regarded as duty ratio functions with values in the interval $(-1,1)$.

2.1.3.   Transformation of Dynamic Equations to the αβ Reference Frame

The equations derived by the automated method are in the stationary three-phase *abc* reference frame. However, for power systems and three-phase power electronics, the rotating two-phase *dq* (direct-quadrature) reference frame is often used to express the dynamics of machines because this form is often simplest mathematically and most useful for control purposes [43]. Sinusoidal steady-state operation in the *abc* reference frame yields constant steady-state values in the *dq* reference frame if the *dq* reference is rotating at the same speed as the sinusoidal steady-state frequency. Therefore, it is important to extend the automated derivation of the dynamic equations from the *abc* reference frame to the *dq* reference frame.

First, the transformation of the equations to the stationary two-phase αβ reference frame is described, and then in the next section the transformation of equations to the rotating *dq* reference frame is described. Any system with three or more stationary phases can be equivalently modeled as two stationary phases [44,45]. The graphical interpretation of the *abc* to αβ transformation is shown in Figure 2.2 and this transformation is given by

19

$$\mathbf{x}_{\alpha\beta z} = \mathbf{T}\mathbf{x}_{abc}$$

$$\mathbf{T} = \sqrt{\frac{2}{3}} \begin{bmatrix} 1 & -\dfrac{1}{2} & -\dfrac{1}{2} \\ 0 & \dfrac{\sqrt{3}}{2} & -\dfrac{\sqrt{3}}{2} \\ \dfrac{1}{\sqrt{2}} & \dfrac{1}{\sqrt{2}} & \dfrac{1}{\sqrt{2}} \end{bmatrix}$$

(2.46)

The z-phase is independent of the α and β phases and is only used in order to make $\mathbf{T}$ invertible. If the three phases of the system are balanced, then the a, b, and c phases sum to zero at all times, and the z phase is always zero [45].
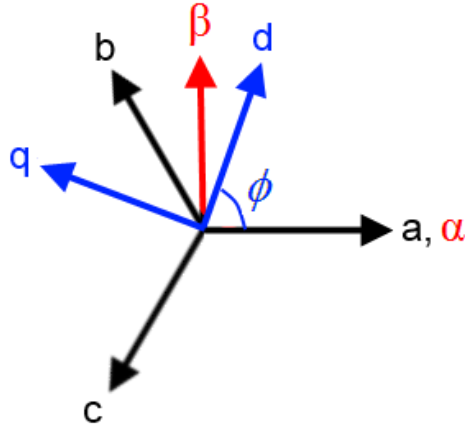
Figure 2.2: Graphical interpretation of the $\alpha\beta$ and dq transformations.

When the c phase is dependent due to an all-inductor cutset and is replaced as the negative sum of the a and b phases (as is the case for i_{1c} and i_{2c} in the ac/dc/ac converter), transformation (2.46) reduces to

$$\mathbf{x}_{\alpha\beta} = \mathbf{T}_{red}\mathbf{x}_{ab}$$

$$\mathbf{T}_{red} = \begin{bmatrix} \sqrt{\dfrac{2}{3}} + \dfrac{1}{\sqrt{6}} & 0 \\ \dfrac{1}{\sqrt{2}} & \sqrt{2} \end{bmatrix}$$

(2.47)

For the ac/dc/ac converter, the dynamic equations (2.41)-(2.45) can be re-written in matrix form as

$$
\begin{bmatrix} \dot{\mathbf{i}}_{1ab} \\ \dot{\mathbf{i}}_{2ab} \\ \dot{q}_C \end{bmatrix} = \begin{bmatrix} \mathbf{f}_1(\mathbf{V}_{1abc}, \mathbf{u}_{1abc}) \\ \mathbf{f}_2(\mathbf{u}_{2abc}, \mathbf{i}_{2ab}) \\ f_3(\mathbf{u}_{1abc}, \mathbf{u}_{2abc}, \mathbf{i}_{1ab}, \mathbf{i}_{2ab}) \end{bmatrix}
$$

$$
\mathbf{V}_{1abc} = \begin{bmatrix} V_{1a} & V_{1b} & V_{1c} \end{bmatrix}^T
$$

$$
\mathbf{u}_{1abc} = \begin{bmatrix} u_{1a} & u_{1b} & u_{1c} \end{bmatrix}^T
$$

$$
\mathbf{u}_{2abc} = \begin{bmatrix} u_{2a} & u_{2b} & u_{2c} \end{bmatrix}^T \tag{2.48}
$$

$$
\mathbf{i}_{1ab} = \begin{bmatrix} i_{1a} & i_{1b} \end{bmatrix}^T
$$

$$
\mathbf{i}_{2ab} = \begin{bmatrix} i_{2a} & i_{2b} \end{bmatrix}^T
$$

To obtain the differential equations in the αβ reference frame, first the expressions for the derivatives of $\mathbf{i}_{1\alpha\beta}$ and $\mathbf{i}_{2\alpha\beta}$ are found in terms of the *abc* quantities.

$$
\begin{bmatrix} \dot{\mathbf{i}}_{1\alpha\beta} \\ \dot{\mathbf{i}}_{2\alpha\beta} \\ \dot{q}_C \end{bmatrix} = \begin{bmatrix} \mathbf{T}_{red}\mathbf{f}_1(\mathbf{V}_{1abc}, \mathbf{u}_{1abc}) \\ \mathbf{T}_{red}\mathbf{f}_2(\mathbf{u}_{2abc}, \mathbf{i}_{2ab}) \\ f_3(\mathbf{u}_{1abc}, \mathbf{u}_{2abc}, \mathbf{i}_{1ab}, \mathbf{i}_{2ab}) \end{bmatrix}
$$

$$
\mathbf{i}_{1\alpha\beta} = \begin{bmatrix} i_{1\alpha} & i_{1\beta} \end{bmatrix}^T \tag{2.49}
$$

$$
\mathbf{i}_{2\alpha\beta} = \begin{bmatrix} i_{2\alpha} & i_{2\beta} \end{bmatrix}^T
$$

Next, to find the expressions for the derivatives of $\mathbf{i}_{1\alpha\beta}$ and $\mathbf{i}_{2\alpha\beta}$ in terms of the αβ quantities, the MATLAB 'subs' command is used to substitute the *abc* quantities in terms of the αβ quantities.

$$
\begin{bmatrix} \dot{\mathbf{i}}_{1\alpha\beta} \\ \dot{\mathbf{i}}_{2\alpha\beta} \\ \dot{q}_C \end{bmatrix} = \begin{bmatrix} \mathbf{T}_{red}\mathbf{f}_1(\mathbf{T}^{-1}\mathbf{V}_{1\alpha\beta z}, \mathbf{T}^{-1}\mathbf{u}_{1\alpha\beta z}) \\ \mathbf{T}_{red}\mathbf{f}_2(\mathbf{T}^{-1}\mathbf{u}_{2\alpha\beta z}, \mathbf{T}_{red}^{-1}\mathbf{i}_{2\alpha\beta}) \\ f_3(\mathbf{T}^{-1}\mathbf{u}_{1\alpha\beta z}, \mathbf{T}^{-1}\mathbf{u}_{2\alpha\beta z}, \mathbf{T}_{red}^{-1}\mathbf{i}_{1\alpha\beta}, \mathbf{T}_{red}^{-1}\mathbf{i}_{2\alpha\beta}) \end{bmatrix}
$$

$$
\mathbf{V}_{1\alpha\beta z} = \begin{bmatrix} V_{1\alpha} & V_{1\beta} & V_{1z} \end{bmatrix}^T
$$

$$
\mathbf{u}_{1\alpha\beta z} = \begin{bmatrix} u_{1\alpha} & u_{1\beta} & u_{1z} \end{bmatrix}^T
$$

$$
\mathbf{u}_{2\alpha\beta z} = \begin{bmatrix} u_{2\alpha} & u_{2\beta} & u_{2z} \end{bmatrix}^T \tag{2.50}
$$

$$
\mathbf{i}_{1\alpha\beta} = \begin{bmatrix} i_{1\alpha} & i_{1\beta} \end{bmatrix}^T
$$

$$
\mathbf{i}_{2\alpha\beta} = \begin{bmatrix} i_{2\alpha} & i_{2\beta} \end{bmatrix}^T
$$

Expanding (2.50), the dynamic equations in the αβ reference frame are

$$
\frac{di_{1\alpha}}{dt} = \frac{V_{1\alpha}}{L_1} - \frac{u_{1\alpha}q_C}{2CL_1} \tag{2.51}
$$

$$\frac{di_{1\beta}}{dt} = \frac{V_{1\beta}}{L_1} - \frac{u_{1\beta}q_C}{2CL_1} \tag{2.52}$$

$$\frac{di_{2\alpha}}{dt} = -\frac{u_{2\alpha}q_C}{2CL_2} - \frac{R_2}{L_2}i_{2\alpha} \tag{2.53}$$

$$\frac{di_{2\beta}}{dt} = -\frac{u_{2\beta}q_C}{2CL_2} - \frac{R_2}{L_2}i_{2\beta} \tag{2.54}$$

$$\frac{dq_C}{dt} = \frac{i_{1\alpha}u_{1\alpha}}{2} + \frac{i_{1\beta}u_{1\beta}}{2} + \frac{i_{2\alpha}u_{2\alpha}}{2} + \frac{i_{2\beta}u_{2\beta}}{2} - \frac{q_C}{CR_C} \tag{2.55}$$

2.1.4.   Transformation of Dynamic Equations to the *dq* Reference Frame

The graphical interpretation of the transformation from the αβ reference frame to the *dq* reference frame is shown in Figure 2.2, and the angle ϕ of the *dq* reference frame is the angle between the rotating *d*-axis and the stationary α-axis. The transformation is given by [44]

$$\mathbf{x}_{dq0} = \mathbf{K}(\phi)\mathbf{x}_{\alpha\beta z}$$
$$\mathbf{K}(\phi) = \begin{bmatrix} \cos\phi & \sin\phi & 0 \\ -\sin\phi & \cos\phi & 0 \\ 0 & 0 & 1 \end{bmatrix} \tag{2.56}$$

Therefore, the transformation from the *abc* reference frame to the *dq* reference frame is given by

$$\mathbf{x}_{dq0} = \mathbf{K}(\phi)\mathbf{x}_{\alpha\beta z} = \mathbf{K}(\phi)\mathbf{T}\mathbf{x}_{abc} = \mathbf{P}(\phi)\mathbf{x}_{abc}$$
$$\mathbf{P}(\phi) = \sqrt{\frac{2}{3}}\begin{bmatrix} \cos\phi & \cos\left(\phi - \frac{2\pi}{3}\right) & \cos\left(\phi + \frac{2\pi}{3}\right) \\ -\sin\phi & -\sin\left(\phi - \frac{2\pi}{3}\right) & -\sin\left(\phi + \frac{2\pi}{3}\right) \\ \frac{1}{\sqrt{2}} & \frac{1}{\sqrt{2}} & \frac{1}{\sqrt{2}} \end{bmatrix} \tag{2.57}$$

Since the transformation $\mathbf{P}$ is defined in such a way that its transpose and inverse are equal, the transformation $\mathbf{P}$ defined here is power invariant, as in [44,46]. Sometimes in power system literature, the *dq* transformation is defined in such a way that it is not power invariant [43,45,47].

Again, when the *c* phase is dependent and is replaced as the negative sum of the *a* and *b* phases (as is the case for i_{1c} and i_{2c} in the ac/dc/ac converter), transformation (2.57) reduces to

$$\mathbf{x}_{dq} = \mathbf{P}_{red}(\phi)\mathbf{x}_{ab}$$

$$\mathbf{P}_{red}(\phi) = \sqrt{\frac{2}{3}}\begin{bmatrix} \cos(\phi)-\cos(\phi+2\pi/3) & \cos(\phi-2\pi/3)-\cos(\phi+2\pi/3) \\ -\sin(\phi)+\sin(\phi+2\pi/3) & -\sin(\phi-2\pi/3)+\sin(\phi+2\pi/3) \end{bmatrix} \quad (2.58)$$

For the ac/dc/ac converter, when transforming the quantities on the left side of the converter, a dq reference frame rotating at a speed equal to the frequency of the three-phase voltage source ω_1 is used ($\phi = \omega_1 t$). For transforming the quantities on the right side of the converter, a dq reference frame rotating at a speed equal to the desired frequency of the load currents ω_2 is used ($\phi = \omega_2 t$).

To obtain the differential equations in the dq reference frame, first the expressions for the derivatives of $\mathbf{i}_{1dq}$ and $\mathbf{i}_{2dq}$ are found in terms of the abc quantities.

$$\begin{bmatrix} \dot{\mathbf{i}}_{1dq} \\ \dot{\mathbf{i}}_{2dq} \\ \dot{q}_C \end{bmatrix} = \begin{bmatrix} \mathbf{P}_{red}(\omega_1 t)\mathbf{f}_1(\mathbf{V}_{1abc},\mathbf{u}_{1abc}) + \dfrac{d\mathbf{P}_{red}(\omega_1 t)}{dt}\mathbf{i}_{1ab} \\ \mathbf{P}_{red}(\omega_2 t)\mathbf{f}_2(\mathbf{u}_{2abc},\mathbf{i}_{2ab}) + \dfrac{d\mathbf{P}_{red}(\omega_2 t)}{dt}\mathbf{i}_{2ab} \\ f_3(\mathbf{u}_{1abc},\mathbf{u}_{2abc},\mathbf{i}_{1ab},\mathbf{i}_{2ab}) \end{bmatrix}$$

$$\mathbf{i}_{1dq} = \begin{bmatrix} i_{1d} & i_{1q} \end{bmatrix}^T$$

$$\mathbf{i}_{2dq} = \begin{bmatrix} i_{2d} & i_{2q} \end{bmatrix}^T \quad (2.59)$$

Note that since $\mathbf{P}_{red}$ is time-varying, the product rule must be applied when differentiating. Next, to find the expressions for the derivatives of $\mathbf{i}_{1dq}$ and $\mathbf{i}_{2dq}$ in terms of the dq quantities, the MATLAB 'subs' command is used to substitute the abc quantities in terms of the dq quantities.

$$\begin{bmatrix} \dot{\mathbf{i}}_{1dq} \\ \dot{\mathbf{i}}_{2dq} \\ \dot{q}_C \end{bmatrix} = \begin{bmatrix} \mathbf{P}_{red}(\omega_1 t)\mathbf{f}_1(\mathbf{P}^{-1}(\omega_1 t)\mathbf{V}_{1\alpha\beta z},\mathbf{P}^{-1}(\omega_1 t)\mathbf{u}_{1\alpha\beta z}) + \dfrac{d\mathbf{P}_{red}(\omega_1 t)}{dt}\mathbf{P}_{red}^{-1}(\omega_1 t)\mathbf{i}_{1dq} \\ \mathbf{P}_{red}(\omega_2 t)\mathbf{f}_2(\mathbf{P}^{-1}(\omega_2 t)\mathbf{u}_{2\alpha\beta z},\mathbf{P}_{red}^{-1}(\omega_2 t)\mathbf{i}_{2\alpha\beta}) + \dfrac{d\mathbf{P}_{red}(\omega_2 t)}{dt}\mathbf{P}_{red}^{-1}(\omega_2 t)\mathbf{i}_{2dq} \\ f_3(\mathbf{P}^{-1}(\omega_1 t)\mathbf{u}_{1\alpha\beta z},\mathbf{P}^{-1}(\omega_2 t)\mathbf{u}_{2\alpha\beta z},\mathbf{P}_{red}^{-1}(\omega_1 t)\mathbf{i}_{1\alpha\beta},\mathbf{P}_{red}^{-1}(\omega_2 t)\mathbf{i}_{2\alpha\beta}) \end{bmatrix}$$

$$\quad (2.60)$$

$$\mathbf{V}_{1dq0} = \begin{bmatrix} V_{1d} & V_{1q} & V_{10} \end{bmatrix}^T$$

$$\mathbf{u}_{1dq0} = \begin{bmatrix} u_{1d} & u_{1q} & u_{10} \end{bmatrix}^T, \quad \mathbf{u}_{2dqo} = \begin{bmatrix} u_{2d} & u_{2q} & u_{20} \end{bmatrix}^T$$

$$\mathbf{i}_{1dq} = \begin{bmatrix} i_{1d} & i_{1q} \end{bmatrix}^T, \quad \mathbf{i}_{2dq} = \begin{bmatrix} i_{2d} & i_{2q} \end{bmatrix}^T$$

Expanding (2.60), the dynamic equations in the *dq* reference frame are

$$\frac{di_{1d}}{dt} = i_{1q}\omega_1 + \frac{V_{1d}}{L_1} - \frac{q_C u_{1d}}{2CL_1} \tag{2.61}$$

$$\frac{di_{1q}}{dt} = -i_{1d}\omega_1 + \frac{V_{1q}}{L_1} - \frac{q_C u_{1q}}{2CL_1} \tag{2.62}$$

$$\frac{di_{2d}}{dt} = i_{2q}\omega_2 - \frac{R_2}{L_2}i_{2d} - \frac{q_C u_{2d}}{2CL_2} \tag{2.63}$$

$$\frac{di_{2q}}{dt} = -i_{2d}\omega_2 - \frac{R_2}{L_2}i_{2q} - \frac{q_C u_{2q}}{2CL_2} \tag{2.64}$$

$$\frac{dq_C}{dt} = \frac{i_{1d}u_{1d}}{2} + \frac{i_{1q}u_{1q}}{2} + \frac{i_{2d}u_{2d}}{2} + \frac{i_{2q}u_{2q}}{2} - \frac{q_C}{CR_C} \tag{2.65}$$

Passivity-based control will be designed for the ac/dc/ac converter in Chapter 4 using these dynamic equations.

2.2. Lagrangian Formulation Applied to Electromechanical Systems

The dynamics of mechanical systems can be easily modeled using Newton's second law of motion while the dynamics of electrical systems can be easily modeled using KCL and KVL equations, but the difficulty for electromechanical systems is determining the coupling between the subsystems. For example, for an electric machine, an electric torque is applied to the rotor as a result of the coupling between the mechanical and electrical subsystems. Conventionally, the coupling between the electrical and mechanical subsystems is determined using conservation of energy [38]. An alternative, perhaps easier, approach is to use the Lagrangian formulation, which provides a unified framework for analyzing the electrical and mechanical subsystem and explicitly captures the coupling between the subsystems [48].

Very little previous research has been done on applying the Lagrangian formulation to electric power systems, especially for multiple interconnected power systems components. In [49], the dynamics of one electric machine connected to an infinite bus are derived using the Lagrangian formulation, but this

derivation neglects the dynamics of the electric subsystem. In [48], the dynamic equations of an electric machine connected to an infinite bus are derived using the Lagrangian approach.

Extending this previous work, an automated computer-aided method was implemented for symbolically deriving the state space model for interconnected power systems using the Lagrangian approach [12]. The automation of this process is critical because even for relatively small power systems, it is very tedious to derive the dynamic equations by hand. The automated approach is then demonstrated for deriving the state space model for a variable speed drive for flywheels. The variable speed drive uses an ac/dc/ac converter to regulate the speed of the flywheel to a different frequency than the power grid frequency. Control for this variable speed drive will be designed in Chapter 5 using passivity-based control logic.

2.2.1.   Automated State Space Model Derivation Methodology

The automated approach can be used to solve for the dynamic equations of power systems with conventional power system components, such as synchronous machines, induction machines, transmission lines, and loads. The approach can also be applied to electrostatic machines, which Lawrence Livermore National Lab (LLNL) is using for integrating flywheels [50]. In conventional magnetic machines the electric torque results from the mutual inductance varying as a function of the rotor position, while in electrostatic machines, the electric torque results from the capacitance varying as a function of the rotor position. The Lagrangian formulation explicitly captures this coupling between subsystems for both cases. As with electric circuits, logic is implemented in the automated method to check for all-inductor cutsets and all-capacitor loops, so that the power system dynamics can be expressed as an ODE system rather than a DAE system.

The user should take the following steps to input the power system topology:

1. Draw schematics of the electrical subsystem and the mechanical subsystem. For each of the B branches in the electrical subsystem, label and define the directions of the current. For each of the

M machines in the mechanical subsystem, label and define the direction of the angular velocity of the rotor.

2. For each circuit in the electrical subsystem, choose one arbitrary junction to be ground and label the voltages at the other *J* junctions as λ_1, λ_2,..., λ_J. Write KCL equations at the non-ground junctions starting with the junction labeled λ_1 and ending with the junction labeled λ_J. Use the convention in (2.1) when writing the KCL equations. Again, for systems with power electronic switches, the KCL equations are a function of the switch positions.

3. Define all parameters, controllable inputs, the charge and current on each branch, and the angular velocity and angular position of the rotor of each machine as MATLAB 'syms'.

4. Form *B*x1 symbolic vectors for the current **I** and the charge **Q** consisting of the symbolic currents and charges on the individual branches.

5. Form 1x*B* symbolic vectors for the capacitance vector **C**, the resistance vector **R**, and the voltage source vector **V**, consisting respectively of the capacitances, resistances, and voltage sources on each branch. For the voltage source vector, if the direction of the current is such that it leaves the positive terminal of the voltage source, then the sign is positive. Otherwise, the sign is negative.

6. Form a *B*x*B* symbolic matrix for the inductance matrix **L** where the self-inductances of each branch are given on the diagonal entries of the matrix and the mutual inductance between branches are given on the off-diagonal entries of the matrix.

7. Form the constraint matrix **G**, which is a *J*x*B* matrix. $\mathbf{GI} = 0$ gives the KCL equations.

8. Form the Lagrange multiplier vector **Λ**, which is a 1x*J* symbolic matrix, consisting of the voltages at the *J* non-ground junctions.

9. For the mechanical subsystem, form *M*x1 symbolic vectors for the angular velocity **Ω** and the angular position **Θ** consisting of the symbolic angular velocities and angular positions of each individual machine.

10. Form 1x*M* symbolic vectors for the inertia matrix **J**, the damping matrix **B**, and the mechanical torque matrix $\boldsymbol{\tau}_M$ consisting respectively of the inertias, damping factors, and external mechanical torques on each machine. For the mechanical torque vector, if the direction of the mechanical torque is such that it opposes the angular velocity of the machine, then the sign is negative. Otherwise, the sign is positive.

Given the power system input defined by the matrices **I, Q, C, R, V, L, G, Λ, Ω, Θ, J, B**, and $\boldsymbol{\tau}_M$, the computer solves for the dynamic equations using the Lagrangian approach by taking the following steps:

1. First the electrical subsystem is considered. Find the total magnetic co-energy $W_m{'}$ stored in the inductors of the electrical subsystem, which is given by (2.2).

2. Find the total electric energy W_e stored in the capacitors, which is given by (2.3)

3. Find the Lagrangian for the electrical subsystem $\mathcal{L}_{elec}$, which is given by (2.4)

4. Find the Rayleigh dissipation function for the electrical subsystem $\mathcal{R}_{elec}$, which is given by (2.5)

5. Now consider the mechanical subsystem. Find the kinetic co-energy *KE'* stored in the rotating masses of the machines, which is

$$KE' = \sum_{k=1}^{M} \frac{1}{2} \mathbf{J}(k) \boldsymbol{\Omega}(k)^2 \tag{2.66}$$

6. Since there are no springs in electric machines, the potential energy is zero. Find the Lagrangian for the mechanical subsystem $\mathcal{L}_{mech}$, which is

$$\mathcal{L}_{mech} = KE' - PE = KE' \tag{2.67}$$

7. Find the Rayleigh dissipation function for the mechanical subsystem $\mathcal{R}_{mech}$, which is

$$\mathcal{R}_{mech} = \sum_{k=1}^{M} \frac{1}{2} \mathbf{B}(k) \boldsymbol{\Omega}(k)^2 \tag{2.68}$$

8. Combine the Lagrangians and the Rayleigh dissipation functions from the electrical and mechanical subsystems.

$$\mathcal{L} = \mathcal{L}_{elec} + \mathcal{L}_{mech} \tag{2.69}$$

27

$$\mathscr{R} = \mathscr{R}_{elec} + \mathscr{R}_{mech} \tag{2.70}$$

9. Form $(B+M)$x1 vectors for the generalized flow $\mathbf{F}_{gen}$ consisting of the electric currents and the mechanical angular velocities and for the generalized charge $\mathbf{Q}_{gen}$ consisting of the electric charges and the mechanical angular positions.

$$\mathbf{F}_{gen} = \begin{bmatrix} \mathbf{I} \\ \boldsymbol{\Omega} \end{bmatrix} \tag{2.71}$$

$$\mathbf{Q}_{gen} = \begin{bmatrix} \mathbf{Q} \\ \boldsymbol{\Theta} \end{bmatrix} \tag{2.72}$$

10. Form a $(B+M)$x1 vector for the generalized forcing function $\mathscr{F}$.

$$\mathscr{F} = \begin{bmatrix} \mathbf{V} \\ \boldsymbol{\tau}_M \end{bmatrix} \tag{2.73}$$

11. Form the Lagrange equations of the first kind, which for an electromechanical system are [48]

$$\frac{d}{dt}\left[\frac{\partial \mathscr{L}}{\partial \mathbf{F}_{gen}(k)} \right] - \frac{\partial \mathscr{L}}{\partial \mathbf{Q}_{gen}(k)} + \frac{\partial \mathscr{R}}{\partial \mathbf{F}_{gen}(k)} - \mathscr{F}(k) - \frac{\partial \boldsymbol{\Lambda}\mathbf{GI}}{\partial \mathbf{F}_{gen}(k)} = 0 \tag{2.74}$$
$$\text{for } k = 1, 2, ... B + M$$

The Lagrange equations for electromechanical systems specify that the voltage across each branch must be equal to the difference between the two junction voltages adjacent to that branch and specify that the inertia multiplied by the angular acceleration of each machine must equal to the sum of the torques on the rotor of the machine (including the electric torque resulting from the coupling between the electrical and mechanical subsystems).

12. Add the KCL equations, $\mathbf{GI} = 0$, to these equations in order to form the initial set of equations.

13. For each machine, add another equation to the system: $d\theta_k / dt = \omega_k$.

14. For branches containing both a capacitor and an inductor, add another equation to the system: $dq_k / dt = i_k$.

15. For branches containing a capacitor but not an inductor, substitute in dq_k / dt for i_k.

28

16. Check for any all-inductor cutsets. If there is an all-inductor cutset, a current must be substituted by an expression in terms of the other currents in the all-inductor cutset. Also, the derivative of that current must be substituted by the derivative of that expression. Finally, the proper KCL equation must be eliminated from the system of equations.

17. Check for any all-capacitor loops. If there is an all-capacitor loop, a charge must be substituted by an expression in terms of the other charges and voltages sources in the loop. Also, the derivative of that charge must be substituted by the derivative of that expression as well. Finally, the Lagrange equation for the branch whose charge was substituted for must be eliminated from the system of equations.

18. At this point, there are $B + 2M + J + B_{both} - D$ equations and $B_{none} + 2B_{ind} + 2B_{cap} + 4B_{both} + J - 2D + 4M$ unknowns where D is the number of dependent storage devices, B_{none} is the number of branches with neither an inductor nor a capacitor, B_{ind} is the number of branches with an inductor but not a capacitor, B_{cap} is the number of branches with a capacitor but not an inductor, and B_{both} is the number of branches with both a capacitor and an inductor. There are $B_{ind} + B_{cap} + 2B_{both} - D + 2M$ (the sum of the number of independent storage devices and twice the number of machines) more unknowns than equations.

To form the state space model, the derivatives of the state variables need to be solved for in terms of only the state variables (not the λ's or the currents in branches with no storage devices). Therefore, the MATLAB 'solve' function is used to symbolically solve for the $B_{ind} + B_{cap} + 2B_{both} - D + 2M$ derivatives of the state variables, as well as the J λ's and the B_{none} currents, in terms of the $B_{ind} + B_{cap} + 2B_{both} - D + 2M$ state variables.

The solution returned by the MATLAB 'solve' function is in the general state space form

$$\dot{\mathbf{x}} = \mathbf{f}(x, u) \tag{2.75}$$

The electrical state variables are the independent inductor currents and the independent capacitor charges. The mechanical state variables are the angular velocity and the angular position of the rotor of each machine.
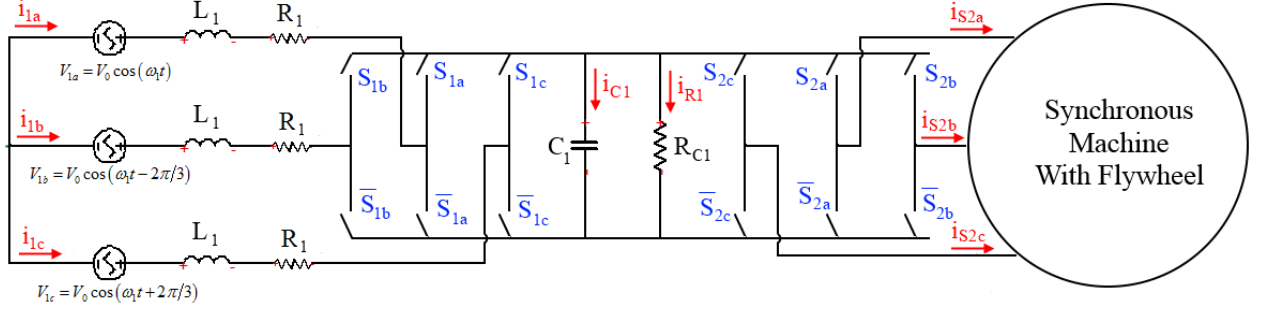
Figure 2.3: Topology for flywheel variable speed drive.

2.2.2. Example: Variable Speed Drive for Flywheels

As an example of the automated modeling methodology, consider the variable speed drive shown in Figure 2.3, where an ac/dc/ac converter drives a synchronous machine with a flywheel energy storage system. There is a three-phase voltage source at a constant frequency ω_1 on the left side of the converter, a dc-link capacitor in the middle, and the synchronous machine attached to the flywheel on the right side of the converter. The objective of the variable speed drive is to regulate the speed of the flywheel (and hence the energy stored in the flywheel) to a different frequency than the grid frequency. As in Section 2.1.2, the controllable inputs are again the positions of the twelve switches. The switching functions $u_{1a}, u_{1b}, u_{1c}, u_{2a}, u_{2b},$ and u_{2c} are defined using (2.8).

The schematic of the mechanical subsystem is shown in Figure 2.4. The synchronous machine is assumed to have three phases on the stator and one phase on the rotor, and the angular position of the rotor θ_2 is defined as angle between the rotor winding and the a-phase of the stator winding, as shown in Figure 2.4. The direction of the angular velocity is chosen to be in the counterclockwise direction.

As shown by Figure 2.5, the electrical subsystem consists of two coupled circuits: the synchronous machine rotor windings and the synchronous machine stator windings which are connected to the ac/dc/ac converter. The mutual inductances between the stator windings and the rotor winding of the synchronous machine depend on the angular position θ_2 of the rotor. The mutual inductance between the a-phase

30

stator winding and the rotor winding is given by $M_2 \cos \theta_2$, the mutual inductance between the b-phase

stator winding and the rotor winding is given by $M_2 \cos(\theta_2 - 2\pi/3)$, and the mutual inductance between

the c-phase stator winding and the rotor winding is given by $M_2 \cos(\theta_2 + 2\pi/3)$. There is also a

negative mutual inductance, $-L_{SS2}$, between the three phases of the stator windings.
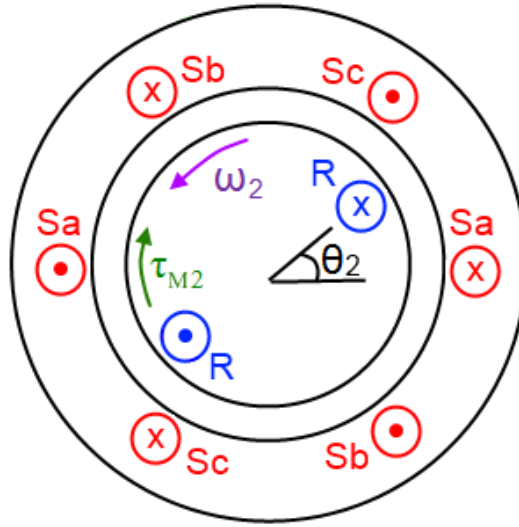
Rotor Inertia: J_2
Damping Coefficient: B_2

Figure 2.4: Mechanical subsystem of the variable speed drive shown in Figure 2.3.

The directions of the currents are labeled on each of the nine branches in the electrical subsystem

while the three non-ground junctions are labeled λ_1-λ_3 as shown in Figure 2.4. Using the convention in

(2.1), the KCL equations at these three non-ground junctions are

$$\frac{-(1+u_{1a})}{2}i_{1a} - \frac{(1+u_{1b})}{2}i_{1b} - \frac{(1+u_{1c})}{2}i_{1c} + i_C + i_{RC} - \frac{(1+u_{2a})}{2}i_{S2a} - \frac{(1+u_{2b})}{2}i_{S2b} - \frac{(1+u_{2c})}{2}i_{S2c} = 0 \quad (2.76)$$

$$\frac{-(1-u_{1a})}{2}i_{1a} - \frac{(1-u_{1b})}{2}i_{1b} - \frac{(1-u_{1c})}{2}i_{1c} - i_C - i_{RC} - \frac{(1-u_{2a})}{2}i_{S2a} - \frac{(1-u_{2b})}{2}i_{S2b} - \frac{(1-u_{2c})}{2}i_{S2c} = 0 \quad (2.77)$$

$$i_{S2a} + i_{S2b} + i_{S2c} = 0 \quad (2.78)$$

31
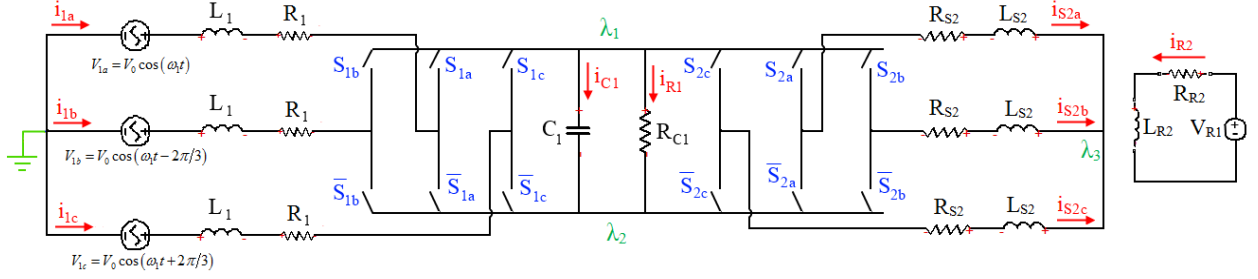
Figure 2.5: Electrical subsystem of the variable speed drive shown in Figure 2.3.

All parameters, the charges and currents on the nine branches, and the angular positions and angular velocities of the machine are defined as MATLAB "syms." The symbolic vectors **I** and **Q** are defined as

$$\mathbf{I} = \begin{bmatrix} i_{1a} & i_{1b} & i_{1c} & i_{C1} & i_{R1} & i_{S2a} & i_{S2b} & i_{S2c} & i_{R2} \end{bmatrix}^T \tag{2.79}$$

$$\mathbf{Q} = \begin{bmatrix} q_{1a} & q_{1b} & q_{1c} & q_{C1} & q_{R1} & q_{S2a} & q_{S2b} & q_{S2c} & q_{R2} \end{bmatrix}^T \tag{2.80}$$

The inductance matrix **L** is defined as

$$\mathbf{L} = \begin{bmatrix}
L_1 & 0 & 0 & 0 & 0 & 0 & 0 & 0 & 0 \\
0 & L_1 & 0 & 0 & 0 & 0 & 0 & 0 & 0 \\
0 & 0 & L_1 & 0 & 0 & 0 & 0 & 0 & 0 \\
0 & 0 & 0 & 0 & 0 & 0 & 0 & 0 & 0 \\
0 & 0 & 0 & 0 & 0 & 0 & 0 & 0 & 0 \\
0 & 0 & 0 & 0 & 0 & L_{S2} & -L_{SS2} & -L_{SS2} & M_2\cos\theta_2 \\
0 & 0 & 0 & 0 & 0 & -L_{SS2} & L_{S2} & -L_{SS2} & M_2\cos\left(\theta_2 - \dfrac{2\pi}{3}\right) \\
0 & 0 & 0 & 0 & 0 & -L_{SS2} & -L_{SS2} & L_{S2} & M_2\cos\left(\theta_2 + \dfrac{2\pi}{3}\right) \\
0 & 0 & 0 & 0 & 0 & M_2\cos\theta_2 & M_2\cos\left(\theta_2 - \dfrac{2\pi}{3}\right) & M_2\cos\left(\theta_2 + \dfrac{2\pi}{3}\right) & L_{R2}
\end{bmatrix} \tag{2.81}$$

The capacitance vector **C**, the resistance vector **R**, and the voltage source vector **V** are

$$\mathbf{C} = \begin{bmatrix} 0 & 0 & 0 & C_1 & 0 & 0 & 0 & 0 & 0 \end{bmatrix} \tag{2.82}$$

$$\mathbf{R} = \begin{bmatrix} R_1 & R_1 & R_1 & 0 & R_{C1} & R_{S2} & R_{S2} & R_{S2} & R_{R2} \end{bmatrix} \tag{2.83}$$

$$\mathbf{V} = \begin{bmatrix} V_{1a} & V_{1b} & V_{1c} & 0 & 0 & 0 & 0 & 0 & V_{R2} \end{bmatrix} \tag{2.84}$$

The constraint matrix **G**, which when multiplied by **I**, yields the KCL equations (2.76)-(2.78), is

$$\mathbf{G} = \begin{bmatrix} -(1+u_{1a})/2 & -(1+u_{1b})/2 & -(1+u_{1c})/2 & 1 & 1 & -(1+u_{2a})/2 & -(1+u_{2b})/2 & -(1+u_{2c})/2 & 0 \\ -(1-u_{1a})/2 & -(1-u_{1b})/2 & -(1-u_{1c})/2 & -1 & -1 & -(1-u_{2a})/2 & -(1-u_{2b})/2 & -(1-u_{2c})/2 & 0 \\ 0 & 0 & 0 & 0 & 0 & 1 & 1 & 1 & 0 \end{bmatrix} \quad (2.85)$$

The Lagrange multiplier vector $\mathbf{\Lambda}$, which contains the voltages at the three non-ground junctions, is

$$\mathbf{\Lambda} = \begin{bmatrix} \lambda_1 & \lambda_2 & \lambda_3 \end{bmatrix} \quad (2.86)$$

The symbolic vector $\mathbf{\Omega}$ and $\mathbf{\Theta}$ are defined as

$$\mathbf{\Omega} = \begin{bmatrix} \omega_2 \end{bmatrix} \quad (2.87)$$

$$\mathbf{\Theta} = \begin{bmatrix} \theta_2 \end{bmatrix} \quad (2.88)$$

The inertia vector $\mathbf{J}$, the damping vector $\mathbf{B}$, and the mechanical torque vector $\boldsymbol{\tau}_M$ are defined as

$$\mathbf{J} = \begin{bmatrix} J_2 \end{bmatrix} \quad (2.89)$$

$$\mathbf{B} = \begin{bmatrix} B_2 \end{bmatrix} \quad (2.90)$$

$$\boldsymbol{\tau}_M = \begin{bmatrix} -\tau_{M2} \end{bmatrix} \quad (2.91)$$

Given the power system input defined by the matrices $\mathbf{I}$, $\mathbf{Q}$, $\mathbf{C}$, $\mathbf{R}$, $\mathbf{U}$, $\mathbf{L}$, $\mathbf{G}$, $\mathbf{\Lambda}$, $\mathbf{\Omega}$, $\mathbf{\Theta}$, $\mathbf{J}$, $\mathbf{B}$, and $\boldsymbol{\tau}_M$,

the MATLAB code solves for the dynamic model of the circuit through the steps detailed below.

First the electric subsystem is considered. The magnetic co-energy stored in the inductors is

$$\begin{aligned} W_m' = {} & \frac{1}{2} L_1 \left(i_{1a}{}^2 + i_{1b}{}^2 + i_{1c}{}^2 \right) + \frac{1}{2} L_{R2} i_{R2}{}^2 + \frac{1}{2} L_{S2} \left(i_{S2a}{}^2 + i_{S2b}{}^2 + i_{S2c}{}^2 \right) \\ & - L_{SS2} \left(i_{S2a} i_{S2b} + i_{S2a} i_{S2c} + i_{S2b} i_{S2c} \right) + M_2 \cos(\theta_2) i_{R2} i_{S2a} \\ & + M_2 i_{R2} i_{S2b} \cos(\theta_2 - 2\pi/3) + M_2 i_{R2} i_{S2c} \cos(\theta_2 + 2\pi/3) \end{aligned} \quad (2.92)$$

The electric energy stored in the capacitor is

$$W_e = \frac{1}{2} \frac{q_{C1}{}^2}{C} \quad (2.93)$$

The Lagrangian for the electrical subsystem $\mathcal{L}_{elec}$ is calculated by subtracting W_e from W_m'.

The Rayleigh dissipation function for the electrical subsystem is

$$\mathcal{R}_{elec} = \frac{1}{2} R_1 \left(i_{1a}{}^2 + i_{1b}{}^2 + i_{1c}{}^2 \right) + \frac{1}{2} R_{C1} i_{R1}{}^2 + \frac{1}{2} R_{R2} i_{R2}{}^2 + \frac{1}{2} R_{S2} \left(i_{S2a}{}^2 + i_{S2b}{}^2 + i_{S2c}{}^2 \right) \quad (2.94)$$

Now the mechanical subsystem is considered. The kinetic co-energy is

$$KE' = \frac{1}{2} J_2 \omega_2^2 \tag{2.95}$$

The Lagrangian for the mechanical subsystem $\mathcal{L}_{\text{mech}}$ is equal to the kinetic co-energy since the potential energy of the system is zero.

The Rayleigh dissipation function for the mechanical subsystem is

$$\mathcal{R}_{\text{mech}} = \frac{1}{2} B_2 \omega_2^2 \tag{2.96}$$

The total Lagrangian $\mathcal{L}$ and the total dissipation function $\mathcal{R}$ are formed by adding $\mathcal{L}_{\text{elec}}$ and $\mathcal{L}_{\text{mech}}$ and by adding $\mathcal{R}_{\text{elec}}$ and $\mathcal{R}_{\text{mech}}$ respectively. The generalized flow matrix $\mathbf{F_{gen}}$ and the generalized charge matrix $\mathbf{Q_{gen}}$ are formed using (2.71) and (2.72). The generalized forcing function $\mathcal{F}$ is formed using (2.73).

The Lagrange equations from evaluating (2.74) are

$$\lambda_1 (1+u_{1a})/2 - V_{1a} + \lambda_2 (1-u_{1a})/2 + L_1 \frac{di_{1a}}{dt} + R_1 i_{1a} = 0 \tag{2.97}$$

$$\lambda_1 (1+u_{1b})/2 - V_{1b} + \lambda_2 (1-u_{1b})/2 + L_1 \frac{di_{1b}}{dt} R_1 i_{1b} = 0 \tag{2.98}$$

$$\lambda_1 (1+u_{1c})/2 - V_{1c} + \lambda_2 (1-u_{1c})/2 + L_1 \frac{di_{1c}}{dt} + R_1 i_{1c} = 0 \tag{2.99}$$

$$\lambda_2 - \lambda_1 + \frac{q_{C1}}{C_1} = 0 \tag{2.100}$$

$$\lambda_2 - \lambda_1 + R_{C1} i_{R1} = 0 \tag{2.101}$$

$$L_{S2} \frac{di_{S2a}}{dt} - L_{SS2} \frac{di_{S2b}}{dt} - L_{SS2} \frac{di_{S2c}}{dt} + R_{S2} i_{S2a} + M_2 \cos\theta_2 \frac{di_{R2}}{dt}$$
$$-M_2 \sin\theta_2 \frac{d\theta_2}{dt} i_{R2} + \lambda_1 (1+u_{2a})/2 - \lambda_3 + \lambda_2 (1-u_{2a})/2 = 0 \tag{2.102}$$

$$L_{S2} \frac{di_{S2b}}{dt} - L_{SS2} \frac{di_{S2a}}{dt} - L_{SS2} \frac{di_{S2c}}{dt} + R_{S2} i_{S2b} + M_2 \cos\left(\theta_2 - \frac{2\pi}{3}\right) \frac{di_{R2}}{dt}$$
$$-M_2 \sin\left(\theta_2 - \frac{2\pi}{3}\right) \frac{d\theta_2}{dt} i_{R2} + \lambda_1 (1+u_{2b})/2 - \lambda_3 + \lambda_2 (1-u_{2b})/2 = 0 \tag{2.103}$$

34

$$L_{S2}\frac{di_{S2c}}{dt} - L_{SS2}\frac{di_{S2a}}{dt} - L_{SS2}\frac{di_{S2b}}{dt} + R_{S2}i_{S2c} + M_2\cos\left(\theta_2 + \frac{2\pi}{3}\right)\frac{di_{R2}}{dt}$$

$$-M_2\sin\left(\theta_2 + \frac{2\pi}{3}\right)\frac{d\theta_2}{dt}i_{R2} + \lambda_1(1+u_{2c})/2 - \lambda_3 + \lambda_2(1-u_{2c})/2 = 0 \tag{2.104}$$

$$L_{R2}\frac{di_{R2}}{dt} - v_{R2} + R_{R2}i_{R2} + M_2\cos\theta_2\frac{di_{S2a}}{dt} - M_2\sin\theta_2\frac{d\theta_2}{dt}i_{S2a} + M_2\cos\left(\theta_2 - \frac{2\pi}{3}\right)\frac{di_{S2b}}{dt}$$

$$-M_2\sin\left(\theta_2 - \frac{2\pi}{3}\right)\frac{d\theta_2}{dt}i_{S2b} + M_2\cos\left(\theta_2 + \frac{2\pi}{3}\right)\frac{di_{S2c}}{dt} - M_2\sin\left(\theta_2 + \frac{2\pi}{3}\right)\frac{d\theta_2}{dt}i_{S2c} = 0 \tag{2.105}$$

$$J_2\frac{d\omega_2}{dt} + \tau_{M2} + B_2\omega_2 + M_2 i_{R2}i_{S2b}\sin\left(\theta_2 - \frac{2\pi}{3}\right) + M_2 i_{R2}i_{S2c}\sin\left(\theta_2 + \frac{2\pi}{3}\right) + M_2 i_{R2}i_{S2a}\sin\theta_2 = 0 \tag{2.106}$$

The last three terms of (2.106) represent the electric torque, which is explicitly captured when evaluating the Lagrange equations.

According to Step 13, the following equation for the synchronous machine must be added to the system of equations:

$$\frac{d\theta_2}{dt} - \omega_2 = 0 \tag{2.107}$$

There are no branches with both an inductor and a capacitor, but there is one branch with a capacitor but not an inductor. Therefore, i_C is replaced by dq_C/dt in (2.76)-(2.78) and (2.97)-(2.107). There are no all-capacitor loops, but there are two all-inductor cutsets. KCL equation (2.78) forms an all-inductor cutset, so i_{S2c} is replaced by $-i_{S2a} - i_{S2b}$ and (2.78) is removed from the system of equations. The sum of KCL equations (2.76) and (2.77) also forms an all-inductor so i_{1c} is replaced by $-i_{1a} - i_{1b}$. Since the all-inductor cutset occurred in the sum of (2.76) and (2.77), either equation could be removed from the system of equations. Equation (2.76) is chosen to be removed.

After making these changes, in the new system of equations, the number of equations, $B + 2M + J + B_{both} - D$, is 12 and the number of unknowns, $B_{none} + 2B_{ind} + 2B_{cap} + 4B_{both} + J - 2D + 4M$, is 20. (For this example $B = 9$, $M = 1$, $J = 3$, $B_{both} = 0$, $D = 2$, $B_{none} = 1$, $B_{ind} = 7$, and $B_{cap} = 1$.) The

unknowns are i_{1a}, i_{1b}, q_{C1}, i_{R1}, i_{S2a}, i_{S2b}, i_{R2}, ω_2, θ_2, di_{1a}/dt, di_{1b}/dt, dq_{C1}/dt, di_{S2a}/dt, di_{S2b}/dt, di_{R2}/dt, $d\omega_2/dt$, $d\theta_2/dt$, λ_1, λ_2, and λ_3.

The MATLAB 'solve' function is used to symbolically solve for the state variables derivatives (di_{1a}/dt, di_{1b}/dt, dq_{C1}/dt, di_{S2a}/dt, di_{S2b}/dt, di_{R2}/dt, $d\omega_2/dt$, $d\theta_2/dt$), as well as i_{R1}, λ_1, λ_2, and λ_3, in terms of the state variables (i_{1a}, i_{1b}, q_{C1}, i_{S2a}, i_{S2b}, i_{R2}, ω_2, θ_2). In the standard state space form given by (2.7), the dynamic equations of the variable speed drive are

$$\frac{di_{1a}}{dt} = \frac{q_C}{6CL_1}\left(-2u_{1a} + u_{1b} + u_{1c}\right) - \frac{1}{3L_1}\left(-2V_{1a} + V_{1b} + V_{1c}\right) - \frac{R_1}{L_1}i_{1a} \qquad (2.108)$$

$$\frac{di_{1b}}{dt} = \frac{q_C}{6CL_1}\left(u_{1a} - 2u_{1b} + u_{1c}\right) - \frac{1}{3L_1}\left(V_{1a} - 2V_{1b} + V_{1c}\right) - \frac{R_1}{L_1}i_{1b} \qquad (2.109)$$

$$\frac{dq_{C1}}{dt} = \frac{i_{1a}}{2}\left(u_{1a} - u_{1c}\right) + \frac{i_{1b}}{2}\left(u_{1b} - u_{1c}\right) + \frac{i_{S2a}}{2}\left(u_{2a} - u_{2c}\right) + \frac{i_{S2b}}{2}\left(u_{2b} - u_{2c}\right) - \frac{q_{C1}}{C_1 R_{C1}} \quad (2.110)$$

$$\frac{d\mathbf{I}_2}{dt} = inv(\mathbf{L}_2)\left(\mathbf{V}_2 - \mathbf{R}_2\mathbf{I}_2 - \frac{d\mathbf{L}_2}{d\theta_2}\mathbf{I}_2\omega_2\right) \qquad (2.111)$$

$$\frac{d\omega_2}{dt} = \frac{M_2 i_{R2}\left(\sqrt{3}/2\, i_{S2a}\cos\theta_2 + \sqrt{3}\, i_{S2b}\cos\theta_2 - 3/2\, i_{S2a}\sin\theta_2\right) - \tau_{M2} - B_2\omega_2}{J_2} \qquad (2.112)$$

$$\frac{d\theta_2}{dt} = \omega_2 \qquad (2.113)$$

where

$$\mathbf{I}_2 = \begin{bmatrix} i_{S2a} \\ i_{S2b} \\ i_{R2} \end{bmatrix}, \ \mathbf{V}_2 = \begin{bmatrix} v_{S2a} \\ v_{S2b} \\ v_{R2} \end{bmatrix}, \ \mathbf{R}_2 = \begin{bmatrix} R_{S2} & 0 & 0 \\ 0 & R_{S2} & 0 \\ 0 & 0 & R_{R2} \end{bmatrix} \qquad (2.114)$$

$$\mathbf{L}_2 = \begin{bmatrix} L_{S2} + L_{SS2} & 0 & M_2\left(\cos\theta_2 - \cos\left(\theta_2 + \frac{2\pi}{3}\right)\right) \\ 0 & L_{S2} + L_{SS2} & M_2\left(\cos\left(\theta_2 - \frac{2\pi}{3}\right) - \cos\left(\theta_2 + \frac{2\pi}{3}\right)\right) \\ M_2\left(\cos\theta_2 - \cos\left(\theta_2 + \frac{2\pi}{3}\right)\right) & M_2\left(\cos\left(\theta_2 - \frac{2\pi}{3}\right) - \cos\left(\theta_2 + \frac{2\pi}{3}\right)\right) & L_{R2} \end{bmatrix} \qquad (2.115)$$

36

The dynamic equations of the variable speed drive can be simplified by transforming to the *dq* reference frame as described in Section 2.1.4. For transforming the quantities on the left side of the converter, a *dq* reference frame rotating at a speed equal to the frequency of the three-phase voltage source ω_1 is used ($\phi = \omega_1 t$). For transforming the quantities on the right side of the converter, a *dq* reference frame fixed to the synchronous machine rotor is used ($\phi = \theta_2$). Choosing a reference frame fixed to the synchronous machine rotor eliminates the time-varying mutual inductances in (2.115). Using the *dq* reference frame, the dynamic equations can be written compactly as

$$\frac{di_{1d}}{dt} = i_{1q}\omega_1 + \frac{V_{1d}}{L_1} - \frac{R_1}{L_1}i_{1d} - \frac{q_{C1}u_{1d}}{2C_1 L_1} \tag{2.116}$$

$$\frac{di_{1q}}{dt} = -i_{1d}\omega_1 + \frac{V_{1q}}{L_1} - \frac{R_1}{L_1}i_{1q} - \frac{q_{C1}u_{1q}}{2C_1 L_1} \tag{2.117}$$

$$\frac{dq_{C1}}{dt} = \frac{i_{1d}u_{1d}}{2} + \frac{i_{1q}u_{1q}}{2} - \frac{i_{S2d}u_{2d}}{2} - \frac{i_{S2q}u_{2q}}{2} - \frac{q_{C1}}{C_1 R_{C1}} \tag{2.118}$$

$$\frac{d\mathbf{I}_2}{dt} = inv(\mathbf{L}_2)\left(\mathbf{V}_2 - \mathbf{R}_2\mathbf{I}_2 - \Omega_2\mathbf{L}_2\mathbf{I}_2\right) \tag{2.119}$$

$$\frac{d\omega_2}{dt} = \frac{\tau_{e2} - \tau_{M2} - B_2\omega_2}{J_2} \tag{2.120}$$

$$\frac{d\theta_2}{dt} = \omega_2 \tag{2.121}$$

where

$$\mathbf{I}_2 = \begin{bmatrix} i_{S2d} \\ i_{S2q} \\ i_{R2} \end{bmatrix}, \quad \mathbf{V}_2 = \begin{bmatrix} v_{S2d} \\ v_{S2q} \\ v_{R2} \end{bmatrix}, \quad \mathbf{R}_2 = \begin{bmatrix} R_{S2} & 0 & 0 \\ 0 & R_{S2} & 0 \\ 0 & 0 & R_{R2} \end{bmatrix},$$

$$\mathbf{L}_2 = \begin{bmatrix} L_{S2} + L_{SS2} & 0 & \sqrt{\frac{3}{2}}M_2 \\ 0 & L_{S2} + L_{SS2} & 0 \\ \sqrt{\frac{3}{2}}M_2 & 0 & L_{R2} \end{bmatrix}, \quad \Omega_2 = \begin{bmatrix} 0 & -\omega_2 & 0 \\ \omega_2 & 0 & 0 \\ 0 & 0 & 0 \end{bmatrix} \tag{2.122}$$

37

$$\tau_e = \sqrt{\frac{3}{2}} M_2 i_{R2} i_{Sq2} \tag{2.123}$$

$$v_{S2d} = \frac{q_{C1} u_{2d}}{2C_1} \quad , \quad v_{S2q} = \frac{q_{C1} u_{2q}}{2C_1} \tag{2.124}$$

Passivity-based control will be designed for the variable speed drive in Chapter 5 using these dynamic equations.

2.3. Summary

In this chapter, novel automated computer-aided methods were introduced for deriving the dynamic model in standard state space form of electric circuits and electric power systems. These automated methods use the Lagrangian formulation from classical mechanics, where the model is obtained from the physical energies of the system. This formulation sets the stage for the passivity-based control in Chapter 4, where the error dynamics and then the control law are derived from desired closed-loop energy functions.

3. Automated Modular Modeling of Power System Dynamics

For large power systems, the automated approach described in Section 2.2.1 for solving for the state space equations can be very computationally intensive since the governing equations for power systems are nonlinear. For this reason, a new automated modular approach for deriving the state space model was implemented as described in [15,51]. Using this modular approach, first dynamic models for each power system component are derived using the Lagrangian approach and expressed in a common form. Then given the connection between modules, the dynamic models of each module are combined in an automated procedure. This modular approach is particularly useful for power systems because large systems contain many of the same types of components, such as synchronous machines, transmission lines, and loads.

Previous work on symbolic modular modeling of power system dynamics was presented in [52]. It should be emphasized that, while [52] generates and simulates a DAE system, the automated method described in this chapter expresses the power system dynamics in standard state space form as an ODE system, so that control can be systematically designed with provable performance.

Depending on how modules are connected, the interconnection of modules can produce all-inductor cutsets, which occur when one of the inductor currents can be expressed as a linear combination of the other inductor currents or all-capacitor loops, which occur when one of the capacitor charges can be expressed as a linear combination of the other capacitor charges. In this case, in order to express the dynamics of the interconnected system in standard state space form as an ODE system rather than a DAE system, it is necessary to eliminate a state variable from one of the modules. After combining the modules, it is shown that each module's dynamics can be expressed in terms of only its own state variables and the state variables of the modules directly connected to that module.

3.1. Individual Module Dynamics

Assuming that all components are modeled using lumped parameter models and all components, including transmission lines, are modeled as having dynamics, the dynamics for each module can be expressed in the following common form:

$$\dot{\mathbf{x}}_k = \mathbf{f}_k(x_k, p_k, u_k, m_k) \tag{3.1}$$

where $\mathbf{x}_k$ is the vector of state variables in module k, $\mathbf{u}_k$ is the vector of controllable inputs to module k, $\mathbf{m}_k$ is the vector of exogenous inputs to module k determined by factors outside the model, and $\mathbf{p}_k$ is the vector of port inputs to module k that will be determined by its connection to the rest of the system. As graphically depicted by Figure 3.1, power system components can have either one port per phase (such as synchronous machines and loads) or two ports per phase (such as transmission lines) [5].
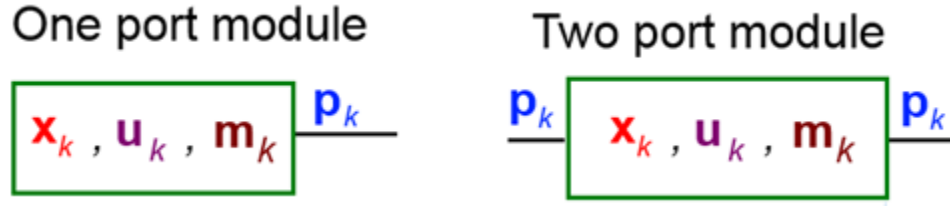
Figure 3.1: Visual representation of one and two port modules.

The dynamic equations for specific power system components used in this thesis are presented in this section. These dynamic equations are developed using the Lagrangian formulation described in the previous chapter and then are converted to a rotating dq reference frame at an arbitrary angle ϕ and a corresponding velocity $\Omega = d\phi/dt$. Since the dynamics of each module must be combined, the dynamics of each module are expressed relative to the same common reference frame with angle ϕ.

3.1.1.   Synchronous Machine

Conventional power plants, such as coal power plants, are typically modeled as synchronous machine [5]. In this thesis, the synchronous machine is modeled as a smooth-air-gap machine with three phases on the stator and one phase on the rotor [53], as shown in Figure 2.4. The dynamic equations for a synchronous machine are given by

$$\frac{d\mathbf{I}}{dt} = inv(\mathbf{L})(\mathbf{V} - \mathbf{RI} - \mathbf{\Omega LI}) \tag{3.2}$$

$$\frac{d\omega}{dt} = \frac{\tau_e - \tau_M - B\omega}{J} \tag{3.3}$$

$$\frac{d\theta}{dt} = \omega \tag{3.4}$$

where

$$\mathbf{I} = \begin{bmatrix} i_{Sd} \\ i_{Sq} \\ i_R \end{bmatrix}, \ \mathbf{V} = \begin{bmatrix} v_{Sd} \\ v_{Sq} \\ v_R \end{bmatrix}, \ \mathbf{R} = \begin{bmatrix} R_S & 0 & 0 \\ 0 & R_S & 0 \\ 0 & 0 & R_R \end{bmatrix}, \ \mathbf{L} = \begin{bmatrix} L_S + L_{SS} & 0 & \sqrt{\frac{3}{2}}M\cos(\phi-\theta) \\ 0 & L_S + L_{SS} & -\sqrt{\frac{3}{2}}M\sin(\phi-\theta) \\ \sqrt{\frac{3}{2}}M\cos(\phi-\theta) & -\sqrt{\frac{3}{2}}M\sin(\phi-\theta) & L_R \end{bmatrix} \tag{3.5}$$

$$\mathbf{\Omega} = \begin{bmatrix} 0 & -\Omega & 0 \\ \Omega & 0 & 0 \\ 0 & 0 & 0 \end{bmatrix} \tag{3.6}$$

$$\tau_e = \sqrt{\frac{3}{2}}M\left(i_R i_{Sq}\cos(\phi-\theta) + i_R i_{Sd}\sin(\phi-\theta)\right) \tag{3.7}$$

As seen by (3.5), the time-varying mutual inductances for the synchronous machine are only eliminated when using a *dq* reference frame fixed to the rotor ($\phi = \theta$) [47]. The port inputs to the synchronous machine module that will be determined by its connection to the rest of the system are the voltages applied to the stator windings. In the form given by (3.1),

$$\mathbf{x}_k = \begin{bmatrix} i_{Sd} & i_{Sq} & i_R & \omega & \theta \end{bmatrix}^T, \ \mathbf{u}_k = \begin{bmatrix} v_R & \tau_M \end{bmatrix}, \ \mathbf{m}_k = \begin{bmatrix} \ \end{bmatrix}, \ \mathbf{p}_k = \begin{bmatrix} v_{Sd} & v_{Sq} \end{bmatrix}^T \tag{3.8}$$

3.1.2. Induction Machine

Wind generators are typically modeled as induction machines [54]. In this thesis, the induction machine is modeled as a smooth-air-gap machine having three phases on the stator and three phases on the rotor [38], as shown in Figure 3.2. The dynamic equations for an induction machine are given by

$$\frac{d\mathbf{I}}{dt} = inv(\mathbf{L})\left(\mathbf{V} - \mathbf{RI} - \mathbf{\Omega LI}\right) \tag{3.9}$$

$$\frac{d\omega}{dt} = \frac{\tau_M - \tau_L - B\omega}{J} \tag{3.10}$$

41

$$\frac{d\theta}{dt} = \omega \tag{3.11}$$

where

$$\mathbf{I} = \begin{bmatrix} i_{Sd} \\ i_{Sq} \\ i_{Rd} \\ i_{Rq} \end{bmatrix}, \quad \mathbf{V} = \begin{bmatrix} v_{Sd} \\ v_{Sq} \\ 0 \\ 0 \end{bmatrix}, \quad \mathbf{R} = \begin{bmatrix} R_S & 0 & 0 & 0 \\ 0 & R_S & 0 & 0 \\ 0 & 0 & R_R & 0 \\ 0 & 0 & 0 & R_R \end{bmatrix} \tag{3.12}$$

$$\mathbf{L} = \begin{bmatrix} L_S + L_{SS} & 0 & \frac{3}{2}M & 0 \\ 0 & L_S + L_{SS} & 0 & \frac{3}{2}M \\ \frac{3}{2}M & 0 & L_R + L_{RR} & 0 \\ 0 & \frac{3}{2}M & 0 & L_R + L_{RR} \end{bmatrix}, \quad \mathbf{\Omega} = \begin{bmatrix} 0 & -\Omega & 0 & 0 \\ \Omega & 0 & 0 & 0 \\ 0 & 0 & 0 & \omega-\Omega \\ 0 & 0 & \Omega-\omega & 0 \end{bmatrix} \tag{3.13}$$

$$\tau_e = \frac{3}{2}M\left(i_{Rd}i_{Sq} - i_{Rq}i_{Sd}\right) \tag{3.14}$$
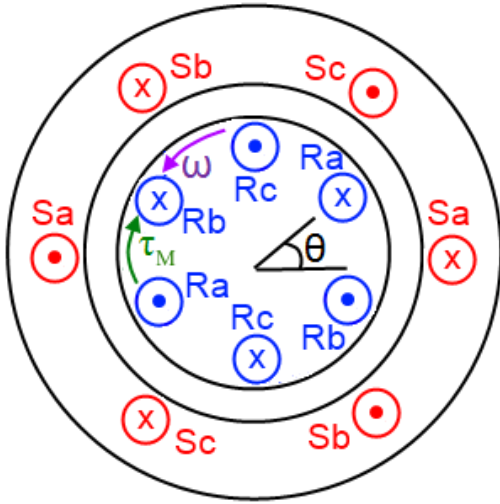
Figure 3.2: Visual representation of the induction machine with three phases on the rotor and three phases on the stator.
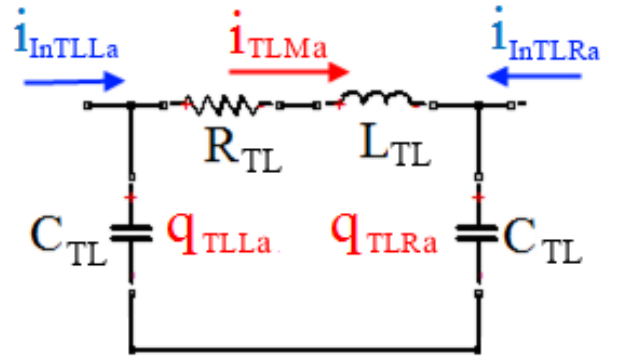
Figure 3.3: The *a*-phase of the transmission line using the pi model. The *b*-phase and *c*-phase are equivalent.

As seen by (3.13), the time-varying mutual inductances for the induction machine are eliminated for any arbitrary *dq* reference frame [47]. The exogenous input that is determined by factors outside the model is the mechanical torque applied to the induction machine. The port inputs to the induction

machine module that will be determined by its connection to the rest of the system are the voltages applied to the stator windings. In the form given by (3.1),

$$\mathbf{x}_k = \begin{bmatrix} i_{Sd} & i_{Sq} & i_{Rd} & i_{Rq} & \omega & \theta \end{bmatrix}^T, \ \mathbf{u}_k = \begin{bmatrix} \ \end{bmatrix}, \ \mathbf{m}_k = \begin{bmatrix} \tau_M \end{bmatrix}, \ \mathbf{p}_k = \begin{bmatrix} v_{Sd} & v_{Sq} \end{bmatrix}^T \tag{3.15}$$

3.1.3. Transmission Line

The transmission line is modeled using the pi model [55] with shunt capacitors, as shown in Figure 3.3. The dynamic equations for a transmission line are given by

$$\frac{dq_{TLLd}}{dt} = i_{InTLLd} - i_{TLMd} + \Omega q_{TLLq} \tag{3.16}$$

$$\frac{dq_{TLLq}}{dt} = i_{InTLLq} - i_{TLMq} - \Omega q_{TLLd} \tag{3.17}$$

$$\frac{di_{TLMd}}{dt} = \Omega i_{TLMq} - \frac{q_{TLRd} - q_{TLLd} + C_{TL}R_{TL}i_{TLMd}}{C_{TL}L_{TL}} \tag{3.18}$$

$$\frac{di_{TLMq}}{dt} = -\Omega i_{TLMd} - \frac{q_{TLRq} - q_{TLLq} + C_{TL}R_{TL}i_{TLMq}}{C_{TL}L_{TL}} \tag{3.19}$$

$$\frac{dq_{TLRd}}{dt} = \Omega q_{TLRq} + i_{InTLRd} + i_{TLMd} \tag{3.20}$$

$$\frac{dq_{TLRq}}{dt} = -\Omega q_{TLRd} + i_{InTLRq} + i_{TLMq} \tag{3.21}$$

The port inputs to the transmission line module that will be determined by its connection to the rest of the system are the currents applied to each side of the transmission line. In the form given by (3.1),

$$\mathbf{x}_k = \begin{bmatrix} q_{TLLd} & q_{TLLq} & i_{TLMd} & i_{TLMq} & q_{TLRd} & q_{TLRq} \end{bmatrix}^T, \ \mathbf{u}_k = \begin{bmatrix} \ \end{bmatrix},$$
$$\mathbf{m}_k = \begin{bmatrix} \ \end{bmatrix}, \ \mathbf{p}_k = \begin{bmatrix} i_{InTLLd} & i_{InTLLq} & i_{InTLRd} & i_{InTLRq} \end{bmatrix}^T \tag{3.22}$$

3.1.4. Load

The dynamic equations for a load with a constant resistance R_L and a constant inductance L_L are

$$\frac{di_{Ld}}{dt} = \Omega i_{Lq} + \frac{v_{Ld} - R_L i_{Ld}}{L_L} \tag{3.23}$$

43

$$\frac{di_{Lq}}{dt} = -\Omega i_{TLMd} + \frac{v_{Lq} - R_L i_{Lq}}{L_L} \tag{3.24}$$

The port inputs to the load module that will be determined by its connection to the rest of the system are the voltages connected to the load. In the form given by (3.1),

$$\mathbf{x}_k = \begin{bmatrix} i_{Ld} & i_{Lq} \end{bmatrix}^T, \mathbf{u}_k = \begin{bmatrix} \ \end{bmatrix}, \mathbf{m}_k = \begin{bmatrix} \ \end{bmatrix}, \mathbf{p}_k = \begin{bmatrix} v_{Ld} & v_{Lq} \end{bmatrix}^T \tag{3.25}$$

3.1.5.   Synchronous Machine with Governor and Exciter Control

Most synchronous machines in industry today have governor and exciter controllers. The governor controller adjusts the steam valve position, changing the mechanical torque, in order to regulate the angular velocity of the machine to 377 rad/sec (60 Hz) [5]. For interconnected systems with no governor control on synchronous machines, the grid frequency depends on the parameters of the system and is not necessarily 60 Hz [12]. The exciter controller adjusts the rotor voltage in order to regulate the terminal voltage (the magnitude of the stator voltages) to a desired set point [56].

The dynamic equations used in this thesis for a synchronous machine with governor and exciter control are (3.2)-(3.7) and

$$\frac{d\tau_M}{dt} = -\frac{\tau_M + K_t a}{T_u} \tag{3.26}$$

$$\frac{da}{dt} = -\frac{K_P\left(\omega - \omega^{ref}\right) + K_I \omega_{Int} + ra}{T_g} \tag{3.27}$$

$$\frac{d\omega_{Int}}{dt} = \omega - \omega^{ref} \tag{3.28}$$

$$\frac{dv_R}{dt} = K_e\left(v_{Terminal}{}^{ref} - \sqrt{v_{Sd}{}^2 + v_{Sq}{}^2}\right) \tag{3.29}$$

For the governor control, a proportional integral controller is used and a denotes the valve position. The integral gain causes ω to converge to ω^{ref} with zero steady-state error. For the exciter control, a simple proportional controller is used in order to regulate the terminal voltage. Alternate, more complex exciter controllers are given in [56]. In the form given by (3.1),

44

$$\mathbf{x}_k = \begin{bmatrix} i_{Sd} & i_{Sq} & i_{Rd} & i_{Rq} & \omega & \theta & a & \omega_{Int} & v_R \end{bmatrix}^T, \mathbf{u}_k = \begin{bmatrix} \ \end{bmatrix}, \mathbf{m}_k = \begin{bmatrix} \ \end{bmatrix}, \mathbf{p}_k = \begin{bmatrix} v_{Sd} & v_{Sq} \end{bmatrix}^T \quad (3.30)$$

3.1.6. Variable Speed Drive for Flywheels

The dynamic equations for the flywheel variable speed drive controller connected to an infinite bus were derived in Section 2.2.2. Now instead of connecting to an infinite bus, consider connecting the variable speed drive to other dynamic components in an interconnected power grid. The dynamic equations are

$$\frac{di_{1d}}{dt} = i_{1q}\Omega + \frac{v_{1d}}{L_1} - \frac{R_1}{L_1}i_{1d} - \frac{q_{C1}u_{1d}}{2C_1L_1} \tag{3.31}$$

$$\frac{di_{1q}}{dt} = -i_{1d}\Omega + \frac{v_{1q}}{L_1} - \frac{R_1}{L_1}i_{1q} - \frac{q_{C1}u_{1q}}{2C_1L_1} \tag{3.32}$$

$$\frac{dq_{C1}}{dt} = \frac{i_{1d}u_{1d}}{2} + \frac{i_{1q}u_{1q}}{2} - \frac{i_{S2d}u_{2d}}{2} - \frac{i_{S2q}u_{2q}}{2} - \frac{q_{C1}}{C_1R_{C1}} \tag{3.33}$$

$$\frac{d\mathbf{I}_2}{dt} = inv(\mathbf{L}_2)\left(\mathbf{V}_2 - \mathbf{R}_2\mathbf{I}_2 - \mathbf{\Omega}_2\mathbf{L}_2\mathbf{I}_2\right) \tag{3.34}$$

$$\frac{d\omega_2}{dt} = \frac{\tau_{e2} - \tau_{M2} - B_2\omega_2}{J_2} \tag{3.35}$$

$$\frac{d\theta_2}{dt} = \omega_2 \tag{3.36}$$

where

$$\mathbf{I}_2 = \begin{bmatrix} i_{S2d} \\ i_{S2q} \\ i_{R2} \end{bmatrix}, \quad \mathbf{V}_2 = \begin{bmatrix} v_{S2d} \\ v_{S2q} \\ v_{R2} \end{bmatrix}, \quad \mathbf{R}_2 = \begin{bmatrix} R_{S2} & 0 & 0 \\ 0 & R_{S2} & 0 \\ 0 & 0 & R_{R2} \end{bmatrix},$$

$$\mathbf{L}_2 = \begin{bmatrix} L_{S2} + L_{SS2} & 0 & \sqrt{\frac{3}{2}}M_2 \\ 0 & L_{S2} + L_{SS2} & 0 \\ \sqrt{\frac{3}{2}}M_2 & 0 & L_{R2} \end{bmatrix}, \quad \mathbf{\Omega}_2 = \begin{bmatrix} 0 & -\omega_2 & 0 \\ \omega_2 & 0 & 0 \\ 0 & 0 & 0 \end{bmatrix} \tag{3.37}$$

$$\tau_e = \sqrt{\frac{3}{2}} M_2 i_{R2} i_{Sq2}$$ (3.38)

$$v_{S2d} = \frac{q_{C1} u_{2d}}{2C_1} \quad, \quad v_{S2q} = \frac{q_{C1} u_{2q}}{2C_1}$$ (3.39)

The port inputs to the variable speed drive module that will be determined by its connection to the rest of the system are the voltages connected to the variable speed drive. In the form given by (3.1),

$$\mathbf{x}_k = \begin{bmatrix} i_{1d} & i_{1q} & q_{C1} & i_{S2d} & i_{S2q} & i_{R2} & \omega_2 & \theta_2 \end{bmatrix}^T, \mathbf{u}_k = \begin{bmatrix} u_{1d} & u_{1q} & u_{2d} & u_{2q} \end{bmatrix}, \mathbf{m}_k = \begin{bmatrix} \ \end{bmatrix}, \mathbf{p}_k = \begin{bmatrix} v_{1d} & v_{1q} \end{bmatrix}^T$$ (3.40)

It should be noted that for transforming the quantities on the left side (the power electronics side) of the converter, a *dq* reference frame with an arbitrary angle ϕ and a corresponding velocity $\Omega = d\phi/dt$ is used, as for the previous modules. However, for the quantities on the right side (the flywheel side) of the converter, a *dq* reference frame fixed to the synchronous machine rotor is used ($\phi = \theta_2$). It is acceptable to use a different frame for the flywheel side than for the rest of the power grid because only the power electronics side, not the flywheel side, of the variable speed drive is ever directly connected to the rest of the power grid.

It should also be noted that for the variable speed drive, neither the mechanical torque nor the voltage applied to the rotor winding is considered a controllable input. It is assumed that there is no governor or exciter controller for the synchronous machine with the flywheel. The only controllable inputs for the variable speed drive are the duty ratios of the switch positions in the power electronics.

3.2. Combining Modules for Interconnected Power System

When combining the modules, the port inputs to one module are expressed in terms of the state variables of its connecting modules. This allows the dynamics of each module to be expressed as

$$\dot{\mathbf{x}}_k = \mathbf{f}_k(x_k, x_{ck}, u_k, m_k)$$ (3.41)

where $\mathbf{x}_{ck}$ is the vector of state variables in modules adjacent to module *k*.

46
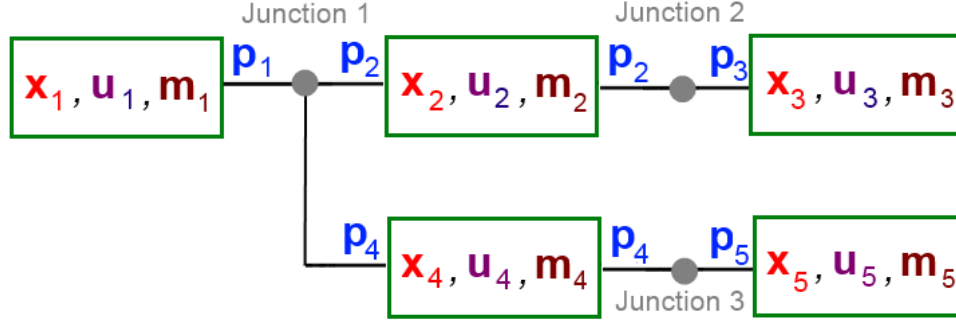
Figure 3.4: Example interconnected system. A junction is defined as the intersection of two or more ports.

The interconnection of modules can be represented as a graph, as shown in Figure 3.4. A junction is defined as the intersection of two or more ports. For a junction with C connecting ports, there are $2C$ relevant equations. There is one KCL constraint at each junction, involving each of the port currents of the connecting ports. There are $C-1$ independent voltage constraints at each junction, setting the port voltages of all connecting ports equal. Finally, there are C dynamic equations, governing the dynamics of the port states of all connecting ports. Let C_q denote the number of port state charges and C_i denote the number of port state currents (where $C_q + C_i = C$). At a junction, there can either be an all-inductor cutset or an all-capacitor loop. An all-inductor cutset occurs when all port states at the junction are currents. All-capacitor loops occur when multiple port states at the junction are charges. In order to express the dynamics in the form given by (3.41), it is necessary to iterate through each junction. For each junction, it is first necessary to determine whether there is an all-inductor cutset or all-capacitor loop at the junction, and then the procedure outlined below for each case can be followed.

Case 1: *No All-Inductor Cutsets or All-Capacitor Loops* This case occurs when $C_q = 1$. If a junction does not contain an all-inductor cutset or an all-capacitor loop, the port inputs at that junction can be re-expressed in terms of the port states at that junction. The one KCL constraint can be used to solve for the one port input current. The $C-1$ voltage constraints can be used to solve for the $C-1$ port input voltages. Then the expressions for the one port input current and the $C-1$ port input voltages can be substituted into the C dynamic equations.

Case 2: *All-Capacitor Loops.* This case occurs when $C_q > 1$. The number of all-capacitor loops at the junction is given by $C_q - 1$. In this case, one port state charge is chosen to be the independent charge and the other $C_q - 1$ port state charges at that junction are chosen to be dependent charges and must be substituted out of the model. The expression to substitute in for each dependent charge is obtained from the voltage constraint equations. The derivative of each dependent charge must also be replaced by the derivative of that expression. After all dependent charges have been substituted for, a system of equations, which consists of the one KCL equation and the C_q dynamic equations for the port state charges, is obtained. This system needs to be solved for the derivative of the one independent port state charge and the C_q port input currents. This will yield the derivative of the independent charge in terms of only the state variables (and not the port input currents). Next the voltage constraints are used to solve for the C_i port input voltages in terms of the independent port state charge. Finally, the expressions for the C_i port input voltages are substituted into the dynamic equations for the C_i port state currents.

Case 3: *All-Inductor Cutsets.* This case occurs when $C_q = 0$. In this case, one port state current is chosen to be the dependent current and must be substituted out of the model. The expression to substitute in for the dependent current is obtained from the KCL constraint. The derivative of the dependent current must also be replaced by the derivative of that expression. After the dependent current has been substituted for, a system of equations, which consists of the $C - 1$ voltage constraints equations and the C dynamic equations, is obtained. This system needs to be solved for the derivatives of the $C - 1$ independent currents and the C port input voltages. This will yield the derivative of the $C - 1$ independent port state currents in terms of only the state variables (and not the port input voltages).

Several advantages of this modular methodology should be noted. First, this methodology enables the system operator to form the state space model for the interconnected system without needing to know details of how the individual module dynamics are derived. This allows for privacy of detailed machine design, since the owner of each module needs to only give the system operator the dynamic model in the

form given by (3.1) . Also this approach provides a basis for common information modeling exchange between different stakeholders (owners of different components) and entities responsible for dynamic operations of the interconnected grid (system operators).

Also, to convert each module's dynamics from (3.1) to (3.41) requires only information about the dynamics of its connecting modules and not the entire power system. Hence, that makes this modular approach scalable to large systems. Since the same procedure is repeated for each junction, the computational intensity only increases linearly as the number of junctions increases.

3.3. Automated Modular State Space Model Derivation Methodology

The algorithm described in the previous section was implemented in MATLAB using an object-oriented approach. Each component type (synchronous machine, induction machine, transmission line, etc.) is defined as a MATLAB class, which is a subclass of the class "PowerSystemModule." The properties of the "PowerSystemModule" class are shown in Table 3.1.

Each subclass has these same properties, although the values and vector sizes of these properties vary for each type of component. The constructor for each subclass takes as input the module index name, which is supplied by the user. For the first nine properties in Table 3.1, symbolic names are already defined for each subclass and the module index name is appended to the end of those names. For example, as given in Section 3.1.1, the state variables for the synchronous machine class are i_{Sd}, i_{Sq}, i_R, ω, and θ. Therefore, if a module index name of '1' is given, the property **StateVariables** for that specific synchronous machine object would be i_{Sd1}, i_{Sq1}, i_{R1}, ω_1, and θ_1.

There is also another class called "PowerSystem." Its constructor takes as input all the modules and the incidence matrix, which describes how the modules are interconnected. The "PowerSystem" class has, in its constructor, a method "ProduceStateSpace," which solves for the dynamic equations of the interconnected power system in the standard state space form shown by (3.41). The "ProduceStateSpace" method follows the methodology described in the previous section. It should be noted that for computational efficiency, only all-capacitor loops are checked for at each junction, not all-inductor cutsets. The reason for this is because, with the models used in this paper, there will never be any all-

inductor cutsets. When the pi model of the transmission line is used and there are always transmission lines between buses, there will never be any all-inductor cutsets between modules. When using the pi model of the transmission line, the port states of the transmission line are charges. Hence, for each junction, it is guaranteed that $C_q \geq 1$.

Table 3.1: Properties of "PowerSystemModule" class

Properties	Description
StateVariableDerivatives	1xN vector with the names of the N state variable time derivatives for that module
StateVariables	1xN vector with the names of the N state variables for that module
PortInputs	1xP vector with the names of the P port inputs for that module
Parameters	a vector with the names of the parameters for that module
ControllableInputs	a vector with the names of the controllable inputs for that module
PortCurrents	1xP vector with the names of the P port currents for that module
PortVoltages	1xP vector with the names of the P port voltages for that module
PortStates	1xP vector with the names of the P port states for that module
PortStateDerivatives	1xP vector with the names of the P port state derivatives for that module
PortStateTypes	1xP vector with the types of state variable (either "Charge" or "Current" at each of the P ports)
StateSpace	Nx1 vector of dynamic equations for that module.

To provide information about the power system, the user should take the following steps:

1. Define a unique index name for each module.

2. For each module, create an object of the proper class, using the index name, the angular position of the *dq* reference frame, and the angular velocity of the *dq* reference frame when calling its constructor. (This angular position and velocity should be common for all modules so that the KCL and KVL at the junctions between modules hold true.)

3. Combine all objects into one cell array called **Modules**.

4. Form the incidence matrix **G**, which describes how the ports of the modules are connected. The size of **G** is the number of junctions between modules by the total number of ports of all modules.

5. Create an instance of the "PowerSystem" class, using **G** and **Modules** as input when calling its constructor.

This modular method is much more user-friendly than the centralized method presented in the previous chapter. When using the centralized method, it is necessary for the user to specify every branch of the electrical subsystem and specify the connection of all branches. Using the modular approach, it is only necessary for the user to specify modules and the connections between modules.

3.4. Modular Modeling Examples

3.4.1. Example without All-Capacitor Loops

To demonstrate the automated modular approach, first a simple two-bus power system without any all-capacitor loops, shown in Figure 3.5, is considered. This power system can be divided into three modules as shown by Figure 3.6. Index names for each module are assigned as shown in Figure 3.6, and for each of the three modules, objects of the appropriate class are created. The object names for each module are also shown in Figure 3.6. The port inputs to each module are shown in blue while the port states of each module are shown in red.
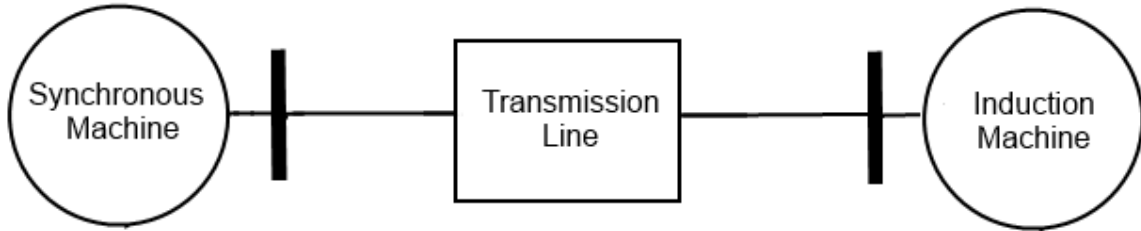
Figure 3.5: Example power system without any all-capacitor loops on which the modular approach is demonstrated.

Next, all the objects are combined into one cell array.

$$\textbf{Modules} = \{SM, TL, IM\} \tag{3.42}$$

The incidence matrix **G** that specifies the interconnection of the modules is given by

$$\mathbf{G} = \begin{bmatrix} 1\ 0 & 1\ 0\ 0\ 0 & 0\ 0 \\ 0\ 1 & 0\ 1\ 0\ 0 & 0\ 0 \\ 0\ 0 & 0\ 0\ 1\ 0 & 1\ 0 \\ 0\ 0 & 0\ 0\ 0\ 1 & 0\ 1 \\ \underbrace{}_{SM} & \underbrace{}_{TL} & \underbrace{}_{IM} \end{bmatrix} \tag{3.43}$$

51
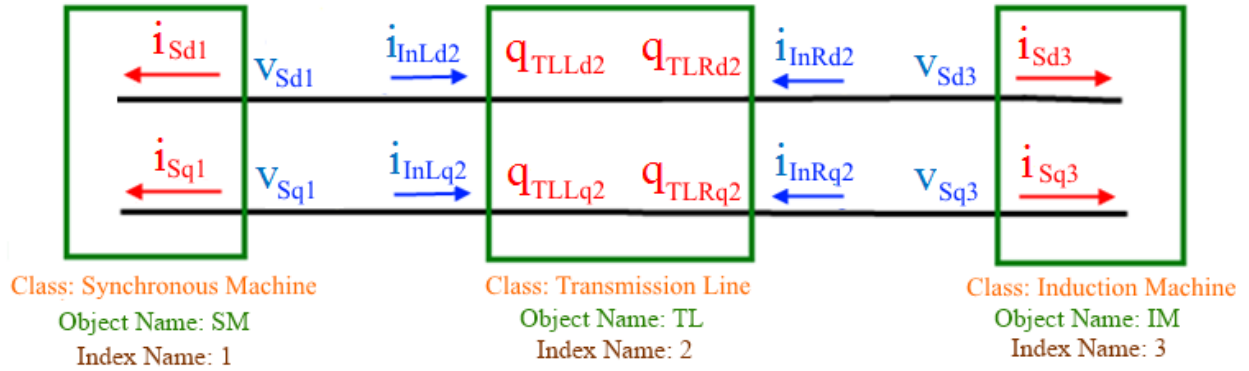
Figure 3.6: Division of the power system shown in Figure 3.5 into three modules. The port inputs to each module are shown in blue while the port states of each module are shown in red.

Finally, an object of the "PowerSystem" class is created using **Modules** and **G** as inputs. Figure 3.7 shows the MATLAB input file used to generate the state space equations for this example.

```
SMIndexName = {'1'};
SM = SynchronousMachine(SMIndexName,phi,dphidt);

TLIndexName = {'2'};
TL = TransmissionLine(TLIndexName,phi,dphidt);

IMIndexName = {'3'};
IM = InductionMachine(IMIndexName,phi,dphidt);

Modules = {SM,TL,IM};
G = [1 0   1 0 0 0   0 0
     0 1   0 1 0 0   0 0
     0 0   0 0 1 0   1 0
     0 0   0 0 0 1   0 1 ];
PS = PowerSystem(G,Modules);
```

Figure 3.7: Input file for the modular method for the example shown in Figure 3.5.

The state space equations for the interconnected power system are symbolically solved for using the "ProduceStateSpace" method in the constructor of the "PowerSystem" object. At each of the four junctions, since there is not an all-capacitor loop, using the KCL equation and the voltage constraint equation at each junction, the port inputs are found in terms of the state variables of the connecting modules.

$$v_{Sd1} = q_{TLLd2} / C_{TL2} \ , \ i_{InLd2} = -i_{Sd1} \tag{3.44}$$

$$v_{Sq1} = q_{TLLq2} / C_{TL2} \ , \ i_{InLq2} = -i_{Sq1} \tag{3.45}$$

$$v_{Sd3} = q_{TLRd2} / C_{TL2} \ , \ i_{InRd2} = -i_{Sd3} \tag{3.46}$$

$$v_{Sq3} = q_{TLRq2} / C_{TL2} \ , \ i_{InRq2} = -i_{Sq3} \tag{3.47}$$

After making these substitutions into the differential equations for each module, the form shown by

(3.41) is obtained. The CPU time of the automated method is 16 seconds. By comparison, for the same

system, using the methodology described in Section 2.2.1, the computational time for deriving the state

space equations was 13 minutes [12].

3.4.2.   Example with All-Capacitor Loops

Next, a larger more complex power system, shown in Figure 3.8, with all-capacitor loops between

components is considered. This power system can be divided into seven modules, as shown by Figure

3.9. Index names for each module are assigned as shown in Figure 3.9, and for each of the seven

modules, objects of the appropriate class are created. The object names for each module are also shown

in Figure 3.9. Next, all the objects are combined into one cell array.

$$\textbf{Modules} = \{SM1, TL1, IM1, TL2, SM2, Load1, TL3\} \tag{3.48}$$
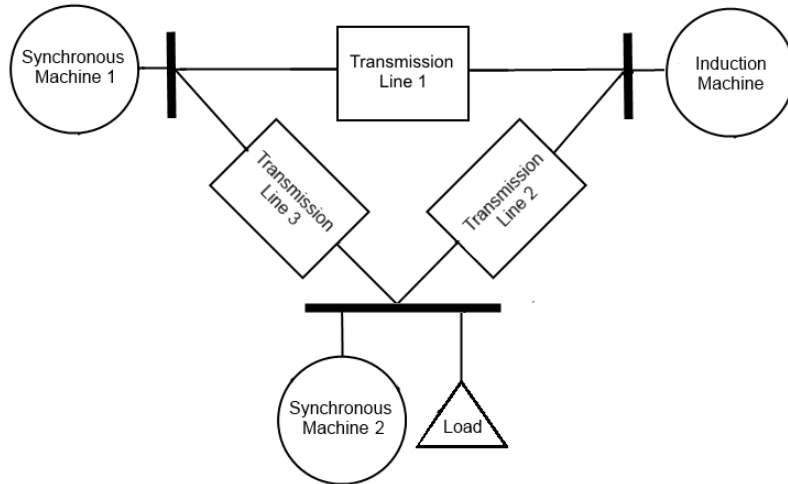
Figure 3.8: Example power system with all-capacitor loops on which the modular approach is demonstrated.
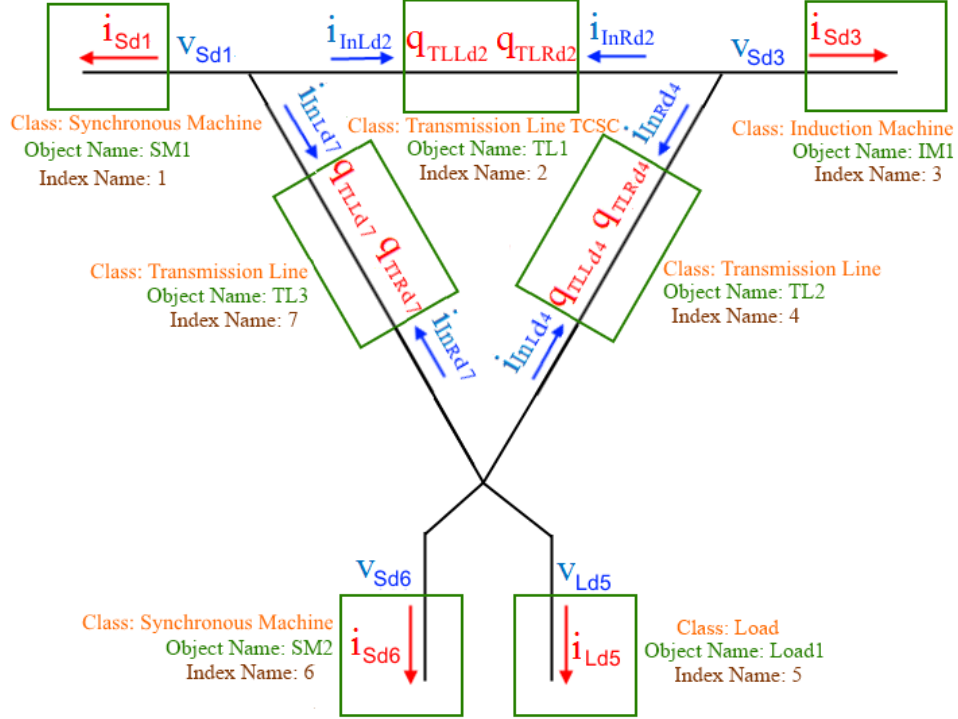
Figure 3.9: Division of the power system shown in Figure 3.8 into seven modules. The port inputs to each module are shown in blue while the port states of each module are shown in red. Only the d-phase is shown here, but the q-phase is equivalent.   .

The incidence matrix **G** that specifies the interconnection of the modules is given by

$$
\mathbf{G} = \begin{bmatrix}
1\ 0 & 1\ 0\ 0\ 0 & 0\ 0 & 0\ 0\ 0\ 0 & 0\ 0 & 0\ 0 & 1\ 0\ 0\ 0 \\
0\ 1 & 0\ 1\ 0\ 0 & 0\ 0 & 0\ 0\ 0\ 0 & 0\ 0 & 0\ 0 & 0\ 1\ 0\ 0 \\
0\ 0 & 0\ 0\ 1\ 0 & 1\ 0 & 0\ 0\ 1\ 0 & 0\ 0 & 0\ 0 & 0\ 0\ 0\ 0 \\
0\ 0 & 0\ 0\ 0\ 1 & 0\ 1 & 0\ 0\ 0\ 1 & 0\ 0 & 0\ 0 & 0\ 0\ 0\ 0 \\
0\ 0 & 0\ 0\ 0\ 0 & 0\ 0 & 1\ 0\ 0\ 0 & 1\ 0 & 1\ 0 & 0\ 0\ 1\ 0 \\
0\ 0 & 0\ 0\ 0\ 0 & 0\ 0 & 0\ 1\ 0\ 0 & 0\ 1 & 0\ 1 & 0\ 0\ 0\ 1 \\
\underbrace{}_{SM1} & \underbrace{}_{TL1} & \underbrace{}_{IM1} & \underbrace{}_{TL2} & \underbrace{}_{Load1} & \underbrace{}_{SM2} & \underbrace{}_{TL3}
\end{bmatrix} \tag{3.49}
$$

An object of the "PowerSystem" class is created using **Modules** and **G** as inputs, and the state space equations for the interconnected power system are symbolically solved for using the "ProduceStateSpace" method. To demonstrate why it is necessary to check each junction for all-capacitor loops and to remove a state variable for each all-capacitor loop, the junction between the d-phases of $SM1$, $TL1$, and $TL3$ is considered. An all-capacitor loop is detected at this junction because two objects at this junction ($TL1$ and $TL3$) have port state charges. At this junction, the one KCL equation is

$$
i_{InLd2} + i_{InLd7} + i_{Sd1} = 0 \tag{3.50}
$$

54

The two independent voltage constraint equations are

$$v_{Sd1} = q_{TLLd2} / C_{TL2} \tag{3.51}$$

$$q_{TLLd2} / C_{TL2} = q_{TLLd7} / C_{TL7} \tag{3.52}$$

The dynamic equations of the port states at this junction are

$$\frac{di_{Sd1}}{dt} = f_1\left(\mathbf{x}_1, v_{Sd1}\right) \tag{3.53}$$

$$\frac{dq_{TLLd2}}{dt} = f_2\left(\mathbf{x}_2, i_{InLd2}\right) \tag{3.54}$$

$$\frac{dq_{TLLd7}}{dt} = f_3\left(\mathbf{x}_7, i_{InLd7}\right) \tag{3.55}$$

where $\mathbf{x}_1$, $\mathbf{x}_2$, and $\mathbf{x}_7$ are the state variables of objects *SM*1, *TL*1, and *TL*3 respectively.

Unlike the previous example, since there is all-capacitor loop, it is not possible to solve (3.50)-(3.52) for the port inputs v_{Sd1}, i_{InLd2}, and i_{InLd7} in terms of the state variables. Therefore, it is necessary to eliminate a state variable from the all-capacitor loop. q_{TLLd7} is chosen to be the state variable removed from the model and the following expressions algebraic expressions are obtained for q_{TLLd7} and $\frac{dq_{TLLd7}}{dt}$.

$$q_{TLLd7} = \frac{C_{TL7}}{C_{TL2}} q_{TLLd2} \tag{3.56}$$

$$\frac{dq_{TLLd7}}{dt} = \frac{C_{TL7}}{C_{TL2}} \frac{dq_{TLLd2}}{dt} \tag{3.57}$$

Substituting (3.57) into (3.55) yields

$$\frac{dq_{TLLd2}}{dt} = \frac{C_{TL2}}{C_{TL7}} f_3\left(\mathbf{x}_7, i_{InLd7}\right) \tag{3.58}$$

Equations (3.50), (3.54), and (3.58) can now be solved for $\frac{dq_{TLLd2}}{dt}$, i_{InLd2}, and i_{InLd7} (in order to yield $\frac{dq_{TLLd2}}{dt}$ independent of the port inputs i_{InLd2} and i_{InLd7}). Finally, substituting (3.51) into (3.53) yields $\frac{di_{Sd1}}{dt}$ independent of the port input v_{Sd1}.

This same logic is used for the other five junctions, and the differential equations in the form shown by (3.41) are obtained. Since there are six all-capacitor loops, six port state variables (q_{TLLd7} , q_{TLLq7} , q_{TLRd7} , q_{TLRq7} , q_{TLRd4} , and q_{TLRq4}) are eliminated from the model. The CPU time of the automated method is 31 seconds.

3.5. Alternate Distributed Computing Implementation

The automated methodology discussed in Section 3.3 has one centralized object (the "PowerSystem" object), which is given the connection between all modules and solves for the interconnected state space system. There are two drawbacks with this approach. First, even though the same procedure is repeated for each junction, this method cannot be run in a distributed manner using multiple processors. Second, this approach requires that the "PowerSystem" object know the connection between all modules in the grid. For large power systems, it may not be realistic that one entity knows the entire power system topology.

In this section, an alternative distributed methodology is described, where each object is run in parallel on different processors, and TCP/IP (Transmission Control Protocol/Internet Protocol) communication is used to exchange information between the different processors [57] . Each module sends their port information to their connecting buses and each bus, in parallel, solves the KCL and KVL equations at that bus in order to re-express the port inputs at that bus in terms of the port states at that bus. Communication is only needed between each module and their connecting buses. Using this distributed methodology, each bus only needs to know what modules are connected to that bus, and there is no centralized object that needs to know the entire topology of the power system.

As in Section 3.3, MATLAB classes are defined for each component with their corresponding dynamic equations. The constructor for each dynamic module class takes as input the module index name, the rotating reference frame position ϕ , the rotating reference frame speed $d\phi/dt$, and the TCP/IP mailboxes that will be used to communicate with other objects on different processors.

Now, a "Bus" MATLAB class is also implemented. The constructor for the bus class takes as input the TCP/IP mailboxes that will be used to communicate with other objects. Tables 3.2 and 3.3 show the communicated data, the learned data, and the class methods for the "Synchronous Machine" class and the "Bus" class respectively. (The data structures for the other dynamic module classes are similar to the "Synchronous Machine" class.) These tables show the flow of information and communication between a dynamic module object and a bus object.

First, each dynamic module object, in parallel, communicates their port states, port inputs, port currents, port voltages, port state types, and port state dynamic equations to their connecting bus objects. Then, each bus object uses that information to solve for the port inputs at that bus in terms of the state variables using the methodology described in Section 3.2. Each bus object can do this in parallel. If there is an all-capacitor loop at a bus, then one of the capacitor charges at the bus is a dependent state and must be eliminated as a state variable. The bus object finds an algebraic expression in terms of the independent charge to substitute for the dependent charge.

Table 3.2: "Synchronous Machine" class data structure

Communicated Data:	Port States: i_{Sd}, i_{Sq} Port Inputs: v_{Sd}, v_{Sq} Port Currents: i_{Sd}, i_{Sq} Port Voltages: v_{Sd}, v_{Sq} Port State Types: "Current", "Current" Port State Dynamic Equations: $\dfrac{di_{Sd}}{dt} = f_{k1}(x_k, p_k, u_k, m_k),$ $\dfrac{di_{Sq}}{dt} = f_{k2}(x_k, p_k, u_k, m_k)$
Learned Data:	Port Input Expressions: port input expressions in terms of state variables of connecting modules Dependent States: state variables which are dependent and can be expressed as an algebraic function of state variables of connecting modules Dependent State Expressions: expressions for dependent state variables in terms of state variables of connecting modules
Methods:	ReExpressPortInputs: substitutes Port Input Expressions for Port Inputs in the state space model ReExpressDependentState: substitutes Dependent State Expressions for Dependent States in the state space model EliminateDependentState: eliminates dynamic equations for Dependent States in the state space model

Table 3.3: "Bus" class data structure

Communicated Data:	Port Input Expressions: port input expressions in terms of state variables of connecting modules Dependent States: state variables which are dependent and can be expressed as an algebraic function of the state variables of connecting modules Dependent State Expressions: expressions for dependent state variables in terms of state variables of connecting modules
Learned Data:	Port States: all port state variables at the bus Port Inputs: all port inputs at the bus Port Voltages: all port voltages at the bus Port Currents: all port currents at the bus Port State Types: all port state variable types ("Charge" or "Current") at the bus Port State Dynamic Equations: all port state dynamic equations at the bus
Methods:	CheckForAllCapacitorLoop: Determines if there is an all-capacitor loop at the bus. If there is, this method solves for the dependent state charges in terms of the independent state charges and then communicates Dependent States and Dependent State Expressions to the proper dynamic modules at the bus ReExpressPortInputs: Uses the KCL and KVL equations to solve for Port Inputs at the bus in terms of Port States at the bus. This method then communicates Port Input Expressions to each connecting dynamic module.

The bus objects then communicate to the connecting dynamic module objects either the port input expressions or the dependent states and the dependent state expressions. Finally, each dynamic module object uses that information to substitute their port inputs in terms of the port input expressions in the state space model or to, if necessary, eliminate a dependent state variable from the state space model. Each dynamic module object can also do this in parallel.

This distributed method is demonstrated on the two-bus power system example shown in Figure 3.5 and discussed in Section 3.4.1. This power system can be divided into three dynamic module objects and two bus objects as shown by Figure 3.10. Objects of the appropriate class are created on different processors. The object names for all dynamic modules and buses, as well as the index names for each dynamic module, are shown in Figure 3.10.
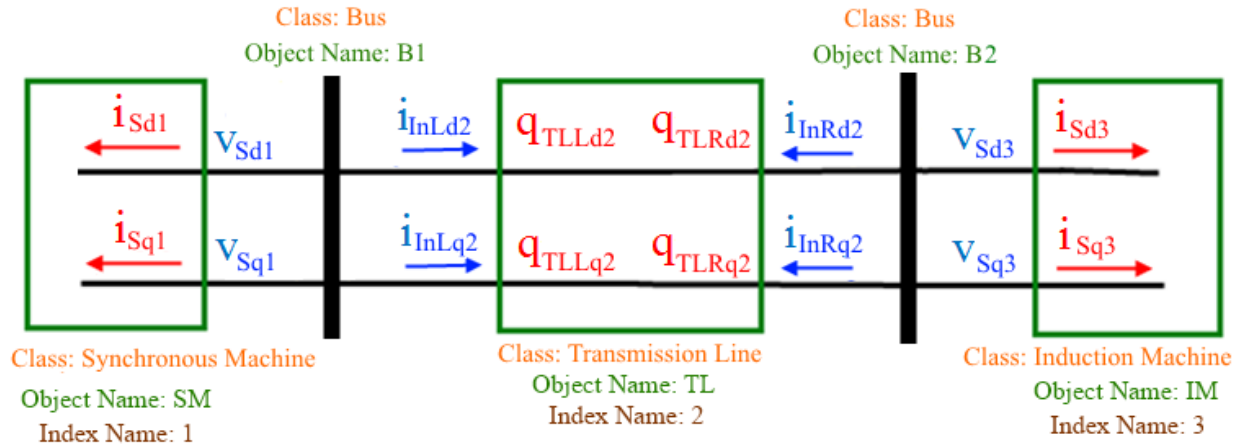
Figure 3.10: Division of the power system shown in Figure 3.5 into three dynamic module objects and two bus objects.

Bus object *B1* communicates with dynamic module objects *SM* and *TL* while bus object *B2* communicates with dynamic module objects *TL* and *IM* through TCP/IP communication. Figure 3.11 shows the initialization of all the objects in MATLAB, as well as the initialization of their TCP/IP communication.

```
SMIndexName = {'1'};
Mailbox1 = TCPIPMailbox('0.0.0.0',30001,'server');
SM = SynchronousMachine(SMIndexName,phi,dphidt,Mailbox1);

Mailbox1 = TCPIPMailbox('127.0.0.1',30001,'client');
Mailbox2 = TCPIPMailbox('127.0.0.1',30002,'client');
MailboxMatrix = [Mailbox1;Mailbox2];
B1 = Bus(MailboxMatrix);

TLIndexName = {'2'};
Mailbox2 = TCPIPMailbox('0.0.0.0',30002,'server');
Mailbox3 = TCPIPMailbox('0.0.0.0',30003,'server');
MailboxMatrix = [Mailbox2 ; Mailbox3];
TL = TransmissionLine(TLIndexName,phi,dphidt,MailboxMatrix);

Mailbox3 = TCPIPMailbox('127.0.0.1',30003,'client');
Mailbox4 = TCPIPMailbox('127.0.0.1',30004,'client');
MailboxMatrix = [Mailbox3;Mailbox4];
B2 = Bus(MailboxMatrix);

IMIndexName = {'3'};
Mailbox4 = TCPIPMailbox('0.0.0.0',30004,'server');
IM = InductionMachine(IMIndexName,phi,dphidt,Mailbox4);
```

Figure 3.11: Initialization of all objects in Figure 3.10 and the initialization of the TCP/IP communication.

59

The same interconnected state space model is formed as in Section 3.4.1, and (3.44)-(3.47) are used in order to express the port inputs at each bus in terms of the port states at each bus. The computational time of the automated distributed method is 29 seconds. It should be noted that all processors were run on one computer, so the computational time could be improved by using multiple computers.

3.6. Summary

This chapter presented a new automated modular approach for deriving the state space model for power systems. Using this modular approach, first dynamic models for each power system component are derived using the Lagrangian approach and then given the connection between modules, the dynamic models of each module are combined in an automated procedure. This modular approach is much more computationally efficient and suitable for large power systems than the centralized approach described in Chapter 2. This chapter concludes the discussion of the modeling of power systems, and the next five chapters will discuss the control design using flywheels.

4. Automated Passivity-Based Control

Once the dynamic model of the power system has been obtained, the next step is design the control using flywheels. This chapter introduces passivity-based control, as well as details a novel automated method for symbolically deriving the passivity-based control law. Chapter 5 will describe a variable speed drive controller for flywheels using passivity-based control logic.

In industry today, most controllers in power systems and power electronics use linearized models of nonlinear dynamics and linear control logic [5,46,58,59]. While these linearized models are accurate for small disturbances, large disturbances can perturb the system far away from the equilibrium where linearized models are no longer accurate. Some common nonlinear control techniques include variable structure control [9], Lyapunov-based control [60], and feedback linearization [61]. However, none of these nonlinear control techniques take advantage of the intrinsic physical structure and energy properties of the system dynamics.

Passivity-based control exploits these intrinsic energy properties when designing control for stabilization or regulation [14] and for this reason, enhanced robustness against parameter uncertainty and simplified controller implementation are achieved with passivity-based control compared to feedback linearization, due to the avoidance of exact cancellation of nonlinearities [41]. Previous work on passivity-based control has been demonstrated for robot arms [14], dc/dc converters [14,62,63], one-phase ac/dc converters [64], three-phase ac/dc converters [41], torque regulation of induction motors [14,65], and speed regulation of Boost-converter driven dc-motors [66].

As outlined in [67], two basic approaches for passivity-based control have been explored in previous literature. In the first approach, the desired closed-loop storage function is chosen first and then the controller is designed to ensure this objective [14]. In the second, newer approach, the closed-loop storage function is obtained as a result of the interconnection of the controller and the plant to be controlled [68]. Using this approach, the plant and the controller can be both modelled as Port-Hamiltonian systems, and the resulting closed-loop storage function has the nice physical interpretation of the sum of the energy of the plant to be controlled and the energy of the controller [68]. Unfortunately,

this approach hinges on the ability to solve a partial differential equation (PDE) and explicit conditions for the existence of solutions to the PDE cannot be found in general [68]. As a result, no automated or systematic procedure can be designed to derive the control law. Therefore, the first approach, where the desired closed-loop energy functions are chosen beforehand, is used in this thesis because that approach lends itself to a systematic and automated procedure for deriving the control law. The ability to automate the control law derivation is strongly desired because it is allows for quick testing of different closed-loop system behavior and different set point equations, and deriving the control law by hand is a complex and tedious procedure even for small systems.

Extending the previous literature on passivity-based control, this chapter describes a novel automated method for symbolically deriving the passivity-based control law for electrical systems. This is the first computer-aided tool for symbolically designing passivity-based control. In the automated method, the user specifies the original state space model, the set point equations, the desired closed-loop energy function, and the desired closed-loop dissipation function, and the automated method symbolically derives the control law.

The automated method is then demonstrated for regulation of the three-phase ac/dc/ac converter, which was introduced in Section 2.1.2. Simulation results are shown demonstrating the effectiveness of the passivity-based control for this example, and finally, the stability limits and the switch feasibility limits for this controller are derived and interpreted. The control logic derived for the ac/dc/ac converter is important because having a nonlinear state space representation of the dynamics and mathematical expressions for the duty ratios of the switches allow for control with provable performance.

4.1. Automated Control Law Derivation Methodology

For the automated control design methodology introduced in [16], the control designer specifies the original state space model, the set point equations, the closed-loop energy functions (the closed-loop magnetic co-energy and the closed-loop electric energy), and the closed-loop dissipation function, and the automated method symbolically derives the control law. The Lyapunov function for the closed-loop system is the sum of the closed-loop magnetic co-energy and the closed-loop electric energy. If the

closed-loop energy and dissipation functions are chosen so that the Lyapunov function is positive definite and the time derivative of the Lyapunov function is negative definite, then the error dynamics will be asymptotically stable and the state variables will converge to their desired values [69]. A function $f(x)$ is positive definite if $f(0) = 0$ and $f(x) > 0 \ \forall \, x \neq 0$, and $f(x)$ is negative definite if $f(0) = 0$ and $f(x) < 0 \ \forall \, x \neq 0$.

To specify the desired closed-loop behavior, the control designer should take the following steps:

1. Enter the original state space model $\dot{\mathbf{x}} = \mathbf{f}(x, u)$.

2. Choose a desired closed-loop magnetic co-energy $\tilde{W}_m{}'(\tilde{\mathbf{x}})$ and a desired closed-loop electric energy $\tilde{W}_e(\tilde{\mathbf{x}})$ where $\tilde{\mathbf{x}} = \mathbf{x} - \mathbf{x}^D$ and $\mathbf{x}^D$ denotes the desired state variables. For an underactuated system (a system with less control inputs than state variables), these desired state variables cannot be all arbitrarily selected, but rather will be determined later from the set point equations and the error dynamics [14]. The Lyapunov function of the closed-loop system is $V(\tilde{\mathbf{x}}) = \tilde{W}_m{}'(\tilde{\mathbf{x}}) + \tilde{W}_e(\tilde{\mathbf{x}})$, so $\tilde{W}_m{}'(\tilde{\mathbf{x}})$ and $\tilde{W}_e(\tilde{\mathbf{x}})$ should be chosen so that $V(\tilde{\mathbf{x}})$ is positive definite. It should be noted that the choices for $\tilde{W}_m{}'(\tilde{\mathbf{x}})$ and $\tilde{W}_e(\tilde{\mathbf{x}})$ are not unique.

3. Choose a desired closed-loop dissipation function $\tilde{\mathcal{R}}(\tilde{\mathbf{x}})$ which will ensure that $\dot{V}(\tilde{\mathbf{x}})$, computed in Step 4 by the computer, is negative definite. Again the choice for $\tilde{\mathcal{R}}(\tilde{\mathbf{x}})$ is not unique.

4. Form symbolic vectors for the current $\tilde{\mathbf{I}}$ and the charge $\tilde{\mathbf{Q}}$ of the closed-loop system.

5. Form the constraint matrix $\tilde{\mathbf{G}}$ for the closed-loop system. $\tilde{\mathbf{G}}\tilde{\mathbf{I}} = 0$ will give the KCL equations.

6. Form the Lagrange multiplier vector $\tilde{\boldsymbol{\Lambda}}$ for the closed-loop system, consisting of the voltages at the non-ground junctions.

7. Specify a vector of set point equations $\mathbf{f}_r(x^D) = \mathbf{r}^*$ where $\mathbf{r}^*$ is a vector of external set points and specify which desired state variables are being directly controlled. The number of set point

equations, as well as the number of directly controlled state variables, should match the number of controllable inputs in the systems.

Given the original state-space model $\dot{\mathbf{x}} = \mathbf{f}(x, u)$, the set point equations $\mathbf{f}_r(x^D) = \mathbf{r}^*$, and the desired closed-loop behavior specified by matrices $\tilde{W}_m'(\tilde{\mathbf{x}})$, $\tilde{W}_e(\tilde{\mathbf{x}})$, $\tilde{\mathbf{I}}$, $\tilde{\mathbf{Q}}$, $\tilde{\mathbf{G}}$, and $\tilde{\mathbf{\Lambda}}$, the computer solves for the passivity-based control law by taking the following steps:

1. Calculate the closed-loop Lagrangian

$$\tilde{\mathscr{L}}(\tilde{\mathbf{x}}) = \tilde{W}_m'(\tilde{\mathbf{x}}) - \tilde{W}_e(\tilde{\mathbf{x}}) \tag{4.1}$$

2. Obtain the error dynamic equations for the closed-loop system by evaluating the Lagrange equations of the first kind

$$\frac{d}{dt}\left[\frac{\partial \tilde{\mathscr{L}}}{\partial \tilde{\mathbf{I}}(k)}\right] - \frac{\partial \tilde{\mathscr{L}}}{\partial \tilde{\mathbf{Q}}(k)} + \frac{\partial \tilde{\mathscr{R}}}{\partial \tilde{\mathbf{I}}(k)} - \tilde{\mathbf{V}}(k) - \frac{\partial \tilde{\mathbf{\Lambda}}\tilde{\mathbf{G}}\tilde{\mathbf{I}}}{\partial \tilde{\mathbf{I}}(k)} = 0 \tag{4.2}$$

$$\tilde{\mathbf{G}}\tilde{\mathbf{I}} = 0 \tag{4.3}$$

$\tilde{\mathbf{V}}(k)$ is set to zero for all k because in order to make the error dynamics asymptotically stable there should be no closed-loop forcing function [41]. It should also be noted that because the Lagrange equations (4.2) do not hold in a rotating reference frame [70], the automated method converts $\tilde{\mathscr{L}}$ and $\tilde{\mathscr{R}}$ to the stationary αβ reference frame, then evaluates the Lagrange equations, and finally converts the dynamic equations back to the *dq* rotating reference frame.

3. Re-express the error dynamics given by (4.2) and (4.3) in standard state space form.

$$\dot{\tilde{\mathbf{x}}} = \tilde{\mathbf{f}}(\tilde{x}, u) \tag{4.4}$$

4. Compute and display the Lyapunov function and the time-derivative of the Lyapunov function

$$V(\tilde{\mathbf{x}}) = \tilde{W}_m'(\tilde{\mathbf{x}}) + \tilde{W}_e(\tilde{\mathbf{x}}) \tag{4.5}$$

$$\dot{V}(\tilde{\mathbf{x}}) = \frac{\partial V(\tilde{\mathbf{x}})}{\partial \tilde{\mathbf{x}}}\dot{\tilde{\mathbf{x}}} \tag{4.6}$$

In order to ensure that $\tilde{\mathbf{x}} \rightarrow 0$ ($\mathbf{x} \rightarrow \mathbf{x}^D$), $V(\tilde{\mathbf{x}})$ should be a positive definite function and $\dot{V}(\tilde{\mathbf{x}})$ should be a negative definite function. If this is not the case, the control designer can abort the automated method at this point and re-enter different closed-loop energy and dissipation functions.

5. Substitute in $\mathbf{x} - \mathbf{x}^D$ for $\tilde{\mathbf{x}}$ in the error dynamics given by (4.4)

$$\dot{\mathbf{x}} - \dot{\mathbf{x}}^D = \tilde{\mathbf{f}}(x - x^D, u) \tag{4.7}$$

6. Using the original state-space model, substitute $\mathbf{f}(x, u)$ in for $\dot{\mathbf{x}}$

$$\mathbf{f}(x, u) - \dot{\mathbf{x}}^D = \tilde{\mathbf{f}}(x - x^D, u) \tag{4.8}$$

For a system with N state variables and M controllable inputs, the controller has $N+M$ degrees of freedom (the M inputs and the N desired values $\mathbf{x}^D$). N equations result from (4.8) and the remaining M equations are the set point equations $\mathbf{f}_r(x^D) = \mathbf{r}^*$.

7. Solve (4.8) and the set point equations for the M inputs, the M directly controlled state variables, and the N-M derivatives of the non-directly controlled desired state variables.

$$\mathbf{u} = \mathbf{g_1}(x, x^{Dn}, r^*) \tag{4.9}$$

$$\dot{\mathbf{x}}^{Dn} = \mathbf{g_2}(x, x^{Dn}, r^*) \tag{4.10}$$

$$\mathbf{x}^{Dd} = \mathbf{g_3}(x, x^{Dn}, r^*) \tag{4.11}$$

where $\mathbf{x}^{Dd}$ and $\mathbf{x}^{Dn}$ represent the directly controlled desired state variables and the non-directly controlled desired state variables respectively. Since with an underactuated system all state variables cannot be controlled, the non-directly controlled desired state variables have dynamics. By adding (4.9) and (4.10) to the original state space model $\dot{\mathbf{x}} = \mathbf{f}(x, u)$, the closed-loop dynamics of the system with the controller can be simulated.

4.2. Example: AC/DC/AC Converter

Now the automated computer-aided control law derivation methodology is demonstrated for the ac/dc/ac converter, whose dynamics were derived in Section 2.1.2. The state-space model in the *dq*

reference frame for the ac/dc/ac converter is given by (2.41)-(2.45). The desired closed-loop magnetic co-energy and electric energy are chosen to be

$$\tilde{W}_m' = \frac{1}{2} L_1 \left(\tilde{i}_{1d}^2 + \tilde{i}_{1q}^2 \right) + \frac{1}{2} L_2 \left(\tilde{i}_{2d}^2 + \tilde{i}_{2q}^2 \right) \tag{4.12}$$

$$\tilde{W}_e = \frac{1}{2} \frac{\tilde{q}_C^2}{C} \tag{4.13}$$

The desired closed-loop dissipation is chosen to be

$$\tilde{\mathcal{R}} = \frac{1}{2} R_1 \left(\tilde{i}_{1d}^2 + \tilde{i}_{1q}^2 \right) + \frac{1}{2} R_2 \left(\tilde{i}_{2d}^2 + \tilde{i}_{2q}^2 \right) + \frac{1}{2} R_C \tilde{i}_R^2 \tag{4.14}$$

Note that R_1 is damping injected to the closed-loop system in order to make the time derivative of the Lyapunov function negative definite, as will be shown by (4.30).

The symbolic vectors $\tilde{\mathbf{I}}$ and $\tilde{\mathbf{Q}}$ for the closed-loop system are defined as

$$\tilde{\mathbf{I}} = \begin{bmatrix} \tilde{i}_{1d} & \tilde{i}_{1q} & \tilde{i}_C & \tilde{i}_R & \tilde{i}_{2d} & \tilde{i}_{2q} \end{bmatrix}^T \tag{4.15}$$

$$\tilde{\mathbf{Q}} = \begin{bmatrix} \tilde{q}_{1d} & \tilde{q}_{1q} & \tilde{q}_C & \tilde{q}_R & \tilde{q}_{2d} & \tilde{q}_{2q} \end{bmatrix}^T \tag{4.16}$$

The constraint matrix $\tilde{\mathbf{G}}$ for the closed-loop system is

$$\tilde{\mathbf{G}} = \begin{bmatrix} -\dfrac{u_{d1}}{2} & -\dfrac{u_{q1}}{2} & 1 & 1 & -\dfrac{u_{d2}}{2} & -\dfrac{u_{q2}}{2} \end{bmatrix} \tag{4.17}$$

The Lagrange multiplier vector $\tilde{\boldsymbol{\Lambda}}$ for the closed-loop system is

$$\tilde{\boldsymbol{\Lambda}} = \begin{bmatrix} \lambda_1 \end{bmatrix} \tag{4.18}$$

As shown by (2.41)-(2.45), the ac/dc/ac converter is an underactuated system with five state variables (i_{1d}, i_{1q}, q_C^D, i_{2d}, and i_{2q}) and four controllable inputs (u_{1d}, u_{1q}, u_{2d}, and u_{2q}). Therefore i_{1d}^D, i_{1q}^D, i_{2d}^D, and i_{2q}^D are chosen to be the four directly controlled desired state variables, meaning that q_C^D will have dynamics. The specified set point equations are

$$i_{1d}^D = i_{1d}^* \tag{4.19}$$

$$i_{1q}^{D} = i_{1q}^{*} \tag{4.20}$$

$$i_{2d}^{D} = i_{2d}^{*} \tag{4.21}$$

$$i_{2q}^{D} = i_{2q}^{*} \tag{4.22}$$

where i_{1d}^{*} , i_{1q}^{*} , i_{2d}^{*} , and i_{2q}^{*} are the controller set points.

Given these specifications by the control designer, the automated method derives the control law. The closed-loop Lagrangian is calculated as

$$\tilde{\mathcal{L}} = \tilde{W}_{m}{}' - \tilde{W}_{e} = \frac{1}{2} L_1 \left(\tilde{i}_{1d}{}^2 + \tilde{i}_{1q}{}^2 \right) + \frac{1}{2} L_2 \left(\tilde{i}_{2d}{}^2 + \tilde{i}_{2q}{}^2 \right) - \frac{1}{2} \frac{\tilde{q}_C{}^2}{C} \tag{4.23}$$

After evaluating (4.2) and (4.3) and re-expressing the error dynamics in standard state space form

$$\frac{d\tilde{i}_{1d}}{dt} = \tilde{i}_{1q} \omega_1 - \frac{R_1}{L_1} \tilde{i}_{1d} - \frac{\tilde{q}_C u_{1d}}{2CL_1} \tag{4.24}$$

$$\frac{d\tilde{i}_{1q}}{dt} = -\tilde{i}_{1d} \omega_1 - \frac{R_1}{L_1} \tilde{i}_{1q} - \frac{\tilde{q}_C u_{1q}}{2CL_1} \tag{4.25}$$

$$\frac{d\tilde{q}_C}{dt} = \frac{\tilde{i}_{1d} u_{1d}}{2} + \frac{\tilde{i}_{1q} u_{1q}}{2} + \frac{\tilde{i}_{2d} u_{2d}}{2} + \frac{\tilde{i}_{2q} u_{2q}}{2} - \frac{\tilde{q}_C}{CR_C} \tag{4.26}$$

$$\frac{d\tilde{i}_{2d}}{dt} = \tilde{i}_{2q} \omega_2 - \frac{R_2}{L_2} \tilde{i}_{2d} - \frac{\tilde{q}_C u_{2d}}{2CL_2} \tag{4.27}$$

$$\frac{d\tilde{i}_{2q}}{dt} = -\tilde{i}_{2d} \omega_2 - \frac{R_2}{L_2} \tilde{i}_{2q} - \frac{\tilde{q}_C u_{2q}}{2CL_2} \tag{4.28}$$

The Lyapunov function and the time derivative of the Lyapunov function are

$$V = \tilde{W}_{m}{}' + \tilde{W}_{e} = \frac{1}{2} L_1 \left(\tilde{i}_{1d}{}^2 + \tilde{i}_{1q}{}^2 \right) + \frac{1}{2} L_2 \left(\tilde{i}_{2d}{}^2 + \tilde{i}_{2q}{}^2 \right) + \frac{1}{2} \frac{\tilde{q}_C{}^2}{C} \tag{4.29}$$

$$\dot{V} = \frac{\partial V}{\partial \tilde{\mathbf{x}}} \frac{d\tilde{\mathbf{x}}}{dt} = -R_1 \left(\tilde{i}_{1d}{}^2 + \tilde{i}_{1q}{}^2 \right) - R_2 \left(\tilde{i}_{2d}{}^2 + \tilde{i}_{2q}{}^2 \right) - \frac{\tilde{q}_C{}^2}{C^2 R_C} \tag{4.30}$$

It is apparent that (4.29) is positive definite and (4.30) is negative definite, so the automated control law derivation is continued. (Without the added damping R_1 in the closed-loop system, (4.30) would only

67

be negative semidefinite, not negative definite.) After applying Steps 5 and 6, (4.24)-(4.28) become in terms of desired values

$$\frac{di_{1d}^D}{dt} = \frac{V_{1d}}{L_1} + i_{1q}^D \omega_1 + \frac{R_1}{L_1}\left(i_{1d} - i_{1d}^D\right) - \frac{q_C^D u_{1d}}{2CL_1} \tag{4.31}$$

$$\frac{di_{1q}^D}{dt} = \frac{V_{1q}}{L_1} - i_{1d}^D \omega_1 + \frac{R_1}{L_1}\left(i_{1q} - i_{1q}^D\right) - \frac{q_C^D u_{1q}}{2CL_1} \tag{4.32}$$

$$\frac{dq_C^D}{dt} = \frac{i_{1d}^D u_{1d}}{2} + \frac{i_{1q}^D u_{1q}}{2} + \frac{i_{2d}^D u_{2d}}{2} + \frac{i_{2q}^D u_{2q}}{2} - \frac{q_C^D}{CR_C} \tag{4.33}$$

$$\frac{di_{2d}^D}{dt} = i_{2q}^D \omega_2 - \frac{R_2}{L_2} i_{2d}^D - \frac{q_C^D u_{2d}}{2CL_2} \tag{4.34}$$

$$\frac{di_{2q}^D}{dt} = -i_{2d}^D \omega_2 - \frac{R_2}{L_2} i_{2q}^D - \frac{q_C^D u_{2q}}{2CL_2} \tag{4.35}$$

Solving (4.31)-(4.35) and the set point equations (4.19)-(4.22) for u_{1d}, u_{1q}, u_{2d}, u_{2q}, $\dfrac{dq_C^D}{dt}$, i_{1d}^D, i_{1q}^D,

i_{2d}^D, and i_{2q}^D, the following control law is obtained.

$$u_{1d} = \frac{2\left(CV_{1d} + CR_1 i_{1d} - CR_1 i_{1d}^* + CL_1 i_{1q}^* \omega_1\right)}{q_C^D} \tag{4.36}$$

$$u_{1q} = \frac{2\left(CV_{1q} + CR_1 i_{1q} - CR_1 i_{1q}^* - CL_1 i_{1d}^* \omega_1\right)}{q_C^D} \tag{4.37}$$

$$u_{2d} = \frac{-2\left(CR_2 i_{2d}^* - CL_2 i_{2q}^* \omega_2\right)}{q_C^D} \tag{4.38}$$

$$u_{2q} = \frac{-2\left(CR_2 i_{2q}^* + CL_2 i_{2d}^* \omega_2\right)}{q_C^D} \tag{4.39}$$

$$\frac{dq_C^D}{dt} = -\frac{\left(q_C^D\right)^2 - C^2 R_C\left(V_{1d}i_{1d}^* + V_{1q}i_{1q}^*\right) + C^2 R_C R_2\left(i_{2d}^{*\,2} + i_{2q}^{*\,2}\right) + C^2 R_C R_1\left(i_{1d}^{*\,2} + i_{1q}^{*\,2} - i_{1d}i_{1d}^* - i_{1q}i_{1q}^*\right)}{CR_C q_C^D} \tag{4.40}$$

68

4.2.1.   Simulation Results

The dynamic equations given by (2.41)-(2.45) and the control equations given by (4.36)-(4.40) are simulated using the MATLAB differential equation solver 'ode45.' The parameters, the set points, and the initial conditions used in the simulation are given in Table 4.1, Table 4.2, and Table 4.3 respectively.

Table 4.1: Parameters for ac/dc/ac converter

Symbol	Quantity	Value
V_0	Magnitude of three-phase voltage source	80 V
ω_1	Frequency of three-phase voltage source	377 rad/sec
C	Capacitance of dc-link capacitor	200 μF
L_1	Inductance on line with voltage source	0.5 mH
L_2	Inductance of three-phase load	5 mH
R_C	Resistance of resistor in parallel with capacitor	25 Ω
R_2	Resistance of three-phase load	0.1 Ω

Table 4.2: Controller set points for ac/dc/ac converter

Symbol	Quantity	Value
R_1	Injected resistance for controller	0.1 Ω
ω_2	Desired frequency of load currents	300 rad/sec
i_{1d}^*	Set point for direct component of source current	10 A
i_{1q}^*	Set point for quadrature component of source current	0 A
i_{2d}^*	Set point for direct component of load current	8 A
i_{2q}^*	Set point for quadrature component of load current	1 A

Table 4.3: Initial conditions for ac/dc/ac converter

Symbol	Quantity	Initial Condition
i_{1d}	Direct component of the source current	11 A
i_{1q}	Quadrature component of source current	-1 A
i_{2d}	Direct component of load current	9 A
i_{2q}	Quadrature component of load current	-1 A
q_C	Charge of dc-link capacitor	0.03 C
q_C^D	Desired charge of dc-link capacitor	0.04 C
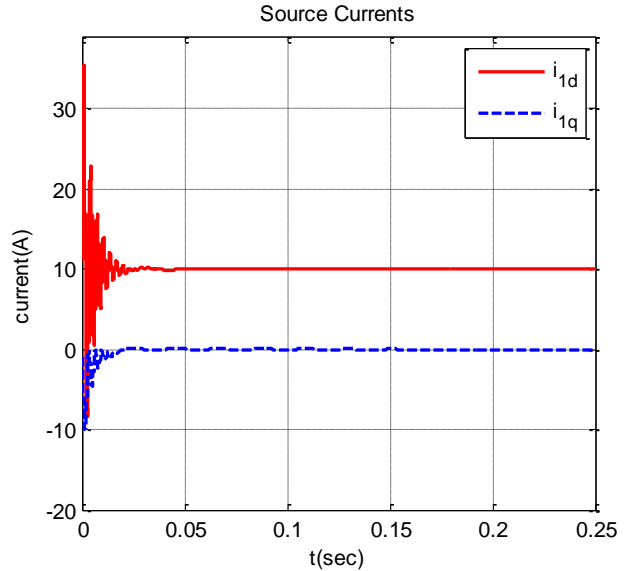
Figure 4.1: Source currents as a function of time for the ac/dc/ac converter using passivity-based control.

The source currents and the load currents as a function of time are shown in Figures 4.1 and 4.2 respectively, and it is evident that these currents converge to their set points. The capacitor charge and

69

the desired capacitor charge as a function of time are plotted in Figure 4.3, demonstrating that the desired capacitor charge reaches a stable equilibrium and the actual capacitor charge converges to the desired charge. Finally, the duty ratios for the two switches are shown in Figures 4.4 and 4.5. As will be shown in Section 4.2.3, these duty ratios are within feasible limits.
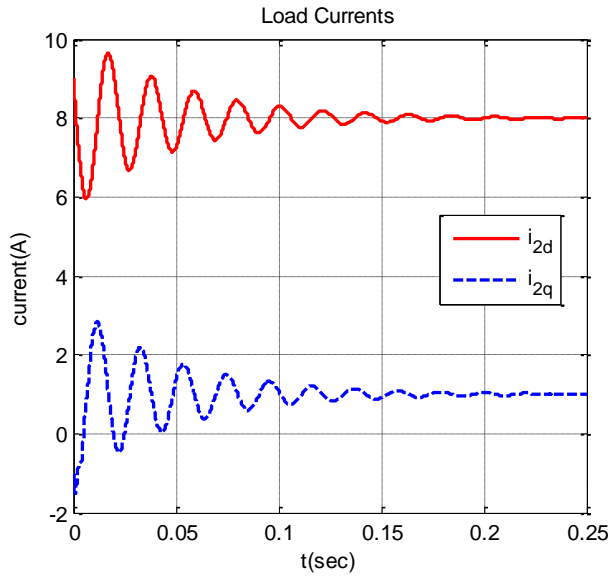
Figure 4.2: Load currents as a function of time for the ac/dc/ac converter using passivity-based control
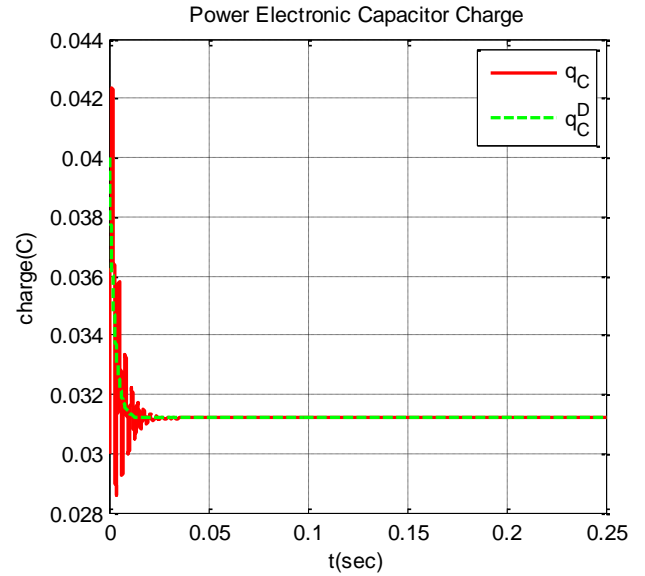
Figure 4.3: Capacitor charge and the desired capacitor charge as a function of time for the ac/dc/ac converter using passivity-based control.

4.2.2. Controller Stability Limits

To ensure internal stability with passivity-based control, it is necessary to check the stability of the zero dynamics of the non-directly controlled desired state variables [14,41]. As tracking of i_{1d}, i_{1q}, i_{2d}, and i_{2q} is achieved ($i_{1d} \to i_{1d}^*$, $i_{1q} \to i_{1q}^*$, $i_{2d} \to i_{2d}^*$, and $i_{2q} \to i_{2q}^*$), the dynamics of q_C^D given by (4.40) become

$$\frac{dq_C^D}{dt} = \frac{C\left(V_{1d}i_{1d}^* + V_{1q}i_{1q}^* - R_2 i_{2d}^{*\,2} - R_2 i_{2q}^{*\,2}\right)}{q_C^D} - \frac{q_C^D}{CR_C} \tag{4.41}$$
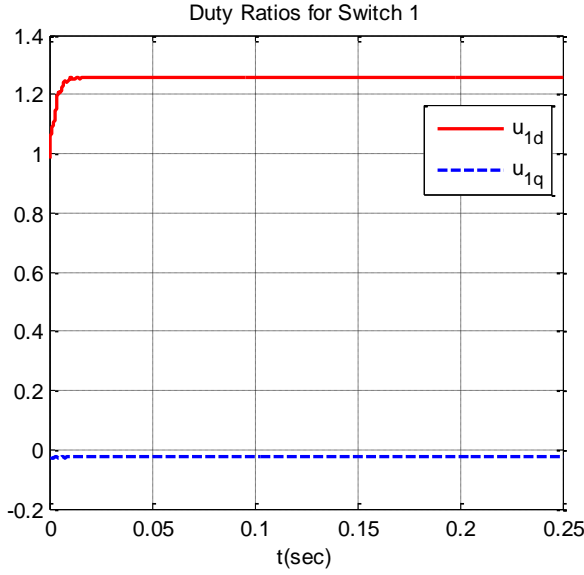
Figure 4.4: Duty ratios of switch 1 as a function of time for the ac/dc/ac converter using passivity-based control
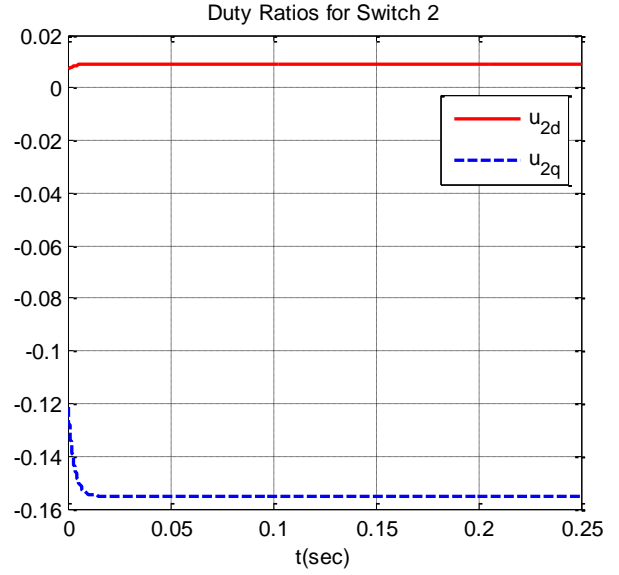
Figure 4.5: Duty ratios of switch 2 as a function of time for the ac/dc/ac converter using passivity-based control.

Examining (4.41), it is apparent that the resistance R_C in parallel with the capacitor is necessary or there would be no possible equilibrium for q_C^D. Figure 4.6 shows a plot of the zero dynamics of q_C^D using the parameters given in the previous section. It is evident that there is a stable equilibrium because the slope at the *x*-intercept in Figure 4.6 (where $dq_C^D/dt = 0$) is negative.
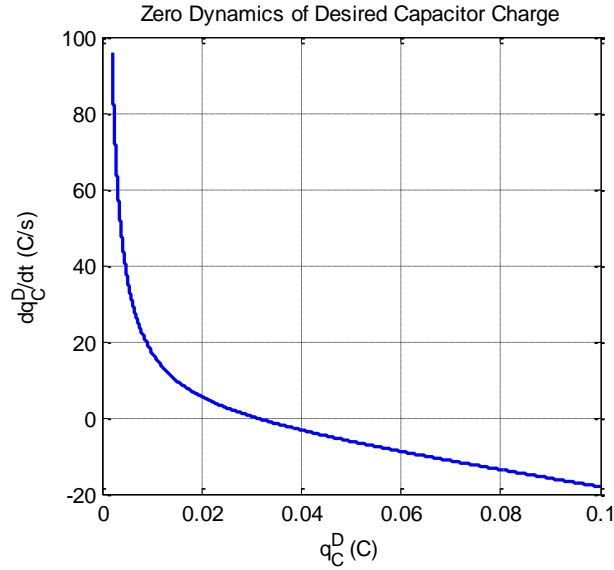
Figure 4.6: Plot of the zero dynamics for the desired capacitor charge showing that there is a stable equilibrium.

71

To calculate the condition for when (4.41) has a stable equilibrium, let $M_2 = -CR_C$ and $M_1 = C\left(V_{1d}i_{1d}^* + V_{1q}i_{1q}^* - R_2 i_{2d}^{*2} - R_2 i_{2q}^{*2}\right)$. The equilibrium solution $\bar{q}_C^D$ to (4.41) is

$$\bar{q}_C^D = \sqrt{-M_1 M_2} \tag{4.42}$$

Since M_2 is always negative, there is only an equilibrium when M_1 is positive. This happens when

$$V_{1d}i_{1d}^* + V_{1q}i_{1q}^* \geq R_2 i_{2d}^{*2} + R_2 i_{2q}^{*2} \tag{4.43}$$

This condition can be interpreted as the set points must be chosen such that the power supplied by the voltage source is greater than the power output supplied to the load.

To check the stability of the equilibrium given by (4.42), (4.41) is linearized around the equilibrium.

$$\frac{dq_C^D}{dt} = \left[\frac{-M_1}{\left(\bar{q}_C^D\right)^2} + \frac{1}{M_2}\right]\left(q_C^D - \bar{q}_C^D\right) \tag{4.44}$$

This linearized differential equation is stable if

$$\frac{-M_1}{\left(\bar{q}_C^D\right)^2} + \frac{1}{M_2} < 0 \tag{4.45}$$

Substituting in the expression for $\bar{q}_C^D$ given by (4.41), it is apparent that condition (4.45) is always satisfied since M_2 is always negative. Therefore, as long as condition (4.43) is met and an equilibrium exists, this equilibrium is always stable.

4.2.3.   Switch Feasibility Limits

Also, in order for the controller to be physically realizable, it is necessary for the switch duty ratios to stay within their feasible limits. For analyzing the feasibility limits of the duty ratios in the dq reference frame, the easiest approach is to use the switching function space vector [60,71]. For the switches on the left side of the ac/dc/ac converter, the switching function space vector is defined as

$$U = \sqrt{\frac{2}{3}}\left(u_{1a} + au_{1b} + a^2 u_{1c}\right) \tag{4.46}$$

where $a = e^{j2\pi/3}$ [60,71] . All eight possible switching vectors are shown in Figure 4.7. There are six non-zero space vector (U_1-U_6) and two zero space vectors (U_7-U_8). When using state-space averaging, the average switching vector must remain within the dotted hexagon shown in Figure 4.7 [60].

Switching State	u_{1a}	u_{1b}	u_{1c}	Switching Vector
U_1	1	-1	-1	$2\sqrt{2/3} + 0j$
U_2	1	1	-1	$0.8165 + 1.4142j$
U_3	-1	1	-1	$-0.8165 + 1.4142j$
U_4	-1	1	1	$-2\sqrt{2/3} + 0j$
U_5	-1	-1	1	$-0.8165 - 1.4142j$
U_6	1	-1	1	$0.8165 - 1.4142j$
U_7	1	1	1	0
U_8	-1	-1	-1	0
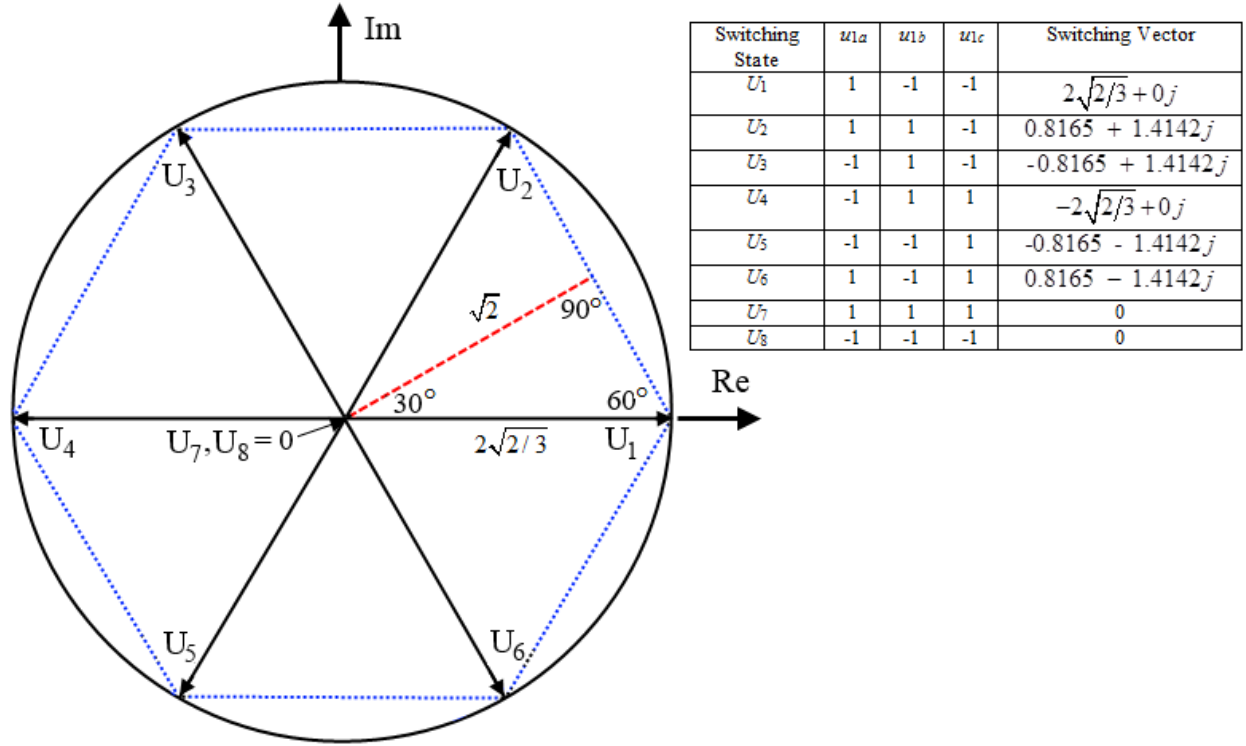
Figure 4.7: Switching function space vectors for ac/dc/ac converter.

Therefore, for sinusoidal steady-state operation, the switching functions u_{1d} and u_{1q} must satisfy

$$\sqrt{u_{1d}^2 + u_{1q}^2} \le \sqrt{2} \qquad (4.47)$$

The feasibility condition for the switches on the right side of the ac/dc/ac converter can be similarly derived to be

$$\sqrt{u_{2d}^2 + u_{2q}^2} \le \sqrt{2} \qquad (4.48)$$

Looking at Figures 4.4 and 4.5, it is evident that conditions (4.47) and (4.48) are met for the example in Section 4.2.1. It is also of interest to calculate the conditions for which the duty ratios are feasible in terms of the parameters and set points of the system. Conditions (4.47) and (4.48) are met when

73

$$\left(V_{1d} + L_1 i_{1q}^* \omega_1\right)^2 + \left(V_{1q} - L_1 i_{1d}^* \omega_1\right)^2 - \frac{\left(\bar{q}_C^D\right)^2}{2C^2} < 0 \tag{4.49}$$

$$\left(L_2 i_{2q}^* \omega_2 - R_2 i_{2d}^*\right)^2 + \left(-L_2 i_{2d}^* \omega_2 - R_2 i_{2q}^*\right)^2 - \frac{\left(\bar{q}_C^D\right)^2}{2C^2} < 0 \tag{4.50}$$

4.3. Summary

A new automated method for deriving the passivity-based control law for electrical systems was introduced in this chapter. Since deriving the passivity-based control law by hand is a complex and lengthy procedure, the automation of this control law derivation is valuable because it allows for quick testing of different closed-loop system behavior and different set point equations. As mentioned in Section 4.1, while the closed-loop energy and dissipation functions should be chosen so that the Lyapunov function is positive definite and the time derivative of the Lyapunov function is negative definite, the choice of these closed-loop functions is not unique. The effect of varying these closed-loop functions and finding optimal closed-loop functions based on the cost of control are open questions for future work.

The automated method was demonstrated on an ac/dc/ac converter in this chapter, and controller stability limits and switch feasibility limits were derived for this example. The next chapter will discuss the design of a variable drive controller for flywheels using time-scale separation and this automated passivity-based control logic.

5. Variable Speed Drive Controller for Flywheels

Building upon the automated passivity-based control law derivation introduced in Chapter 4, this chapter applies passivity-based control to the flywheel variable speed drive, whose dynamic equations were derived in Section 2.2.2. The switch positions of the power electronics are controlled in order to regulate the speed of the flywheel (and hence the energy stored in the flywheel) to a different speed than the grid frequency.

Previous work for machine speed control takes advantage of the natural time-scale separation between the mechanical and electrical variables but assumes that the stator voltages of the machine are directly controllable inputs [43,47]. This technique can be used to design control for stand-alone machines, but cannot be applied for interconnected power systems since the stator voltages are not directly controllable in interconnected systems. Also much previous literature on flywheels neglects the fast dynamics of the power electronics interfacing between the flywheel and the rest of the grid and models the flywheel as an ideal power source or current source [18,19]. However, when using flywheels for transient stabilization on a very fast time-scale, it is necessary to include the fast power electronic dynamics or else potential instabilities on a very fast time-scale will not be captured.

Extending this previous work, a novel passivity-based controller using three time-scale separations is introduced in this chapter for the variable speed drive.   As described in Section 2.2.2, the stator voltages of the flywheel are not assumed to be directly controllable, and the only directly controllable inputs are the switch positions in the power electronics, which allows the controller to be applicable to interconnected power systems. Also, the fast dynamics of the inductors and capacitors in the power electronics are included, as shown in the dynamic model given in Section 2.2.2. Therefore, a third time-scale for the fast power electronic dynamics is added to the time-scale separation between the mechanical and electrical machine variables in [43,47], and therefore a third layer is added to the controller.

This chapter demonstrates the ability of the variable speed drive controller to regulate both the flywheel speed and the power electronic currents to desired set point values. Chapter 6 will then describe

several options for choosing these set point values in order to transiently stabilize power systems against large sudden wind power disturbances using this flywheel variable speed drive controller.

5.1. Time-Scale Separation of the Variable Speed Drive

The automated passivity-based control methodology from Section 4.1 could be generalized from electrical systems to electromechanical systems and then applied to the full dynamic model for the variable speed drive given by (2.116)-(2.124). However, to simplify the control design and reduce the amount of communications needed, the controller takes advantage of the natural time-scale separation between the mechanical machine state variables, the electric machine state variables, and the power electronic state variables.

Three different time-scales for the variable speed drive are defined, as shown in Table 5.1. The slowest time-scale is the mechanical machine time-scale, the middle time-scale is the electrical machine time-scale, and the fastest time-scale is the power electronics time-scale. Each of these time-scales will be used to derive the control law for a layer of the controller described in the next section.

Table 5.1: Time-scale separation of variable speed drive

Time-Scale	Mechanical Machine State Variables (ω_2, θ_2)	Electrical Machine State Variables $(i_{R2}, i_{S2d}, i_{S2q})$	Power Electronics State Variables (i_{1d}, i_{1q}, q_{C1})
Mechanical machine time-scale (Slowest)	Dynamic	Instantaneous	Instantaneous
Electrical machine time-scale (Middle)	Frozen	Dynamic	Instantaneous
Power electronics time-scale (Fastest)	Frozen	Frozen	Dynamic

5.1.1. Mechanical Machine Time-Scale

In the mechanical machine time-scale, the mechanical machine state variables (ω_2, θ_2) have dynamics, and the electrical machine state variables $(i_{R2}, i_{S2d}, i_{S2q})$ and the power electronic state variables (i_{1d}, i_{1q}, q_{C1}) are assumed to be instantaneous because their time constants are much smaller. Therefore, the dynamics in the mechanical machine time-scale are

$$\frac{d\omega_2}{dt} = \frac{\tau_{e2} - \tau_{M2} - B_2\omega_2}{J_2} \tag{5.1}$$

$$\frac{d\theta_2}{dt} = \omega_2 \tag{5.2}$$

In this time-scale, the electric torque τ_{e2}, which is a product of the machine currents, is assumed to be directly controllable, because the electrical machine dynamics are much faster.

5.1.2. Electrical Machine Time-Scale

In the electrical machine time-scale, the electrical machine state variables have dynamics. The mechanical machine state variables are assumed to be frozen because their time constants are much larger while the power electronic state variables are assumed to be instantaneous because their time constants are much smaller. Therefore, the dynamics in the electrical machine time-scale are

$$\frac{d\mathbf{I}_2}{dt} = inv(\mathbf{L}_2)\left(\mathbf{V}_2 - \mathbf{R}_2\mathbf{I}_2 - \mathbf{\Omega}_2\mathbf{L}_2\mathbf{I}_2\right) \tag{5.3}$$

where

$$\mathbf{I}_2 = \begin{bmatrix} i_{S2d} \\ i_{S2q} \\ i_{R2} \end{bmatrix}, \quad \mathbf{V}_2 = \begin{bmatrix} v_{S2d} \\ v_{S2q} \\ v_{R2} \end{bmatrix}, \quad \mathbf{R}_2 = \begin{bmatrix} R_{S2} & 0 & 0 \\ 0 & R_{S2} & 0 \\ 0 & 0 & R_{R2} \end{bmatrix},$$

$$\mathbf{L}_2 = \begin{bmatrix} L_{S2} + L_{SS2} & 0 & \sqrt{\frac{3}{2}}M_2 \\ 0 & L_{S2} + L_{SS2} & 0 \\ \sqrt{\frac{3}{2}}M_2 & 0 & L_{R2} \end{bmatrix}, \quad \mathbf{\Omega}_2 = \begin{bmatrix} 0 & -\omega_2 & 0 \\ \omega_2 & 0 & 0 \\ 0 & 0 & 0 \end{bmatrix} \tag{5.4}$$

In this time-scale, ω_2 is assumed to be frozen because the dynamics of the mechanical machine variables are much slower while the stator voltages v_{S2d} and v_{S2q} are assumed to be directly controllable, because the power electronic dynamics are much faster.

5.1.3. Power Electronics Time-Scale

In the power electronics time-scale, the power electronics state variables have dynamics while the mechanical and electrical machine state variables are assumed to be frozen because their time constants are much larger. Therefore, the dynamics in the power electronics time-scale are

$$\frac{di_{1d}}{dt} = i_{1q}\omega_1 + \frac{V_{1d}}{L_1} - \frac{R_1}{L_1}i_{1d} - \frac{q_{C1}u_{1d}}{2C_1L_1} \tag{5.5}$$

$$\frac{di_{1q}}{dt} = -i_{1d}\omega_1 + \frac{V_{1q}}{L_1} - \frac{R_1}{L_1}i_{1q} - \frac{q_{C1}u_{1q}}{2C_1L_1} \tag{5.6}$$

$$\frac{dq_{C1}}{dt} = \frac{i_{1d}u_{1d}}{2} + \frac{i_{1q}u_{1q}}{2} - \frac{i_{S2d}u_{2d}}{2} - \frac{i_{S2q}u_{2q}}{2} - \frac{q_{C1}}{C_1R_{C1}} \tag{5.7}$$

In this time-scale, i_{S2d} and i_{S2q} are assumed to be frozen because the dynamics of the electrical machine variables are much slower. The controllable inputs are the same as for the full model, the duty ratios of the switches u_{1d}, u_{1q}, u_{2d}, and u_{2q}.

5.2. Three-Layer Control Methodology

The three-layer controller shown in Figure 5.1 was introduced in [17] to regulate both the speed of the flywheel ω_2 and the current into the power electronics, i_{1d} and i_{1q}. The outermost controller is the speed controller, which uses the slowest time-scale model to regulate the speed of the synchronous machine to a set point specified by the control designer. The torque controller then uses the middle time-scale model to control the electric torque to the reference value specified by the speed controller. This control strategy relies on the fact that the torque controller can regulate the electric torque much faster than the reference electric torque changes. The innermost controller is the power electronics controller ,which uses the fastest time-scale model to control the stator voltages to the reference values specified by the torque controller, as well as to control the power electronics currents to set points specified by the control designer. Finally, in order to test the control logic, the switch duty ratios determined by the power electronics controller are fed into the full dynamic model for the variable speed drive given by (2.116)-(2.124).
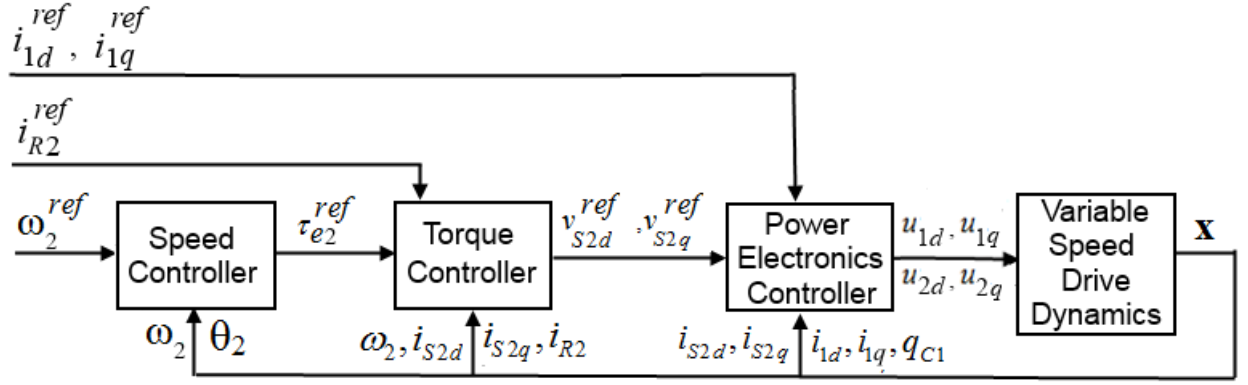
Figure 5.1: Block diagram for the three-layer variable speed drive controller.

5.2.1.   Speed Controller

The speed controller uses the dynamic model in the slowest time-scale, the mechanical machine time-scale, to control the speed of the synchronous machine to a set point ω_2^{ref}. Since the dynamic model in the slowest time-scale is a very simple linear system, a proportional integral controller is used. The control law for the electric torque is given by

$$\tau_{e2}^{ref} = K_P\left(\omega_2^{ref} - \omega_2\right) + K_I \omega_{2Int}$$
$$\dot{\omega}_{2Int} = \omega_2^{ref} - \omega_2$$

(5.8)

where K_P is the proportional gain, and K_I is the integral gain specified by the control designer. The integral gain causes the steady-state error to be zero. The speed controller then gives the value of τ_{e2}^{ref} to the torque controller, which uses τ_{e2}^{ref} as a set point. It should be noted that the gains should not be made too large, or else the time-scale separation of the open-loop dynamics may not hold true for the closed-loop system and hence the reference electric torque may change faster than the torque controller can regulate the electric torque.

5.2.2.   Torque Controller

The torque controller uses the dynamic model in the middle time-scale, the electrical machine time-scale, to control the electric torque to the set point specified by the speed controller, τ_{e2}^{ref}. Passivity-based

79

control logic is used for the torque controller, applying the automated method introduced in Section 4.1. The desired closed-loop magnetic co-energy and electric energy are chosen to be

$$\tilde{W}_m{}' = \frac{1}{2}\left(L_{S2} + L_{SS2}\right)\left(\tilde{i}_{S2d}{}^2 + \tilde{i}_{S2q}{}^2\right) + \frac{1}{2}L_{R2}\tilde{i}_{R2}{}^2 \tag{5.9}$$

$$\tilde{W}_e = 0 \tag{5.10}$$

The desired dissipation function is chosen to be

$$\tilde{\mathcal{R}} = \frac{1}{2}R_{S2}\left(\tilde{i}_{S2d}{}^2 + \tilde{i}_{S2q}{}^2\right) + \frac{1}{2}R_{R2}\tilde{i}_{R2}{}^2 \tag{5.11}$$

The vector of currents $\tilde{\mathbf{I}}$ and the vector of charges $\tilde{\mathbf{Q}}$ for the closed-loop system are defined as

$$\tilde{\mathbf{I}} = \begin{bmatrix} \tilde{i}_{S2d} & \tilde{i}_{S2q} & \tilde{i}_{R2} \end{bmatrix}^T \tag{5.12}$$

$$\tilde{\mathbf{Q}} = \begin{bmatrix} \tilde{q}_{S2d} & \tilde{q}_{S2q} & \tilde{q}_{R2} \end{bmatrix}^T \tag{5.13}$$

The constraint matrix $\tilde{\mathbf{G}}$ and the Lagrange multiplier vector $\tilde{\mathbf{\Lambda}}$ for the closed-loop system are empty matrices since there are no KCL equations.

Since there are two controllable inputs, v_{S2d} and v_{S2q}, in the electrical machine time-scale model, regulation of two reference signals can be achieved. Since the electric torque τ_{e2} is a product of i_{R2} and i_{S2q} as shown by (2.123), i_{R2} and i_{S2q} are chosen to be regulated to set points i_{R2}^{ref} and i_{S2q}^{ref}, which satisfy the reference torque τ_{e2}^{ref} given by the speed controller.

$$i_{R2}^{D} = i_{R2}^{ref} \tag{5.14}$$

$$i_{S2q}^{D} = i_{S2q}^{ref} = \frac{\tau_{e2}^{ref}}{\sqrt{3/2}M_2 i_{R2}^{ref}} \tag{5.15}$$

Since i_{R2}^{D} and i_{S2q}^{D} are chosen to be the directly controlled desired state variables. This means i_{S2d}^{D} will have dynamics [14].

80

Given the state-space model specified by (5.3)-(5.4), the set point equations (5.14)-(5.15), and the desired closed-loop behavior specified by matrices $\tilde{W}_m{}'(\tilde{\mathbf{x}})$, $\tilde{W}_e(\tilde{\mathbf{x}})$, $\tilde{\mathbf{I}}$, $\tilde{\mathbf{Q}}$, $\tilde{\mathbf{G}}$, and $\tilde{\mathbf{\Lambda}}$, the computer derives the control law for the torque controller by taking the following steps:

The desired Lagrangian is calculated as

$$\tilde{\mathcal{L}} = \tilde{W}_m{}' - \tilde{W}_e = \frac{1}{2}\left(L_{S2} + L_{SS2}\right)\left(\tilde{i}_{S2d}{}^2 + \tilde{i}_{S2q}{}^2\right) + \frac{1}{2}L_{R2}\tilde{i}_{R2}{}^2 \tag{5.16}$$

After evaluating (4.2) and (4.3) and re-expressing the error dynamics in standard state space form

$$\frac{d\tilde{i}_{S2d}}{dt} = \tilde{i}_{S2q}\omega_2 - \frac{R_{S2}}{L_{S2} + L_{SS2}}\tilde{i}_{S2d} \tag{5.17}$$

$$\frac{d\tilde{i}_{S2q}}{dt} = -\tilde{i}_{S2d}\omega_2 - \frac{R_{S2}}{L_{S2} + L_{SS2}}\tilde{i}_{S2q} \tag{5.18}$$

$$\frac{d\tilde{i}_{R2}}{dt} = -\frac{R_R}{L_R}\tilde{i}_{R2} \tag{5.19}$$

The Lyapunov function and the time derivative of the Lyapunov function are

$$V = \tilde{W}_m{}' + \tilde{W}_e = \frac{1}{2}\left(L_{S2} + L_{SS2}\right)\left(\tilde{i}_{S2d}{}^2 + \tilde{i}_{S2q}{}^2\right) + \frac{1}{2}L_{R2}\tilde{i}_{R2}{}^2 \tag{5.20}$$

$$\dot{V} = \frac{\partial V}{\partial \tilde{\mathbf{x}}}\frac{d\tilde{\mathbf{x}}}{dt} = -R_{S2}\left(\tilde{i}_{S2d}{}^2 + \tilde{i}_{S2q}{}^2\right) - R_{R2}\tilde{i}_{R2}{}^2 \tag{5.21}$$

It is apparent that the Lyapunov function is positive definite and the time derivative of the Lyapunov function is negative definite. After substituting in $\mathbf{x} - \mathbf{x}^D$ for $\tilde{\mathbf{x}}$ and substituting $\mathbf{f}(x,u)$ in for $\dot{\mathbf{x}}$, (5.17)-(5.19) become in terms of desired values

$$\frac{di_{S2d}^D}{dt} = \frac{2L_{R2}v_{S2d} - \sqrt{6}M\left(v_{R2} - R_{R2}i_{R2}\right) - 2L_{R2}R_{S2}i_{S2d} + i_{S2q}\omega_2}{-3M_2{}^2 + 2L_{R2}L_{S2} + 2L_{R2}L_{SS2}}$$
$$- \omega_2\left(i_{S2q} - i_{S2q}^D\right) + \frac{R_S\left(i_{S2d} - i_{S2d}^D\right)}{L_{S2} + L_{SS2}} \tag{5.22}$$

$$\frac{di_{S2q}^D}{dt} = -i_{S2d}^D\omega_2 - \frac{R_{S2}i_{S2q}^D - v_{S2q} + \sqrt{\frac{3}{2}}M_2 i_{R2}\omega_2}{L_S + L_{SS}} \tag{5.23}$$

$$\frac{di_{R2}^{D}}{dt} = -\frac{2\left(L_{S2}+L_{SS2}\right)\left(R_{R2}i_{R2}-v_{R2}\right)+\sqrt{6}M\left(v_{Sd2}-R_{S2}i_{Sd2}\right)+\sqrt{6}M_{2}\omega_{2}i_{Sq2}\left(L_{S2}+L_{SS2}\right)}{-3M_{2}^{2}+2L_{R2}L_{S2}+2L_{R2}L_{SS2}}$$
$$+\frac{R_{R}\left(i_{R2}-i_{R2}^{D}\right)}{L_{R}} \tag{5.24}$$

Solving (5.22)-(5.24) and the set point equations (5.14)-(5.15) for the two control inputs (v_{S2d} and v_{S2q}), the two directly controlled desired state variables (i_{S2q}^{D} and i_{R2}^{D}), and the derivative of the one non-directly controlled desired state variable ($\frac{di_{S2d}^{D}}{dt}$), the following control law is obtained.

$$v_{S2d}^{ref} = -\frac{\sqrt{6}\left(2\left(L_{SS2}+L_{S2}\right)R_{R2}i_{R2}^{ref}-2\left(L_{SS2}+L_{S2}\right)v_{R2}\right)}{6M_{2}}$$
$$-\frac{\sqrt{6}\left(-\sqrt{6}M_{2}R_{S2}i_{S2d}^{ref}+\sqrt{6}\left(L_{SS2}+L_{S2}\right)M_{2}i_{S2d}\omega_{2}\right)}{6M_{2}}$$
$$-\frac{\sqrt{6}\left(3M_{2}\right)R_{R2}i_{R2}-3M_{2}R_{R2}i_{R2}^{ref}}{6L_{R2}M_{2}} \tag{5.25}$$

$$v_{S2q}^{ref} = \omega_{2}\left(L_{S2}+L_{SS2}\right)i_{S2d}^{D}+\sqrt{3/2}\,\omega_{2}M_{2}i_{R2}+\frac{\sqrt{6}R_{S2}\tau_{e2}^{ref}}{3M_{2}i_{R2}^{ref}} \tag{5.26}$$

$$\frac{di_{S2d}^{D}}{dt} = \frac{\sqrt{6}\left(L_{S2}+L_{SS2}\right)\omega_{2}\tau_{e2}^{ref}-\sqrt{6}\left(L_{S2}+L_{SS2}\right)R_{R2}\left(i_{R2}^{ref}\right)^{2}+\sqrt{6}\left(L_{S2}+L_{SS2}\right)v_{R2}i_{R2}^{ref}}{3M_{2}i_{R2}^{ref}\left(L_{S2}+L_{SS2}\right)}$$
$$-\frac{R_{S2}i_{R2}^{ref}\left(i_{S2d}^{D}-i_{S2d}\right)+\left(L_{S2}+L_{SS2}\right)i_{R2}^{ref}i_{S2q}\omega_{2}}{i_{R2}^{ref}\left(L_{S2}+L_{SS2}\right)} \tag{5.27}$$

As described in the previous chapter, in order to ensure internal stability with passivity-based control, it is necessary to check the stability of the zero dynamics of the desired state variables [14,41]. As tracking of i_{S2d}, i_{S2q}, and i_{R2} is achieved ($i_{S2q}\to i_{S2q}^{ref}, i_{R2}\to i_{R2}^{ref}$, and $i_{S2d}\to i_{S2d}^{D}$), the dynamics of i_{S2d}^{D} given by (5.27) become

$$\frac{di_{S2d}^{D}}{dt} = \frac{\sqrt{6}\left(v_{R2}-R_{R2}i_{R2}^{ref}\right)}{3M_{2}i_{R2}^{ref}} \tag{5.28}$$

Examining (5.28), it is apparent that there is only a stable equilibrium for i^D_{S2d} if and only if

$i^{ref}_{R2} = \dfrac{v_{R2}}{R_{R2}}$. Therefore, i_{R2} cannot actually be controlled to an arbitrary set point, and $i^{ref}_{R2} = \dfrac{v_{R2}}{R_{R2}}$ will be

used for all subsequent simulations in this thesis.

5.2.3. Power Electronics Controller

The power electronics controller uses the dynamic model in the fast time-scale, the power electronics

time-scale to control the stator voltages to the set points specified by the torque controller, v^{ref}_{S2d} and v^{ref}_{S2q}

as well as to regulate the currents to set points specified by the control designer, i^{ref}_{1d} and i^{ref}_{1q}. In order

for the power electronics to achieve regulation of the reference stator voltages, the following algebraic

expressions for the duty ratios of the second switch must be used:

$$u_{2d} = \frac{2C_1 v^{ref}_{S2d}}{q_{C1}} \tag{5.29}$$

$$u_{2q} = \frac{2C_1 v^{ref}_{S2q}}{q_{C1}} \tag{5.30}$$

Substituting in these expressions, the dynamic model in the fast time-scale becomes

$$\frac{di_{1d}}{dt} = i_{1q}\omega_1 + \frac{V_{1d}}{L_1} - \frac{R_1}{L_1}i_{1d} - \frac{q_{C1}u_{1d}}{2C_1L_1} \tag{5.31}$$

$$\frac{di_{1q}}{dt} = -i_{1d}\omega_1 + \frac{V_{1q}}{L_1} - \frac{R_1}{L_1}i_{1q} - \frac{q_{C1}u_{1q}}{2C_1L_1} \tag{5.32}$$

$$\frac{dq_{C1}}{dt} = \frac{i_{1d}u_{1d}}{2} + \frac{i_{1q}u_{1q}}{2} - \frac{C_1\left(i_{S2d}v^{ref}_{S2d} + i_{S2q}v^{ref}_{S2q}\right)}{q_{C1}} - \frac{q_{C1}}{C_1R_{C1}} \tag{5.33}$$

Since the dynamics described by (5.31)-(5.33) are nonlinear, the automated passivity-based control

methodology is again used. The desired closed-loop magnetic co-energy and electric energy are chosen

to be

$$\tilde{W}_m' = \frac{1}{2}L_1\left(\tilde{i}_{1d}^{\,2} + \tilde{i}_{1q}^{\,2}\right) \tag{5.34}$$

$$\tilde{W}_e = \frac{1}{2}\frac{\tilde{q}_{C1}^2}{C_1} \tag{5.35}$$

The desired closed-loop dissipation is chosen to be

$$\tilde{\mathcal{R}} = \frac{1}{2}R_1\left(\tilde{i}_{1d}^2 + \tilde{i}_{1q}^2\right) + \frac{1}{2}R_{C1}\tilde{i}_{R1}^2 \tag{5.36}$$

The symbolic vectors $\tilde{\mathbf{I}}$ and $\tilde{\mathbf{Q}}$ for the closed-loop system are defined as

$$\tilde{\mathbf{I}} = \begin{bmatrix}\tilde{i}_{1d} & \tilde{i}_{1q} & \tilde{i}_{C1} & \tilde{i}_{R1}\end{bmatrix}^T \tag{5.37}$$

$$\tilde{\mathbf{Q}} = \begin{bmatrix}\tilde{q}_{1d} & \tilde{q}_{1q} & \tilde{q}_{C1} & \tilde{q}_{R1}\end{bmatrix}^T \tag{5.38}$$

The constraint matrix $\tilde{\mathbf{G}}$ for the closed-loop system is

$$\tilde{\mathbf{G}} = \begin{bmatrix}-\dfrac{u_{1d}}{2} & -\dfrac{u_{1q}}{2} & 1 & 1\end{bmatrix} \tag{5.39}$$

The Lagrange multiplier vector $\tilde{\mathbf{\Lambda}}$ for the closed-loop system is

$$\tilde{\mathbf{\Lambda}} = \begin{bmatrix}\lambda_1\end{bmatrix} \tag{5.40}$$

Since there are two remaining controllable inputs in (5.31)-(5.33), i_{1d}^D and i_{1q}^D are chosen to be the directly controlled desired state variables. This means q_{C1}^D will have dynamics. The set point equations are given by

$$i_{1d}^D = i_{1d}^{ref} \tag{5.41}$$

$$i_{1q}^D = i_{1q}^{ref} \tag{5.42}$$

Given these specifications by the control designer, the automated method derives the control law for the power electronics controller. The closed-loop Lagrangian is calculated as

$$\tilde{\mathcal{L}} = \tilde{W}_m{}' - \tilde{W}_e = \frac{1}{2}L_1\left(\tilde{i}_{1d}^2 + \tilde{i}_{1q}^2\right) - \frac{1}{2}\frac{\tilde{q}_{C1}^2}{C_1} \tag{5.43}$$

After evaluating (4.2) and (4.3) and re-expressing the error dynamics in standard state space form

$$\frac{d\tilde{i}_{1d}}{dt} = \tilde{i}_{1q}\omega_1 - \frac{R_1}{L_1}\tilde{i}_{1d} - \frac{\tilde{q}_{C1}u_{1d}}{2C_1L_1} \tag{5.44}$$

$$\frac{d\tilde{i}_{1q}}{dt} = -\tilde{i}_{1d}\omega_1 - \frac{R_1}{L_1}\tilde{i}_{1q} - \frac{\tilde{q}_{C1}u_{1q}}{2C_1L_1} \tag{5.45}$$

$$\frac{d\tilde{q}_{C1}}{dt} = \frac{\tilde{i}_{1d}u_{1d}}{2} + \frac{\tilde{i}_{1q}u_{1q}}{2} - \frac{\tilde{q}_{C1}}{C_1R_{C1}} \tag{5.46}$$

The Lyapunov function and the time derivative of the Lyapunov function are

$$V = \tilde{W}_m{}' + \tilde{W}_e = \frac{1}{2}L_1\left(\tilde{i}_{1d}{}^2 + \tilde{i}_{1q}{}^2\right) + \frac{1}{2}\frac{\tilde{q}_{C1}{}^2}{C_1} \tag{5.47}$$

$$\dot{V} = \frac{\partial V}{\partial \tilde{\mathbf{x}}}\frac{d\tilde{\mathbf{x}}}{dt} = -R_1\left(\tilde{i}_{1d}{}^2 + \tilde{i}_{1q}{}^2\right) - \frac{\tilde{q}_{C1}{}^2}{C_1{}^2R_{C1}} \tag{5.48}$$

It is apparent that (5.47) is positive definite and (5.48) is negative definite. After substituting in $\mathbf{x} - \mathbf{x}^D$ for $\tilde{\mathbf{x}}$ and substituting $\mathbf{f}(x,u)$ in for $\dot{\mathbf{x}}$, (5.44)-(5.46) become in terms of desired values

$$\frac{di_{1d}^D}{dt} = \frac{V_{1d}}{L_1} + i_{1q}^D\omega_1 - \frac{R_1}{L_1}i_{1d}^D - \frac{q_{C1}^Du_{1d}}{2C_1L_1} \tag{5.49}$$

$$\frac{di_{1q}^D}{dt} = \frac{V_{1q}}{L_1} - i_{1d}^D\omega_1 - \frac{R_1}{L_1}i_{1q}^D - \frac{q_{C1}^Du_{1q}}{2C_1L_1} \tag{5.50}$$

$$\frac{dq_{C1}^D}{dt} = \frac{i_{1d}^Du_{1d}}{2} + \frac{i_{1q}^Du_{1q}}{2} - \frac{q_{C1}^D}{C_1R_{C1}} - \frac{C_1\left(i_{S2d}v_{S2d}^{ref} + i_{S2q}v_{S2q}^{ref}\right)}{q_{C1}} \tag{5.51}$$

Solving (5.49)-(5.51) and (5.41)-(5.42) for u_{1d}, u_{1q}, $\frac{dq_{C1}^D}{dt}$, i_{1d}^D, and i_{1q}^D the following control law is

obtained.

$$u_{1d} = \frac{2\left(C_1V_{1d} - C_1R_1i_{1d}^{ref} + C_1L_1i_{1q}^{ref}\omega_1\right)}{q_{C1}^D} \tag{5.52}$$

$$u_{1q} = \frac{2\left(C_1V_{1q} - C_1R_1i_{1q}^{ref} - C_1L_1i_{1d}^{ref}\omega_1\right)}{q_{C1}^D} \tag{5.53}$$

$$\frac{dq_{C1}^D}{dt} = \frac{-q_{C1}\left(q_{C1}^D\right)^2 + C_1^2 R_{C1}\left[-\left(v_{S2d}^{ref}i_{S2d} + v_{S2q}^{ref}i_{S2q}\right)q_{C1}^D\right]}{C_1 R_{C1}q_{C1}q_{C1}^D}$$
$$+ \frac{C_1^2 R_{C1}\left[\left(V_{1d}i_{1d}^{ref} + V_{1q}i_{1q}^{ref} - R_1\left(i_{1d}^{ref}\right)^2 - R_1\left(i_{1q}^{ref}\right)^2\right)q_{C1}\right]}{C_1 R_{C1}q_{C1}q_{C1}^D} \tag{5.54}$$

Checking the zero dynamics of q_{C1}^D, as $i_{1d} \to i_{1d}^{ref}, i_{1q} \to i_{1q}^{ref}$, and $q_{C1} \to q_{C1}^D$, the dynamics of q_{C1}^D

given by (5.54) become

$$\frac{dq_{C1}^D}{dt} = \frac{C_1\left(V_{1d}i_{1d}^{ref} + V_{1q}i_{1q}^{ref} - R_1\left(i_{1d}^{ref}\right)^2 - R_1\left(i_{1q}^{ref}\right)^2 - v_{S2d}^{ref}i_{2d} - v_{S2q}^{ref}i_{2q}\right)}{q_{C1}^D} - \frac{q_{C1}^D}{CR_C} \tag{5.55}$$

Examining (5.55), there is only a stable equilibrium for q_{C1}^D when the numerator of the first term is

positive. This happens when

$$V_{1d}i_{1d}^{ref} + V_{1q}i_{1q}^{ref} - R_1\left(i_{1d}^{ref}\right)^2 - R_1\left(i_{1q}^{ref}\right)^2 \geq v_{S2d}^{ref}i_{2d} + v_{S2q}^{ref}i_{2q} \tag{5.56}$$

This condition can be interpreted as the power input to the power electronics after the resistor R_1 must

be greater than the power output of the power electronics. Additionally, as was derived in Section 4.2.3,

in order for the control logic to be physically realizable, the switch duty ratios u_{1d}, u_{1q}, u_{2d}, and u_{2q}

must satisfy (4.47) and (4.48).

5.3. Simulation Results

This variable speed drive is simulated using the full dynamic model given in Section 2.2.2 by (2.116)-

(2.124) and the control equations given by (5.8), (5.25)-(5.27), (5.29)-(5.30), and (5.52)-(5.54). The

parameters used in the simulation are given in Tables 5.2 and 5.3 while the controller set points and gains

are given in Table 5.4. In this section, the set points are just chosen arbitrarily in order to demonstrate the

effectiveness of the variable speed drive controller. In Chapter 6, it will be explored how set points

should be chosen in order to use this controller for transient stabilization of interconnected power

systems.

Table 5.2: Power electronics parameters

Symbol	Quantity	Value
V_0	Magnitude of three-phase voltage source	10 V
ω_1	Frequency of three-phase voltage source	377 rad/sec
C_1	Capacitance of dc-link capacitor	10 mF
L_1	Inductance on line with voltage source	0.5 μH
R_1	Resistance on line with voltage source	0.1 mΩ
R_{C1}	Resistance of resistor in parallel with capacitor	25 Ω

Table 5.3: Flywheel parameters

Symbol	Quantity	Value
L_{R2}	Self-inductance of the rotor winding	5 μH
L_{S2}	Self-inductance of the stator windings	5 μH
L_{SS2}	Mutual inductance between the stator windings	1 μH
M_2	Mutual inductance between the stator and rotor windings when parallel	4 μH
R_{R2}	Resistance of the rotor winding	2×10^{-2} Ω
R_{S2}	Resistance of the stator windings	1×10^{-3} Ω
V_{R2}	Voltage applied to the rotor winding	1 V
J_2	Inertia of the rotor	5×10^{-4} kg m^2
B_2	Damping coefficient of the rotor	2×10^{-4} N m s
τ_{M2}	Mechanical torque applied to the rotor	0 N m

Table 5.4: Variable speed drive set points and gains

Symbol	Quantity	Value
ω_2^{ref}	Set point for the speed of the flywheel	750 rad/sec for t < 0.5 sec 760 rad/sec for t > 1 sec
i_{R2}^{ref}	Set point for the direct component of the stator current of the synchronous machine	50 A
i_{1d}^{ref}	Set point for direct component of source current	100 A for t < 0.5 sec 130 A for t > 0.5 sec
i_{1q}^{ref}	Set point for quadrature component of source current	50 A for t < 0.5 sec 40 A for t > 0.5 sec
K_P	Proportional gain in the speed controller	0.05
K_I	Integral gain in the speed controller	1

The angular speed of the flywheel as a function of time is shown in Figure 5.2, demonstrating that the speed converges to its set point, which changes from 750 rad/sec to 760 rad/sec at 0.5 seconds. The synchronous machine currents and the desired direct stator current as a function of time are shown in Figure 5.3. It is apparent that the desired quadrature stator current reaches a stable equilibrium and the actual quadrature stator current converges to the desired current.
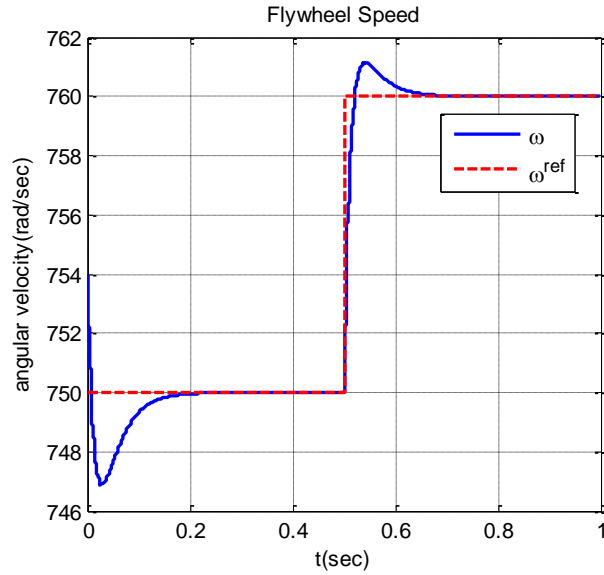
Figure 5.2: Flywheel speed as a function of time for the variable speed drive controller.
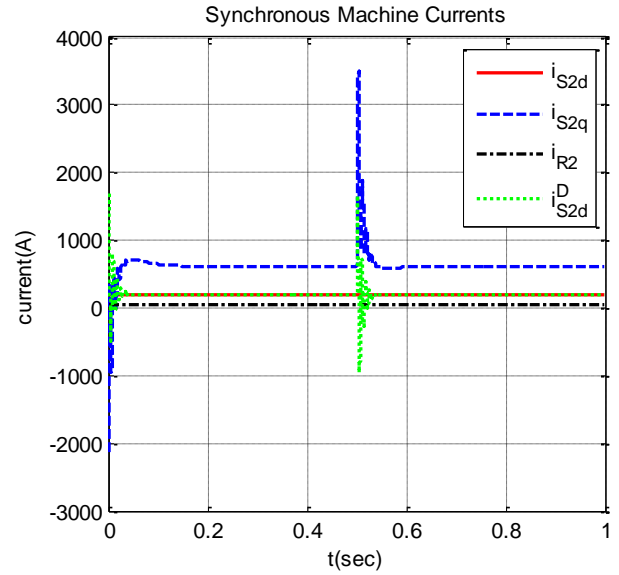
Figure 5.3: Synchronous machine currents and the desired quadrature stator current as a function of time for the variable speed drive controller.

Figure 5.4 shows the power electronic currents as a function of time, and it is evident that they converge to their set points, which also change after 0.5 seconds. The capacitor charge and the desired capacitor charge as a function of time are plotted in Figure 5.5, demonstrating that the desired capacitor charge reaches a stable equilibrium and the actual capacitor charge converges to the desired charge. The duty ratios for the two switches are shown in Figure 5.6, and it is evident that these duty ratios are within the feasible limits given by (4.47) and (4.48).

Finally, Figure 5.7 shows the input and output power of the power electronics. It is observed that in steady-state, the power input after the resistor R_1 is greater than the power output of the power electronics (the power delivered to the flywheel) for both the set points before 0.5 seconds and the set points after 0.5 seconds. Hence stability of q_{C1}^D is achieved as described in Section 5.2.3. It should be noted that for these set points, the majority of the power input to the power electronics is dissipated rather than supplied to the flywheel. In Chapter 6, it will be described how the flywheel speed set point should be chosen so that the majority of the power input to the power electronics is supplied to the flywheel rather than dissipated.

88
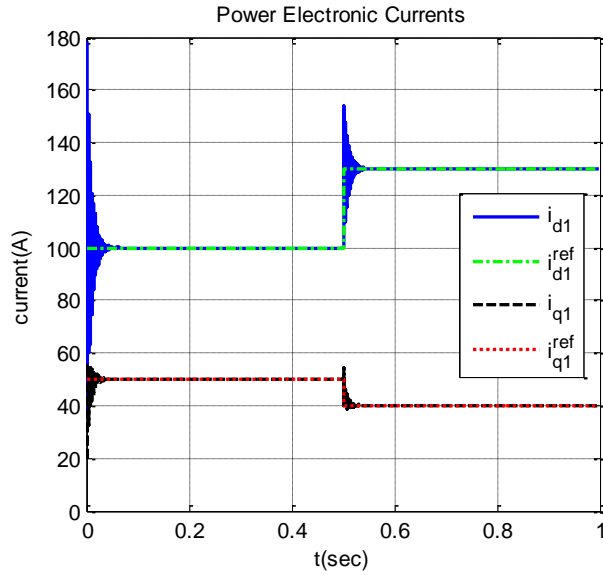
Figure 5.4: Power electronic currents as a function of time for the variable speed drive controller.
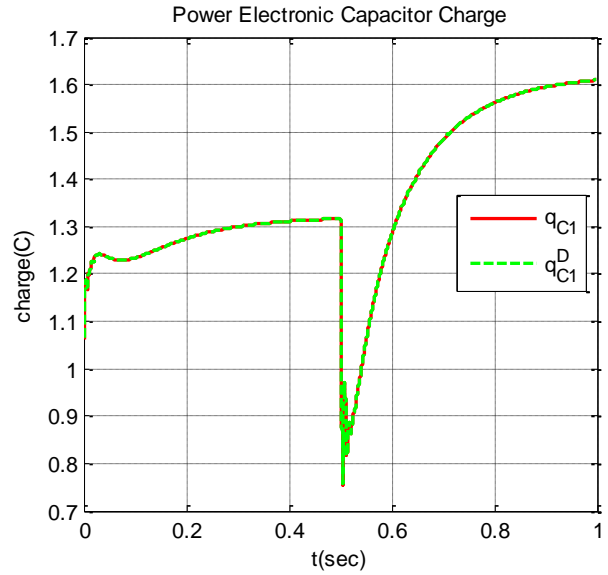
Figure 5.5: Power electronic capacitor charge and the desired capacitor charge as a function of time for the variable speed drive controller.
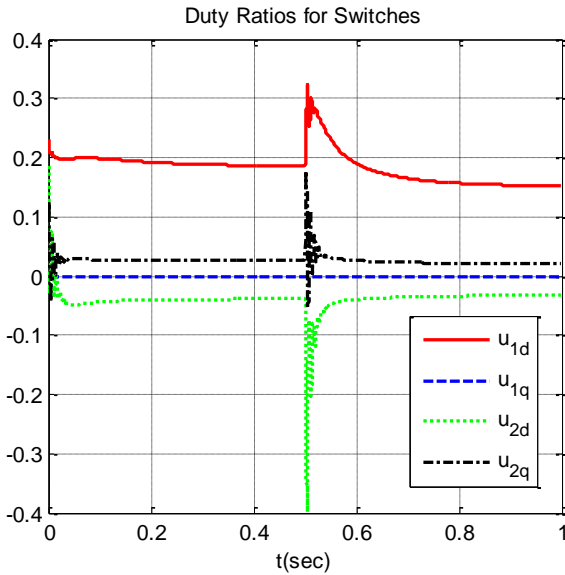
Figure 5.6: Duty ratios of the two switches as a function of time for the variable speed drive controller.
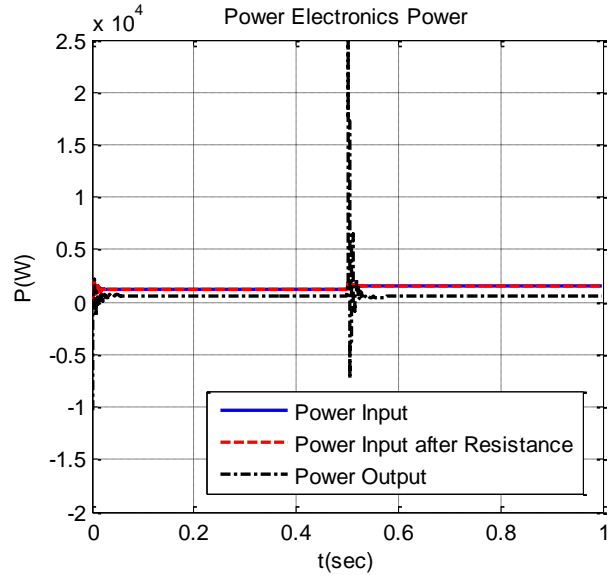
Figure 5.7: Input and output power of the power electronics as a function of time for the variable speed drive controller.

5.4. Summary

A novel variable speed drive controller for flywheels was developed in this chapter using time-scale separation and passivity-based control logic.   A nested three-layer controller was designed, which regulates both the flywheel speed and the power electronic currents to desired set points.   The next

89

chapter will analyze how to choose these set points in order to use the flywheel controller for transient stabilization of power systems in response to wind power disturbances.

While the fast dynamics of the inductors and capacitors were considered in this chapter, the switches were assumed to be ideal. Further research could involve analyzing the effect of switching losses and delays on the control. Designing alternate variable speed drive topologies requiring less infrastructure while maintaining stability is another open question for future work. For example, it would be interesting to examine if the power electronic ac/dc/ac converter could be redesigned as an ac/ac converter without needing the dc-link capacitor.

6. Transient Stabilization Using Flywheels

In this chapter, it is explored how the variable speed drive controller described in the previous chapter can be used to transiently stabilize interconnected power systems against large sudden wind power disturbances. This is the first time passivity-based control has been applied for transient stabilization of power systems using flywheels.

Flywheels are placed at each bus with one or more wind generators, which are the potential disturbance locations. It is desired to choose set points for the variable speed drive controller such that the flywheel absorbs the wind power disturbance and the rest of the system is minimally affected. Three different methods for choosing the set points are described in this chapter and each method is demonstrated and compared on a simple two-bus system. The control will then be demonstrated for larger systems with multiple flywheels and multiple wind generators in Chapter 8.

It should be noted that while the control logic in Chapter 5 was derived for the variable speed drive connected to an infinite bus, the control logic is also applicable for interconnected system for two reasons. First, the dynamics of the transmission line voltages connected to the power electronics evolve at a much slower time-scale than the power electronics. Hence, when designing fast control at the power electronics time-scale, the transmission line voltages can be assumed to be frozen using time-scale separation. Second, the set point logic for the power electronic currents regulates the transmission line voltages to their pre-disturbance values.

6.1. Power Electronic Current Set Points

Three different methods are described in this section for choosing the power electronic current set points for the variable speed drive controller described in Chapter 5.

6.1.1. Constant Current Source Method

The first method explored is to choose the power electronic current set points such that, in closed-loop, the aggregate of the power electronics and all the wind generators on the bus behaves as a constant current source. The set point power electronic currents are

$$i_{1d}^{ref} = i_{Totd}^{ref} - \sum i_{Wd} \tag{6.1}$$

$$i_{1q}^{ref} = i_{Totq}^{ref} - \sum i_{Wq} \tag{6.2}$$

where i_{Totd}^{ref} and i_{Totq}^{ref} are the direct and quadrature components of the constant current source. $\sum i_{Wd}$ is

the sum of the direct components of the stator currents for all wind generators at the bus and $\sum i_{Wq}$ is the

sum of quadrature components of the stator currents for all wind generators at the bus.

6.1.2.   Instantaneous Load Method

The second method considered is to choose the power electronic current set points such that, in

closed-loop, the aggregate of the power electronics and all the wind generators on the bus behaves as an

instantaneous load with an effective resistance R_{eff} and an effective inductance L_{eff}. An instantaneous load

means that the dynamics of the load can be neglected since they are much faster than the rest of the

system. Using this method, the set point power electronic currents are

$$i_{1d}^{ref} = i_{Totd}^{ref} - \sum i_{Wd} \tag{6.3}$$

$$i_{1q}^{ref} = i_{Totq}^{ref} - \sum i_{Wq} \tag{6.4}$$

where

$$i_{Totd}^{ref} = \frac{R_{eff} v_{TLd} + L_{eff} \Omega v_{TLq}}{L_{eff}^{2} \Omega^{2} + R_{eff}^{2}} \tag{6.5}$$

$$i_{Totq}^{ref} = \frac{R_{eff} v_{TLq} - L_{eff} \Omega v_{TLd}}{L_{eff}^{2} \Omega^{2} + R_{eff}^{2}} \tag{6.6}$$

where v_{TLd} and v_{TLq} are the direct and quadrature components of the transmission line capacitor voltage

adjacent to the power electronics. The expressions for i_{Totd}^{ref} and i_{Totq}^{ref} are derived from taking the dynamic

equations for the load given in Section 3.1.4 and setting the time derivatives equal to zero since the

dynamics are instantaneous.

Compared to the constant current source method, the advantage of the instantaneous load method is that the effective resistance R_{eff} in closed-loop at Bus 2 provides additional stability for the closed-loop interconnected system. The disadvantage is that this control method requires slightly more communication than the constant current source method because the adjacent voltages of the transmission line shunt capacitor must now be communicated to the controller.

6.1.3. Passivity-Based Control Method

The third method explored is to choose the power electronic current set points in order to achieve passivity-based control of the adjacent transmission line capacitor voltages. Assume that the right side of the transmission line is adjacent to the power electronics. (If the left side is adjacent instead, an analogous procedure can be used.) The dynamic equations, given in Section 3.1.3, for the capacitor charges on the right side, are

$$\frac{dq_{TLRd}}{dt} = \Omega q_{TLRq} + i_{InTLRd} + i_{TLMd} \tag{6.7}$$

$$\frac{dq_{TLRq}}{dt} = -\Omega q_{TLRd} + i_{InTLRq} + i_{TLMq} \tag{6.8}$$

Since the power electronic dynamics are much faster than the rest of the grid, the port input currents i_{InTLRd} and i_{InTLRq} can be treated as directly controllable at the time-scale in which the dynamics of the rest of the grid evolves. To obtain the reference values for i_{InTLRd} and i_{InTLRq}, the automated passivity-based control described in Section 4.1 is again used. The desired closed-loop magnetic co-energy and electric energy are chosen to be

$$\tilde{W}_m{}' = 0 \tag{6.9}$$

$$\tilde{W}_e = \frac{1}{2} \frac{\tilde{q}_{TLRd}{}^2}{C_{TL}} + \frac{1}{2} \frac{\tilde{q}_{TLRq}{}^2}{C_{TL}} \tag{6.10}$$

The desired closed-loop dissipation is chosen to be

$$\tilde{\mathcal{R}} = \frac{1}{2} R_a \tilde{i}_{TLRd}{}^2 + \frac{1}{2} R_a \tilde{i}_{TLRq}{}^2 \tag{6.11}$$

Note that R_a is damping injected to the closed-loop system in order to make the time derivative of the Lyapunov function negative definite, as will be shown by (6.20).

The symbolic vectors $\tilde{\mathbf{I}}$ and $\tilde{\mathbf{Q}}$ for the closed-loop system are defined as

$$\tilde{\mathbf{I}} = \begin{bmatrix} \tilde{i}_{TLRd} & \tilde{i}_{TLRq} \end{bmatrix}^T \tag{6.12}$$

$$\tilde{\mathbf{Q}} = \begin{bmatrix} \tilde{q}_{TLRd} & \tilde{q}_{TLRq} \end{bmatrix}^T \tag{6.13}$$

The constraint matrix $\tilde{\mathbf{G}}$ and the Lagrange multiplier vector $\tilde{\mathbf{\Lambda}}$ for the closed-loop system are empty matrices since there are no KCL equations.

The specified set point equations are

$$q_{TLRd}^{D} = C_{TL} v_{TLRd}^{ref} \tag{6.14}$$

$$q_{TLRq}^{D} = C_{TL} v_{TLRq}^{ref} \tag{6.15}$$

Given these specifications by the control designer, the automated method derives the control law. The closed-loop Lagrangian is calculated as

$$\tilde{\mathcal{L}} = \tilde{W}_m{}' - \tilde{W}_e = -\frac{1}{2}\frac{\tilde{q}_{TLRd}{}^2}{C_{TL}} - \frac{1}{2}\frac{\tilde{q}_{TLRq}{}^2}{C_{TL}} \tag{6.16}$$

After evaluating (4.2) and (4.3) and re-expressing the error dynamics in standard state space form

$$\frac{d\tilde{q}_{TLRd}}{dt} = \Omega\tilde{q}_{TLRq} - \frac{\tilde{q}_{TLRd}}{C_{TL}R_a} \tag{6.17}$$

$$\frac{d\tilde{q}_{TLRq}}{dt} = -\Omega\tilde{q}_{TLRd} - \frac{\tilde{q}_{TLRq}}{C_{TL}R_a} \tag{6.18}$$

The Lyapunov function and the time derivative of the Lyapunov function are

$$V = \tilde{W}_m{}' + \tilde{W}_e = \frac{1}{2}\frac{\tilde{q}_{TLRd}{}^2}{C_{TL}} + \frac{1}{2}\frac{\tilde{q}_{TLRq}{}^2}{C_{TL}} \tag{6.19}$$

$$\dot{V} = \frac{\partial V}{\partial \tilde{\mathbf{x}}}\frac{d\tilde{\mathbf{x}}}{dt} = -\frac{\tilde{q}_{TLRd}{}^2}{C_{TL}{}^2 R_a} - \frac{\tilde{q}_{TLRq}{}^2}{C_{TL}{}^2 R_a} \tag{6.20}$$

It is apparent that (6.19) is positive definite and (6.20) is negative definite. In terms of desired values, (6.17) and (6.18) become

$$\frac{dq_{TLRd}^{D}}{dt} = i_{InTLRd} + i_{TLMd} + \Omega q_{TLRq}^{D} + \frac{q_{TLRd} - q_{TLRd}^{D}}{C_{TL}R_{a}} \tag{6.21}$$

$$\frac{dq_{TLRq}^{D}}{dt} = i_{InTLRq} + i_{TLMq} - \Omega q_{TLRd}^{D} + \frac{q_{TLRq} - q_{TLRq}^{D}}{C_{TL}R_{a}} \tag{6.22}$$

Solving (6.21)-(6.22) and the set point equations (6.14)-(6.15) for i_{InTLRd}, i_{InTLRq}, q_{TLRd}^{D}, and q_{TLRq}^{D}, the following control law is obtained.

$$i_{InTLRd}^{ref} = \frac{C_{TL}v_{TLRd}^{ref} - q_{TLRd}}{C_{TL}R_{a}} - i_{TLMd} - \Omega C_{TL}v_{TLRq}^{ref} \tag{6.23}$$

$$i_{InTLRq}^{ref} = \frac{C_{TL}v_{TLRq}^{ref} - q_{TLRq}}{C_{TL}R_{a}} - i_{TLMq} + \Omega C_{TL}v_{TLRd}^{ref} \tag{6.24}$$

The set point power electronic currents must then be chosen so that the references for the total current into the transmission line are satisfied.

$$i_{1d}^{ref} = -i_{InTLRd}^{ref} - \sum i_{d} \tag{6.25}$$

$$i_{1q}^{ref} = -i_{InTLRq}^{ref} - \sum i_{q} \tag{6.26}$$

where $\sum i_{d}$ is the sum of the direct components of the currents for all components at the bus besides the transmission line and the power electronics and $\sum i_{q}$ is the sum of quadrature components of the currents for all components at the bus besides the transmission line and the power electronics. Adding the controller for the transmission line voltages to the variable speed drive controller given in Chapter 5, the block diagram shown in Figure 6.1 is obtained.
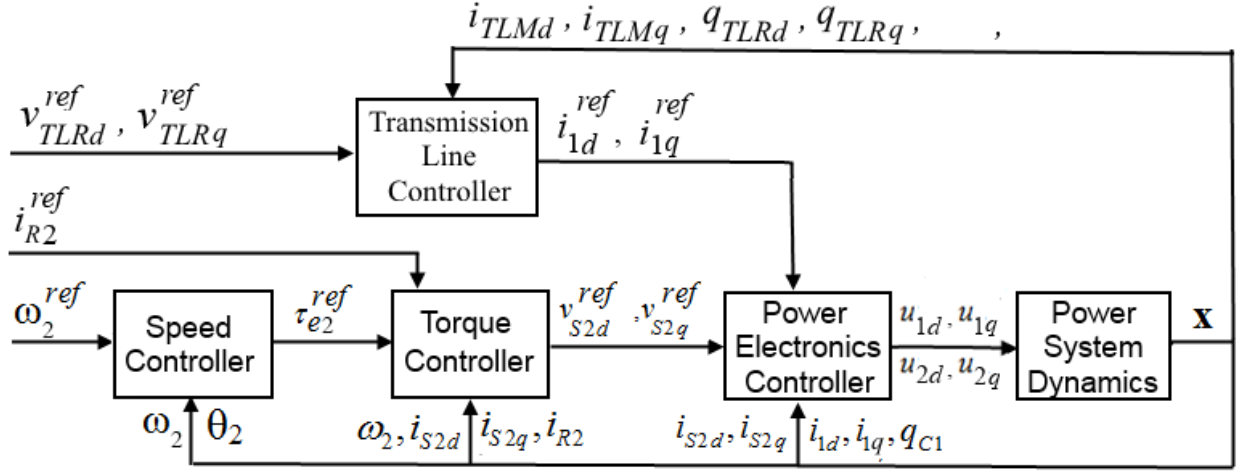
Figure 6.1: Block diagram for the transmission line passivity-based controller combined with the variable speed drive controller.

While this method is able to regulate the transmission line voltages, the disadvantage is that more communication is needed than with the constant current source method or the instantaneous load method. However, it should be noted that communication is still only needed between neighboring components.

6.2. Flywheel Speed Set Point

The flywheel speed set point should be chosen so that most of the power entering the power electronics is absorbed by the flywheel, rather than stored in the dc-capacitor and dissipated by the resistor is parallel with the capacitor. When connected to the shunt capacitor of a transmission line, the stability condition of the power electronics controller derived in Section 5.2.3 becomes

$$v_{TLd}i_{1d}^{ref} + v_{TLq}i_{1q}^{ref} - R_1\left(i_{1d}^{ref}\right)^2 - R_1\left(i_{1q}^{ref}\right)^2 \geq v_{S2d}^{ref}i_{2d} + v_{S2q}^{ref}i_{2q} \tag{6.27}$$

where v_{TLd} and v_{TLq} are the direct and quadrature components of the transmission line capacitor voltage adjacent to the power electronics. Based on conservation of energy in steady-state, (6.27) can be re-written as

$$v_{TLd}i_{1d}^{ref} + v_{TLq}i_{1q}^{ref} - R_1\left(i_{1d}^{ref}\right)^2 - R_1\left(i_{1q}^{ref}\right)^2 \geq R_{R2}i_{R2}^2 + R_{S2}\left(i_{S2d}^2 + i_{S2q}^2\right) + B_2\omega_2^2 - v_{R2}i_{R2} \tag{6.28}$$

The following steady-state values are observed for the flywheel:

$$\omega_2 = \omega_2^{ref} \tag{6.29}$$

96

$$i_{R2} = \frac{v_{R2}}{R_{R2}} \tag{6.30}$$

$$i_{S2q} = \frac{B_2 \omega_2^{ref} v_{R2}}{\sqrt{3/2} M_2 R_{R2}} \tag{6.31}$$

$$i_{S2d} = i_{S2d\_0} \tag{6.32}$$

The steady-state value for i_{S2d} is the initial condition i_{S2d_0} because as shown in Figure 5.2, i_{Sd2} has no closed-loop dynamics. Substituting (6.29)-(6.32) into (6.28), the following restraint is obtained for ω_2^{ref}.

$$\omega_2^{ref} \leq \omega_2^{ref\,max} = \frac{\sqrt{3} M_2 v_{R2} \sqrt{v_{TLd} i_{1d}^{ref} + v_{TLq} i_{1q}^{ref} - R_{S2} i_{S2d\_0}^{\,2} - R_1 \left(i_{1d}^{ref}\right)^2 - R_1 \left(i_{1q}^{ref}\right)^2}}{\sqrt{B_2} \sqrt{3M_2^{\,2} v_{R2}^{\,2} + 2B_2 R_{S2} R_{R2}^{\,2}}} \tag{6.33}$$

One possible approach would be to set ω_2^{ref} to a large percentage of $\omega_2^{ref\,max}$, such as $\omega_2^{ref} = \rho \omega_2^{ref\,max}$ where ρ is a constant close to one. However, the problem with this approach is that ω_2^{ref} would then change very fast since $\omega_2^{ref\,max}$ is an algebraic function of i_{1d}^{ref} and i_{1q}^{ref}, which can change very fast in response to a sudden disturbance. As described in Chapter 6, the variable speed drive controller relies on the fact that the inner torque controller can regulate the electric torque much faster than the outer speed controller changes the reference electric torque τ_{e2}^{ref}. If ω_2^{ref} is changing very fast, then τ_{e2}^{ref} will also change very fast, and the torque controller will not be able to regulate the electric torque faster than the reference torque changes.

To solve this problem, ω_2^{ref} is made a state variable with dynamics

$$\frac{d\omega_2^{ref}}{dt} = -K_S \left(\omega_2^{ref} - \rho \omega_2^{ref\,max}\right) \tag{6.34}$$

A positive gain K_S ensures ω_2^{ref} converges to $\rho\omega_2^{ref\,max}$ in steady-state. However, since ω_2^{ref} has dynamics, it does not change nearly as fast as $\omega_2^{ref\,max}$. Hence, the time-scale separation in the variable speed drive controller still applies.

In addition to the flywheel speed limit from the power electronics controller stability limit, there is also a maximum speed resulting from the tensile strength of the flywheel material [7]. A typical value for the maximum flywheel speed is 36,000 rpm (3770 rad/sec) [72].

6.3. Two-Bus Example Simulation Results

The three methods for choosing the power electronic set points described in Section 6.1, along with the method for choosing the flywheel speed set point described in Section 6.2, are demonstrated on the two-bus system shown in Figure 6.2.
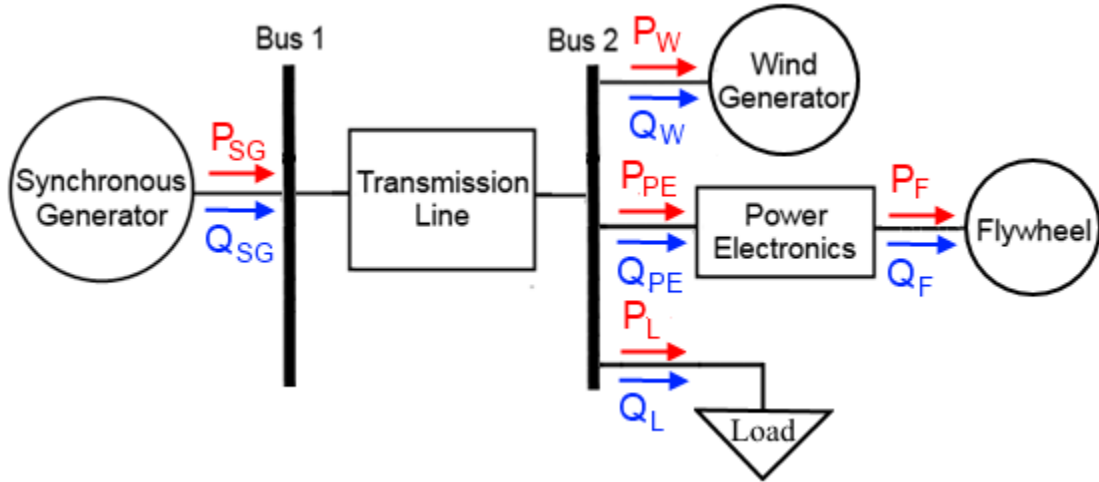

Figure 6.2: Two-bus system on which the flywheel control is demonstrated

The parameters used in the simulations are given in Appendix A. The synchronous machine on Bus 1 has governor and exciter control, as described in Section 3.1.5., in order to regulate the frequency of the system to 60 Hz. The wind generator on Bus 2 is modeled as an induction machine, as described in Section 3.1.2, and there is a sudden prolonged disturbance in the mechanical torque applied to the rotor of the wind generator, as shown by Figure 6.3.
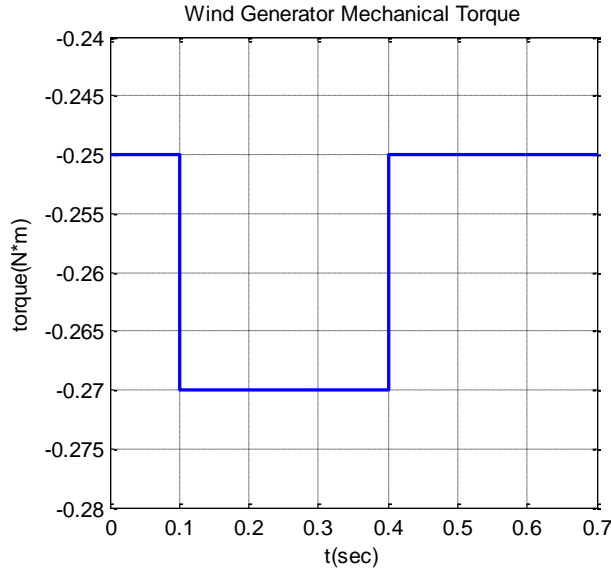
Figure 6.3: Mechanical torque disturbance applied to the wind generator.
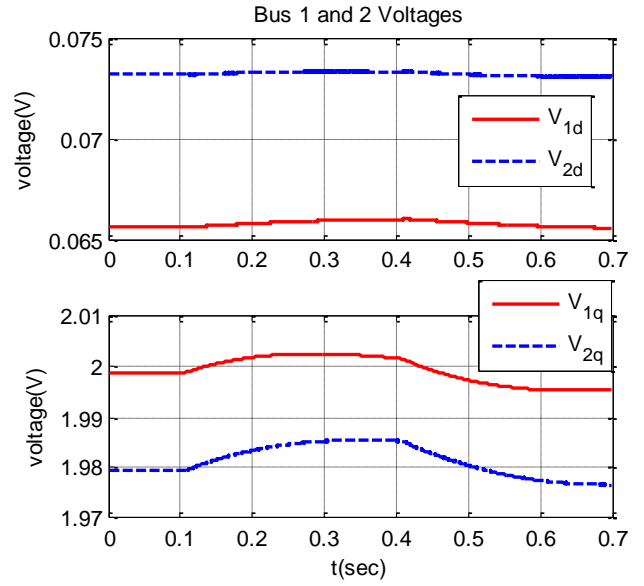
Figure 6.4: Bus 1 and Bus 2 voltages without controller.

Figure 6.4 shows the voltages at Bus 1 and Bus 2 when there is no control (constant values are used for the power electronic duty ratios). High voltage deviations occur due to the disturbance, and the voltages take a few seconds to return to their pre-disturbance values once the disturbance ends. The simulations for each of the three set points methods start in steady-state prior to the disturbance shown in Figure 6.3, although it should be noted that the steady-state values are different depending on which control method is used.

6.3.1.   Constant Current Source Method Set Points

First, simulation results are shown using the constant current source method described in Section 6.1.1. The constant current source values used are $i_{Totd}^{ref} = 1$ and $i_{Totq}^{ref} = 20$. As shown by Figure 6.5, the flywheel reference speed ω_2^{ref} increases during the disturbance since the absolute of the mechanical torque increases and there is more power coming out of the wind generator during the disturbance. As discussed in Section 6.2, ω_2^{ref} changes much slower than $\omega_2^{ref\,max}$ so that the time-scale separation in the variable speed drive controller still applies.
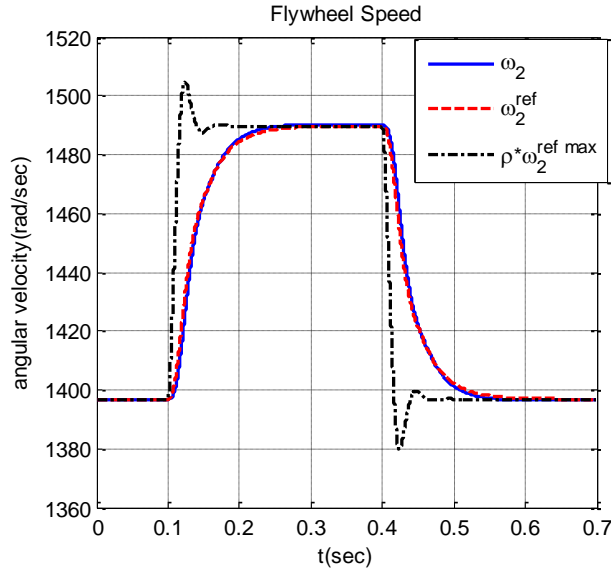
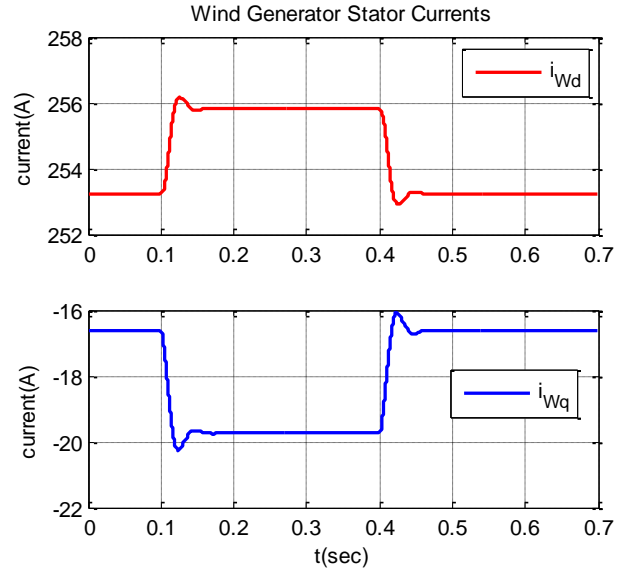**Figure 6.5:** Flywheel speed as a function of time using the constant current source method set points.

Figure 6.6: Wind generator stator currents as a function of time using the constant current source method set points.

Figure 6.6 shows the wind generator stator currents, which, as expected, settle to different values after the disturbance in the mechanical torque applied to the wind generator. Figure 6.7 shows the sum of the power electronic currents and the wind generator stator currents, as well as the reference total currents, demonstrating that with the control logic, the power electronics and the wind generator together behave very nearly as a constant current source. The reason there are small deviations from the constant current reference is that the power electronic dynamics, while very fast, are not instantaneous.

The duty ratios of the two switches are shown in Figure 6.8, and it is evident that they are within the feasible limits given by (4.47) and (4.48). Figure 6.9 and Figure 6.10 show the Bus 1 and Bus 2 voltages with and without the control, demonstrating that, due to the controller, the effect of the disturbance on the rest of the system is very minimal and lasts only a very short time. The oscillations are much smaller with the control than without the control, and also the voltages quickly return to their pre-disturbance values (even though the disturbance is still ongoing) with the control, unlike without the control.
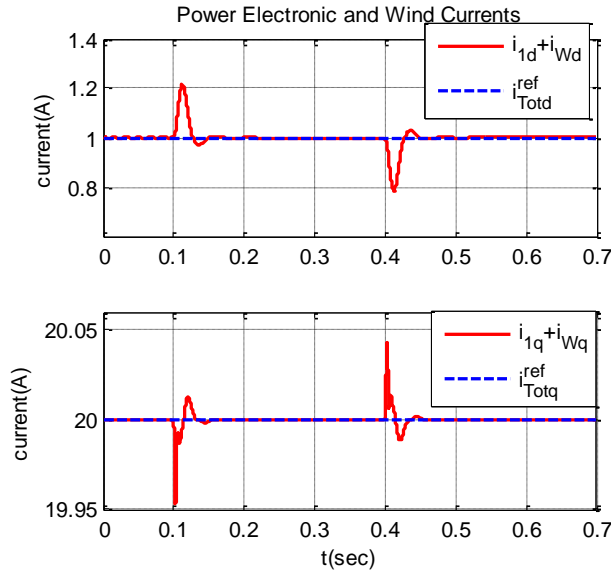
Figure 6.7: Sum of the power electronic currents and the wind generator stator currents, compared to the reference total currents, as a function of time using the constant current source method set points.
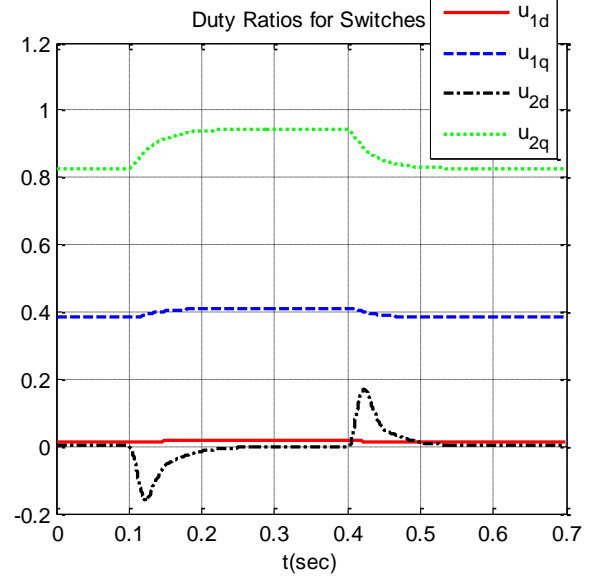
Figure 6.8: Duty ratios of the two switches as a function of time using the constant current source method set points.

Figure 6.9: Bus 1 voltages as a function of time using the constant current source method set points compared to without using any control.
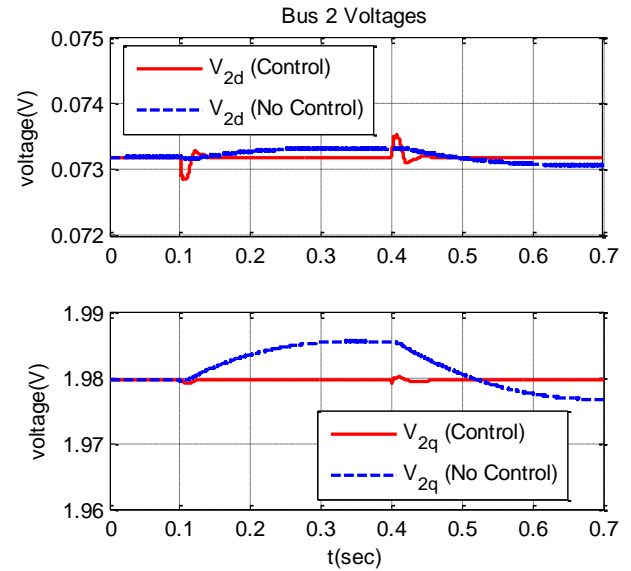
Figure 6.10: Bus 2 voltages as a function of time using the constant current source method set points compared to without using any control.

Finally, the real and reactive power flows, whose directions are defined in Figure 6.2, are shown as a function of time in Figure 6.11 and Figure 6.12. While real and reactive power is conventionally a steady-state concept, the real and reactive power can be calculated from the direct and quadrature

components of the voltages and currents using the instantaneous *p-q* theory [73]. The real and reactive power into an object are

$$P = v_d i_d + v_q i_q \tag{6.35}$$

$$Q = v_q i_d - v_d i_q \tag{6.36}$$

where v_d and v_d are the direct and quadrature components of the bus connected to the object, and i_d and i_q are the direct and quadrature components of the currents into the object.

As shown by Figure 6.11, the real power out of the wind generator increases as a result of the disturbance, which causes the real power into the power electronics and the real power into the flywheel to also increase. Due to the control, which isolates the effect of the disturbance, the real power produced by the synchronous generator and the real power consumed by the load remain almost completely constant.

Several observations for the reactive power flow shown in Figure 6.12 should be noted. Due to the large capacitor on the dc-link of the power electronics, the reactive power into the power electronics is negative (the power electronics actually supplies reactive power to the grid) in steady-state. The reactive power out of the wind generator is also negative in steady-state because an induction machine, even when operating as a generator, always consumes reactive power [74]. During the disturbance, the reactive power consumed by the wind generator increases, which causes the reactive power supplied by the power electronics to increase as well. Due to the control, which isolates the effect of the disturbance, the reactive power out of the synchronous generator and the reactive power consumed by the load remain almost completely constant.

Figure 6.11: Real power flow as a function of time using the constant current source method set points.

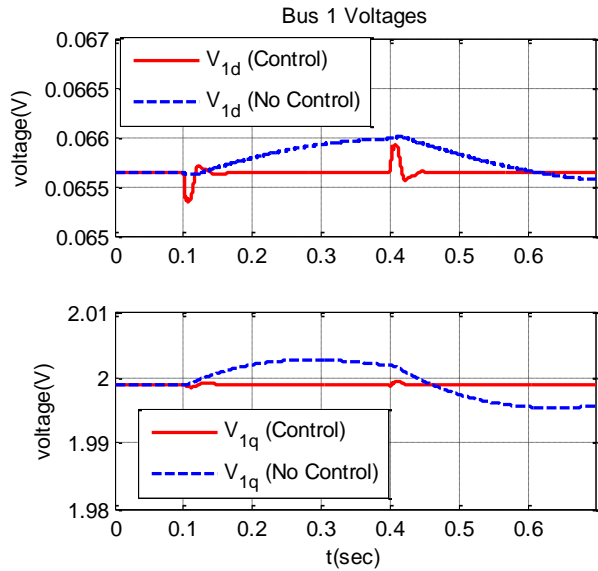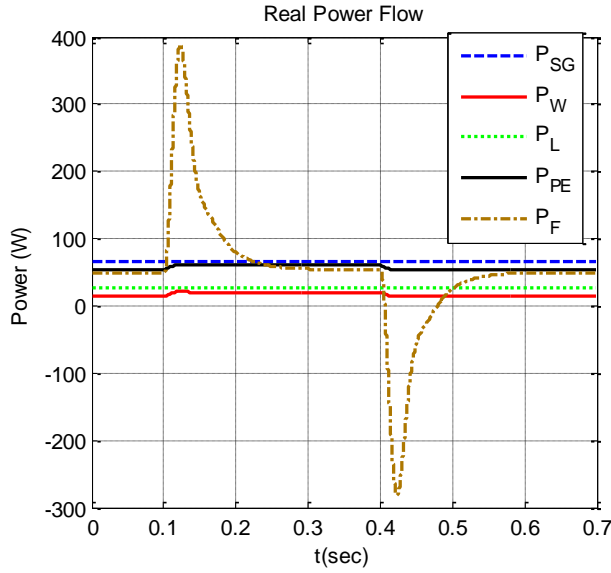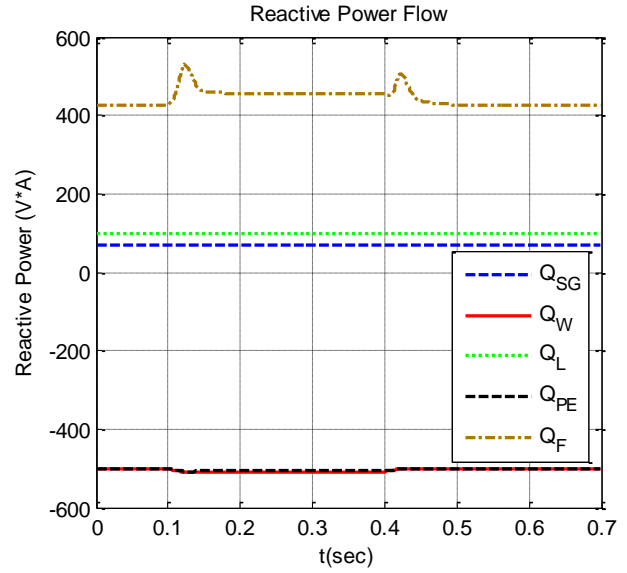**Figure 6.12:** Reactive power flow as a function of time using the constant current source method set points.

6.3.2.　　　Instantaneous Load Method Set Points

Now, it is examined how transient stabilization of the power grid against the wind disturbance can be achieved using instantaneous load method described in Section 6.1.2. The effective resistance and inductance of the load used are $R_{eff} = 0.1 \; \Omega$ and $L_{eff} = 10^{-6} \; H$.

As shown by Figure 6.13, the flywheel speed converges well to the reference speed ω_2^{ref} , which again increases after the disturbance. Figure 6.14 shows the sum of the power electronic currents and the wind generator stator currents, as well as the reference total currents. In contrast to the constant current source method analyzed in the previous section, the reference total current no longer is a constant. Figure 6.15 and Figure 6.16 show the Bus 1 and Bus 2 voltages with and without the control, demonstrating that, due to the controller, the effect of the disturbance on the rest of the system is very minimal and lasts only a very short time. The oscillations are much smaller with the control than without the control, and also the voltages quickly return to their pre-disturbance values with the control, unlike without the control.

Figure 6.13: Flywheel speed as a function of time using the instantaneous load method set points.
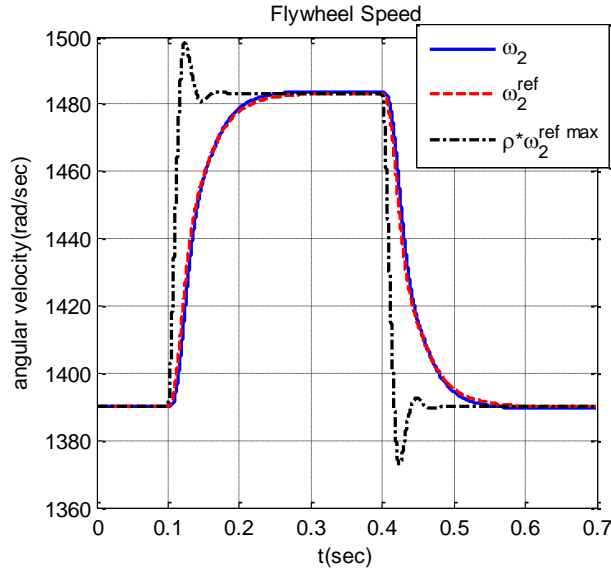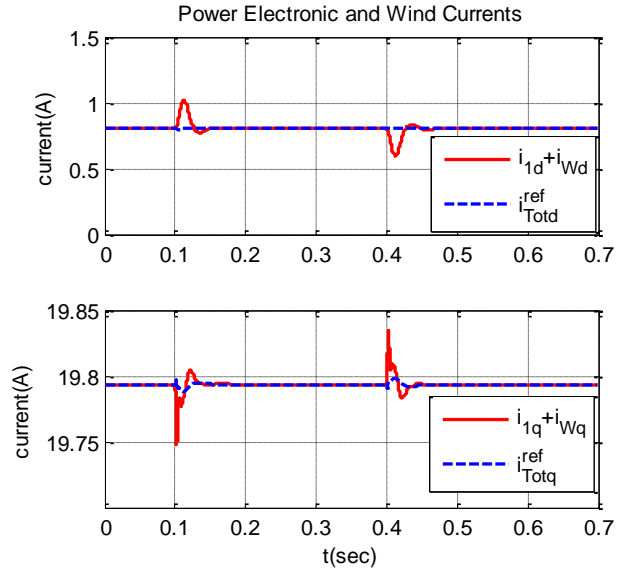
Figure 6.14: Sum of the power electronic currents and the wind generator stator currents, compared to the reference total currents, as a function of time using the instantaneous load method set points.

6.3.3. Passivity-Based Control Method Set Points

Finally, it is examined how transient stabilization of the power grid against the wind disturbance can be achieved using passivity-based control method described in Section 6.1.3. The set points used for the transmission line voltages on Bus 2 are given by $v_{TLRd}^{ref} = 0.073\ V$ and $v_{TLRq}^{ref} = 1.98\ V$. The damping injected to the closed-loop system is $R_a = 0.01\ \Omega$.

As shown by Figure 6.17, the flywheel speed converges well to the reference speed ω_2^{ref}, which again increases after the disturbance. Figure 6.18 shows the total current out of Bus 2 (the sum of the power electronics current, the wind generator current, and the load current), compared to the reference total current. In contrast to the constant current source method, the reference total current is no longer a constant. Figure 6.19 and Figure 6.20 show the Bus 1 and Bus 2 voltages with and without the control. There are larger oscillations immediately following the disturbance with the control than without the control, but the voltages do quickly return to their pre-disturbance values with the control, unlike without the control. While the passivity-based control method, unlike constant current source method or the

104

instantaneous load method, is able to regulate the transmission line voltages to set points, it is evident that there are higher oscillations resulting from the disturbance when using the passivity-based control method than when using the constant current source method or the instantaneous load method.

Figure 6.15: Bus 1 voltages as a function of time using the instantaneous load method set points compared to without using any control.
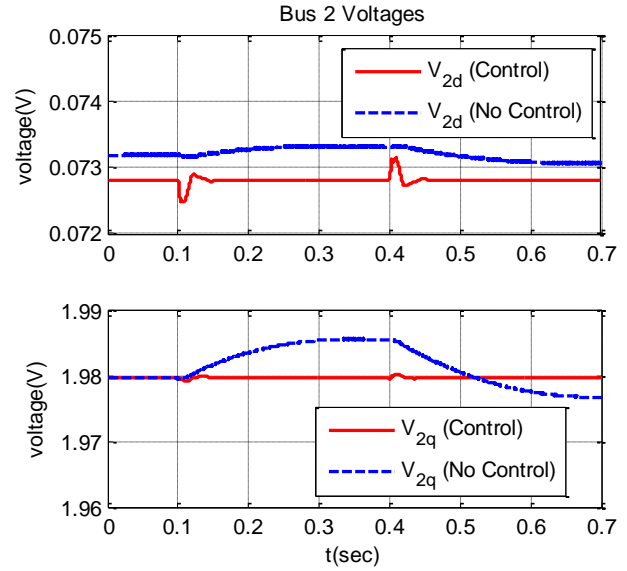
Figure 6.16: Bus 2 voltages as a function of time using the instantaneous load method set points compared to without using any control.
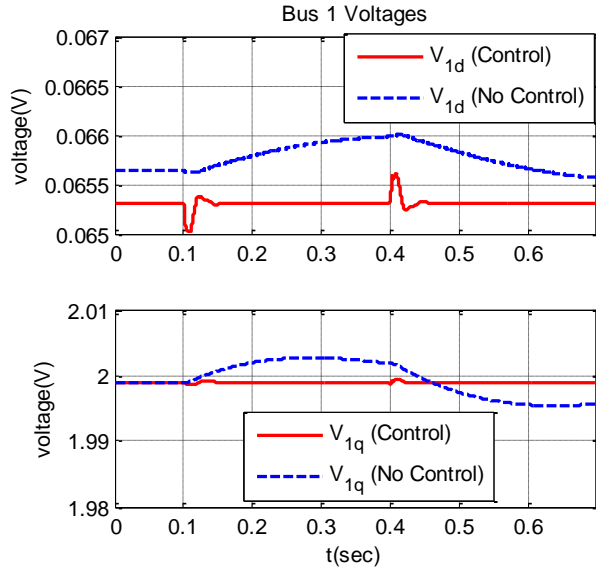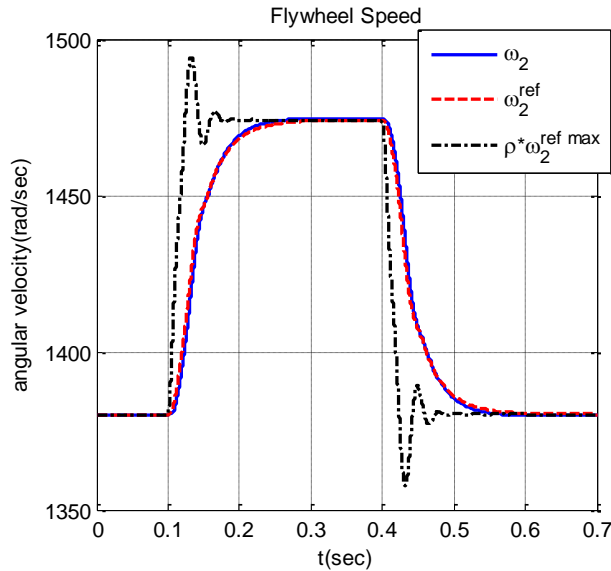

Figure 6.17: Flywheel speed as a function of time using the passivity-based control method set points.
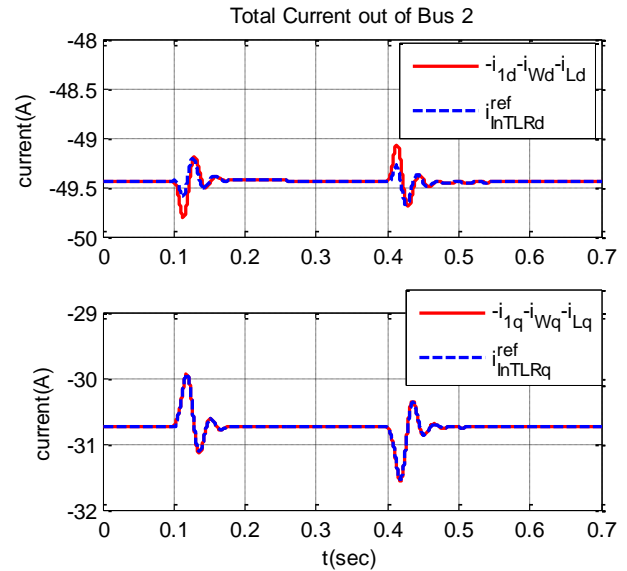
Figure 6.18: Total current out of Bus 2, compared to the reference total current, as a function of time using the passivity-based control method set points.
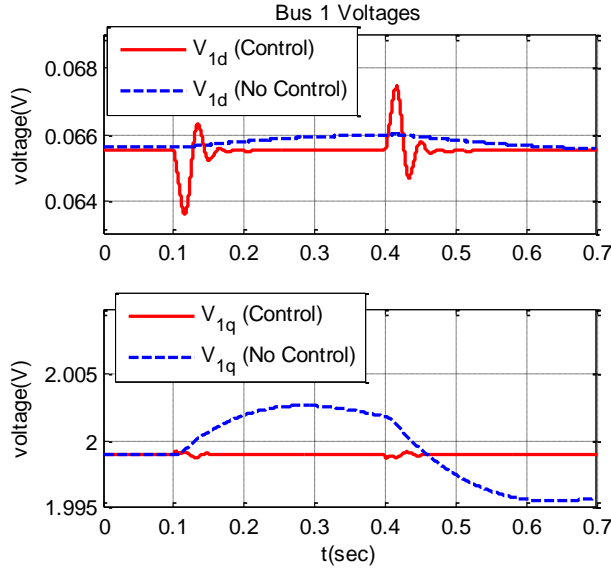
Figure 6.19: Bus 1 voltages as a function of time using the passivity-based control method set points compared to without using any control.
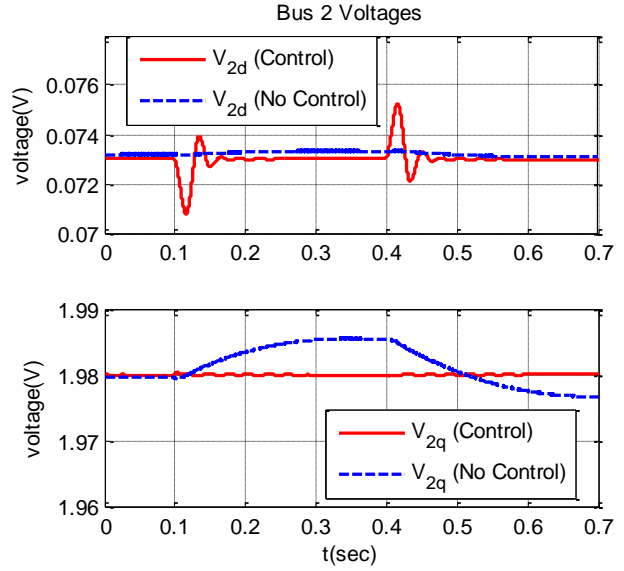
Figure 6.20: Bus 2 voltages as a function of time using the passivity-based control method set points compared to without using any control.

6.4. Summary

This chapter explored using flywheels for transient stabilization of interconnected power systems in response to large sudden wind power disturbances. Three different methods were described for choosing the set points for the flywheel variable speed drive controller so that the flywheel absorbs the wind power disturbance and the rest of the system is minimally affected. Simulation results were shown demonstrating the effectiveness of this controller for a simple two-bus system. The next chapter will discuss sizing the power electronics in the variable speed drive controller, and then this controller will be demonstrated for larger systems in Chapter 8. Further research could involve developing additional methods for choosing the controller set points.

7. Choosing Power Electronic Sizes

This chapter analyzes how changing the size of the power electronic inductors, capacitors, and resistors affects the performance of the flywheel variable speed driver controller for transient stabilization. The effect of changing the parameters is examined for the simulations in Section 6.3.1 using the constant current source set point method, and recommendations are made for sizing these components.

7.1. Power Electronics Inductor

The inductance L_1 should be made as small as possible, in order to make the power electronic dynamics fast and to minimize the effect of the disturbance on the rest of the grid. For the simulation in Section 6.3.1, if L_1 is increased from 0.01 µH to 0.1 µH, then i_{1d} and i_{1q} do not converge to their set points as quickly, and as a result, there is more of an effect from the disturbance on the rest of the system, as shown by Figure 7.1 and Figure 7.2.
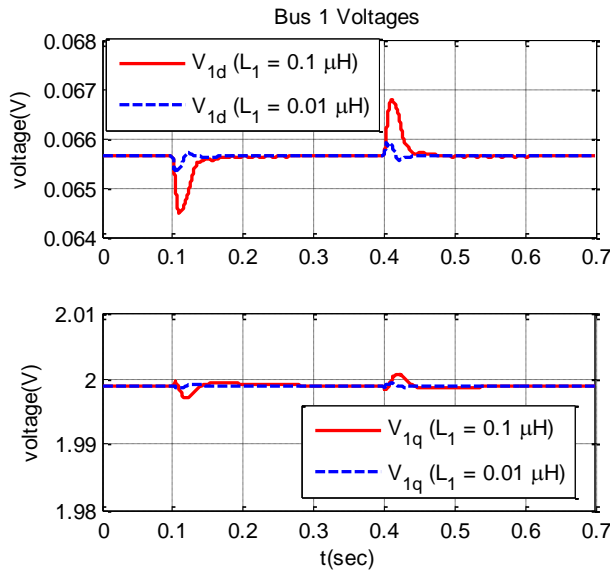
Figure 7.1: Bus 1 voltages as a function of time with varying power electronics inductor sizes.
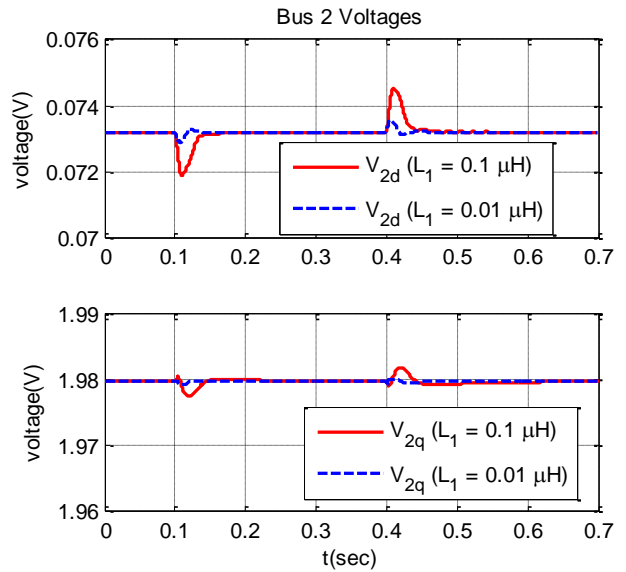
Figure 7.2: Bus 2 voltages as a function of time with varying power electronics inductor sizes.

Furthermore, if too large of an inductor is used, then the time-scale separation assumption that the power electronics dynamics are faster than the rest of the system may not hold and the system may go unstable as a result. For a larger disturbance, a smaller inductor is needed to prevent much effect on the

rest of the system. In theory, the inductor should be made as small as possible. However, there exists a practical limit because the wire itself in the power electronics will have some effective inductance, usually in the nH range, which is a function of the wire length and diameter [75].

7.2. Power Electronics Capacitor

The dc-link capacitance C_1 needs to be made large enough in order to keep the duty ratios within the feasible limits during transients following the disturbance. If C_1 is too small, the magnitude of the capacitor charge q_{C1} can decrease sharply during transients following the disturbance. As shown by (5.52), (5.53), (5.29), and (5.30), if the magnitude of the capacitor charge decreases, then the absolute values of the duty ratios increase. In order for the control to be feasible, the duty ratios need to remain within the physical limits given by (4.47) and (4.48). Therefore, if C_1 is too small, this can cause the duty ratios to go outside of the feasible limits during transients. Once the duty ratios hit saturation, there is no guarantee the control will work successfully.

This problem is demonstrated by decreasing C_1 from 2 F to 0.25 F for the simulation in Section 6.3.1. Figure 7.3 shows that the capacitor voltage decreases much more during transients when using the smaller capacitance, and Figure 7.4 shows that this, in turn, causes the duty ratios of the switches to increase beyond the feasible limits.

For a larger disturbance, a larger capacitor is needed to ensure that the duty ratios will stay within their feasible limits and that the transient stabilization will work successfully. In sizing the capacitor, there exists a trade-off between the size of disturbance the flywheel controller can handle and the economic cost of making a large capacitor.

108

Figure 7.3: Power electronic capacitor voltage as a function of time with varying power electronics capacitor sizes.
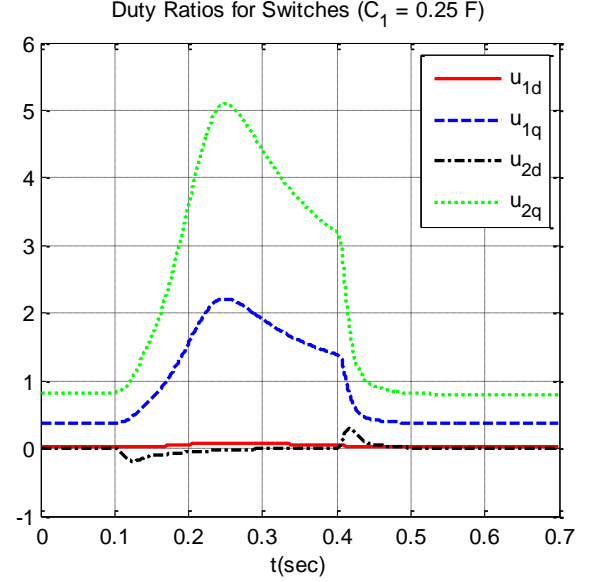
Figure 7.4: Simulation showing that the duty ratios of the switch positions can increase beyond feasible limits in transients when the size of the capacitor is decreased.

7.3. Power Electronics Resistance in Parallel with Capacitor

In the previous section, it was shown that a large capacitor is needed to keep the duty ratios within feasible limits during transients. A large resistor R_{C1} in parallel with the capacitor is needed in order to keep the duty ratios within feasible limits during steady state. As described in Section 6.2, the flywheel set point is chosen so that, in steady-state, the majority of power entering the power electronics after the resistor R_1 is sent to the flywheel. The remaining power is dissipated by R_{C1}, and this power is given by

$$P_{RC1} = \frac{q_{C1}^{2}}{C_1^{2} R_{C1}} \tag{7.1}$$

If R_{C1} decreases, then the absolute value of the capacitor charge q_{C1} must decrease in order to dissipate the same power P_{RC1}. Again, if the magnitude of the capacitor charge decreases, then the absolute values of the duty ratios increases, possibly beyond the feasible duty ratio limits. This problem is demonstrated by decreasing R_{C1} from 25 Ω to 2.5 Ω for the simulation in Section 6.3.1. Figure 7.5 shows that the steady-state voltage across the power electronic capacitor is much lower when

$R_{C1} = 2.5\,\Omega$. This in turn causes the duty ratios to be outside feasible limits during steady-state, as

shown by Figure 7.6.
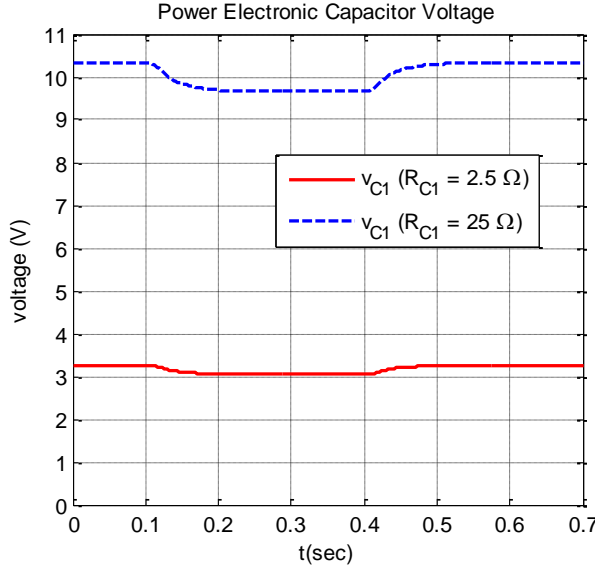
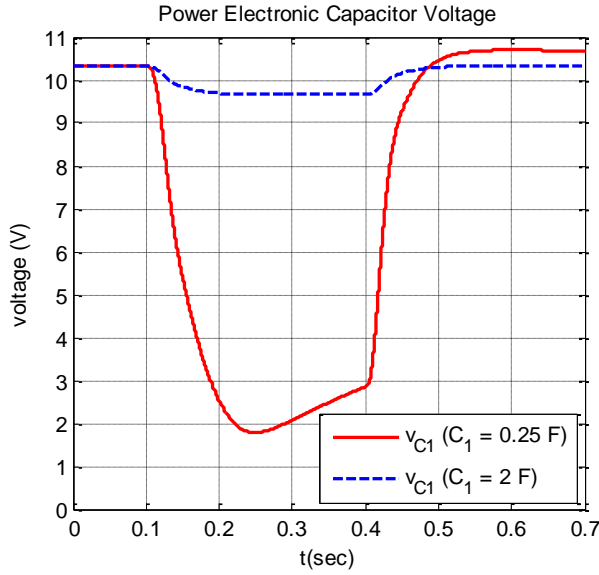**Figure 7.5:** Power electronic capacitor voltage as a function of time with varying resistor sizes.

Figure 7.6: Simulation showing that the duty ratios of the switch positions can increase beyond feasible limits when the size of the resistor is decreased.

Mathematical limits for R_{C1} can be found. Substituting the duty ratios expressions for u_{1d}, u_{1q}, u_{2d},

and u_{2q} given by (5.52), (5.53), (5.29), and (5.30) respectively into the duty ratio limits given by (4.47)

and (4.48), the following expressions are obtained

$$\frac{4C_1^2}{q_{C1}^2}\left[\left(V_{1d} - R_1 i_{1d}^{ref} + L_1 i_{1q}^{ref}\omega_1\right)^2 + \left(V_{1q} - R_1 i_{1q}^{ref} - L_1 i_{1d}^{ref}\omega_1\right)^2\right] \le 2 \tag{7.2}$$

$$\frac{4C_1^2}{q_{C1}^2}\left[\left(v_{S2d}^{ref}\right)^2 + \left(v_{S2q}^{ref}\right)^2\right] \le 2 \tag{7.3}$$

Using (7.1), (7.2) and (7.3) can be re-written in terms of R_{C1}

$$R_{C1} \ge 2\frac{\left(V_{1d} - R_1 i_{1d}^{ref} + L_1 i_{1q}^{ref}\omega_1\right)^2 + \left(V_{1q} - R_1 i_{1q}^{ref} - L_1 i_{1d}^{ref}\omega_1\right)^2}{P_{RC1}} \tag{7.4}$$

$$R_{C1} \ge 2\frac{\left(v_{S2d}^{ref}\right)^2 + \left(v_{S2q}^{ref}\right)^2}{P_{RC1}} \tag{7.5}$$

110

While a sufficiently large resistor is needed to keep the duty ratios within feasible limits, it should also be noted that too large of a resistor could cause voltage breakdown of the capacitor. As given by (7.1), as R_{C1} increases, the capacitor charge q_{C1} (and hence the capacitor voltage) increases as well. There exists a maximum breakdown voltage of the capacitor, where very large electric fields between the capacitor plates cause the dielectric to become conductive and the resulting large currents may damage the capacitor [76]. Typical values for capacitor breakdown voltage range from a few Volts to a few kV, depending on the gap between the plates and other capacitor design factors [77].

7.4. Percentage of Maximum Flywheel Reference Speed

As given by (6.34), the flywheel reference speed $\omega_2{}^{ref}$ converges to $\rho\omega_2^{ref\,max}$ in steady-state where ρ is a constant close to 1 and $\omega_2^{ref\,max}$ is the maximum reference speed based on the passivity-based control law stability condition given by (6.27). As ρ increases, the power sent to the flywheel increases and the power dissipated by R_{C1} decreases. As shown in (7.1), if P_{RC1} decreases, then q_{C1} decreases, which in turn causes the duty ratios to increase. Therefore, just like decreasing the resistor R_{C1}, increasing ρ can cause the duty ratios of the switches to increase beyond feasible limits. This issue is demonstrated by increasing ρ from 0.95 to 0.99 for the simulation in Section 6.3.1. Figure 7.7 shows that the steady-state voltage across the power electronic capacitor is much lower when $\rho = 0.99$. This in turn causes the duty ratios to be outside feasible limits during steady-state, as shown by Figure 7.8.

In terms of ρ, the power dissipated by the resistor is

$$P_{RC1} = \left(1 - \rho^2\right)\left(\frac{R_{S2}B_2{}^2 v_{R2}{}^2}{3/2 M_2{}^2 R_{R2}{}^2} + B_2\right)\omega_2^{ref\,max} \qquad (7.6)$$
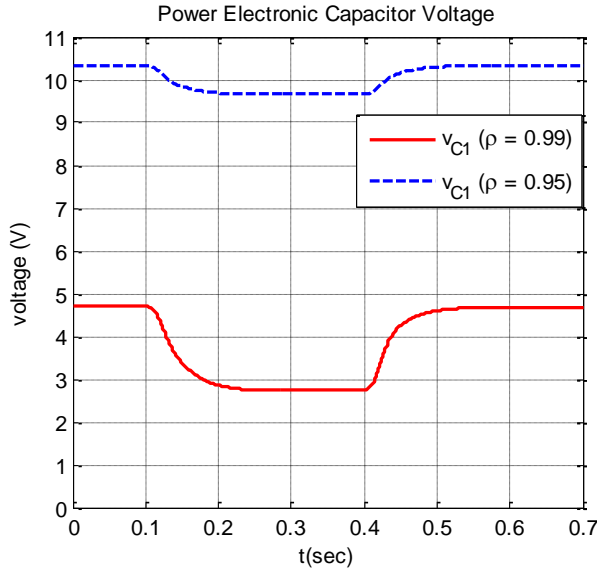
Figure 7.7: Power electronic capacitor voltage as a function of time with varying percentages of maximum flywheel reference speed.

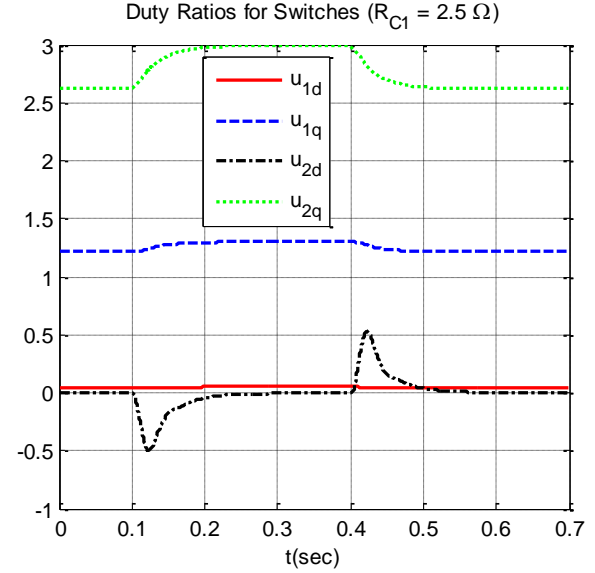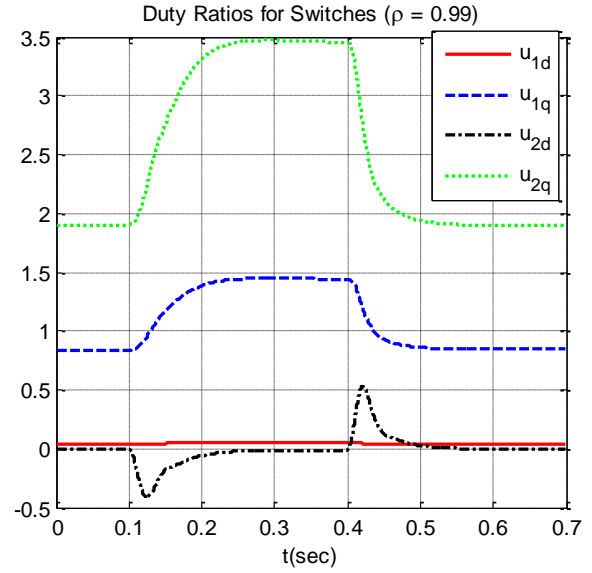**Figure 7.8:** Simulation showing that the duty ratios of the switch positions can increase beyond feasible limits when the percentage of the flywheel maximum reference speed is increased.

Substituting (7.6) into (7.4) and (7.5), the following restraints are obtained.

$$R_{C1} \geq 4 \frac{\left(V_{1d} - R_1 i_{1d}^{ref} + L_1 i_{1q}^{ref} \omega_1\right)^2 + \left(V_{1q} - R_1 i_{1q}^{ref} - L_1 i_{1d}^{ref} \omega_1\right)^2}{\sqrt{2}\left(1-\rho^2\right)\left(\dfrac{R_{S2}B_2^{\ 2}v_{R2}^{\ 2}}{3/2 M_2^{\ 2} R_{R2}^{\ 2}} + B_2\right)\omega_2^{ref\,max}} \tag{7.7}$$

$$R_{C1} \geq 2 \frac{\left(v_{S2d}^{ref}\right)^2 + \left(v_{S2q}^{ref}\right)^2}{\left(1-\rho^2\right)\left(\dfrac{R_{S2}B_2^{\ 2}v_{R2}^{\ 2}}{3/2 M_2^{\ 2} R_{R2}^{\ 2}} + B_2\right)\omega_2^{ref\,max}} \tag{7.8}$$

It is evident from (7.7) and (7.8) that as ρ increases, R_{C1} must increase as well in order to keep the switch duty ratios from hitting saturation. However, it should be noted that, in practice, there is a limit to how large R_{C1} can be. In a real capacitor, the dielectric between the plates has a small, but non-zero, conductivity, which is modelled as an ideal capacitor in parallel with a large leakage resistor [78]. Typical values for the leakage resistance of a capacitor range from 1 MΩ to 100,000 MΩ [78]. The shunt resistance R_{C1} of the capacitor can be made smaller than the internal leakage resistance by adding an additional wire in parallel with the capacitor, but R_{C1} cannot be made any larger than the leakage

112

resistance. Therefore, the optimal strategy for maximizing the efficiency of the flywheel controller would probably be to set ρ as high as possible, given the leakage resistance limit of R_{C1}, in order to still maintain the switch duty ratios within feasible limits.

7.5. Summary

This chapter analyzes the effect of changing the power electronic parameters on the control performance and discusses how these parameters should be sized. The power electronic inductor should be made as small as practically possible given the effective wire inductance. In sizing the dc-link capacitor, there is a trade-off between the size of disturbance the flywheel controller can handle without the switch duty ratios reaching saturation during transients and the cost of making a large capacitor. Finally, it is shown that in order to increase the percentage of power entering the power electronics that is sent to the flywheel, the resistor in parallel with the capacitor must increase as well in order for the duty ratios to remain within feasible limits during steady-state. There is, however, a limit to how large the resistance can be, due to the internal shunt leakage resistance of a real capacitor.

8. Demonstration of Flywheel Controller on Larger Systems

Chapter 6 introduced using the flywheel variable speed drive controller for transient stabilization of a simple two-bus system with one flywheel and one wind generator with a disturbance. This chapter discusses and demonstrates transient stabilization of larger power systems with multiple flywheels and multiple wind generators with different disturbances. Flywheels are placed at each bus with one or more wind generators, which are the potential disturbance locations. Each flywheel controller is responsible for absorbing the disturbances on that bus so that the rest of the system is minimally affected, using the set point logic described in Chapter 6.

If a bus has more than one wind generator (a wind farm), still only one flywheel is needed for that bus, as the flywheel is responsible for absorbing all the wind power disturbances at that bus. This is demonstrated for the three-bus example described in Section 8.1. Next, in Section 8.2, the Sao Miguel island power system is considered using real-world data. It is proposed to replace the three diesel generators on Sao Miguel with wind generators since diesel generators emit harmful environmental pollutants. Flywheels are added along with each wind generator, and it is shown that the flywheel controllers help maintain the power system stability and reduce the voltage oscillations in response to persistent wind power disturbances.

8.1. Three-Bus Power System with a Wind Farm

Consider the three-bus system shown in Figure 8.1. The parameters used in this example are given in Appendix B. Again, the synchronous machine has governor and exciter control in order to regulate the frequency of the system to 60 Hz, and the four wind generators are modeled as induction machines. There is a wind farm on Bus 2 with three wind generators and another wind generator on Bus 3, which all have mechanical torque disturbances, as shown in Figure 8.2. While the three wind generators on Bus 2 have the same parameters and the same pre-disturbance mechanical torques, each wind generator has different disturbances of varying magnitude and length, as shown by Figure 8.2. The flywheel on Bus 2 is responsible for absorbing the disturbances of the three wind generators on Bus 2 while the flywheel on

Bus 3 is responsible for absorbing the disturbance of the wind generator on Bus 3. The constant current source method described in Section 6.1.1 for choosing the controller set points is used for this example. The system starts in steady-state prior to the disturbances beginning at 0.1 seconds.
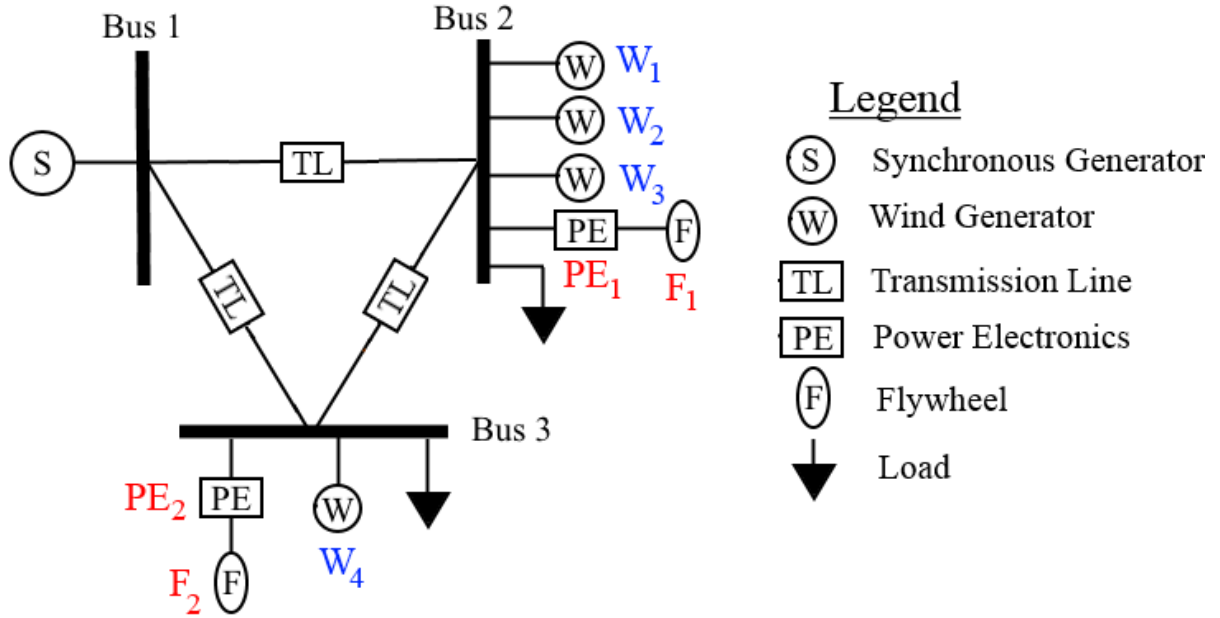
Figure 8.1: Three-bus power system with a wind farm on Bus 2.
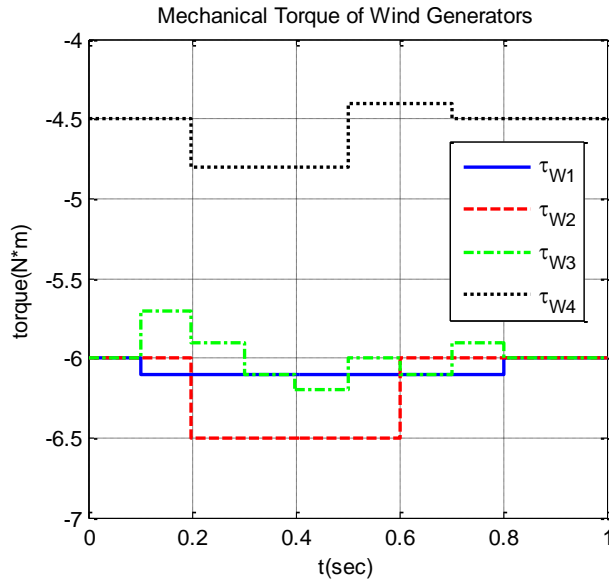
Figure 8.2: Mechanical torque disturbances of the four wind generators.
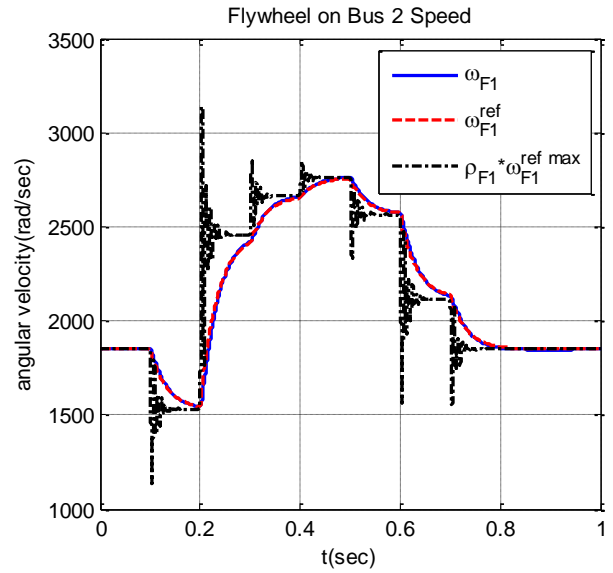
Figure 8.3: Speed of the flywheel on Bus 2 as a function of time.

Figure 8.3 and Figure 8.4 show the speeds of the flywheels on Bus 2 and Bus 3 respectively. As discussed in Section 6.2, the reference flywheel speeds $\left(\omega_{F1}^{ref}, \omega_{F2}^{ref}\right)$ change much slower than the

115

maximum reference flywheels speeds $\left(\omega_{F1}^{ref\,max}, \omega_{F2}^{ref\,max} \right)$ so that the time-scale separation in the variable

speed drive controllers still applies. While ω_{F2} settles to a new steady-state during the disturbance, ω_{F1}

never reaches a new steady-state value during the disturbance due to the fast-changing mechanical torque

τ_{W3} of the third wind generator on Bus 2 shown in Figure 8.2.
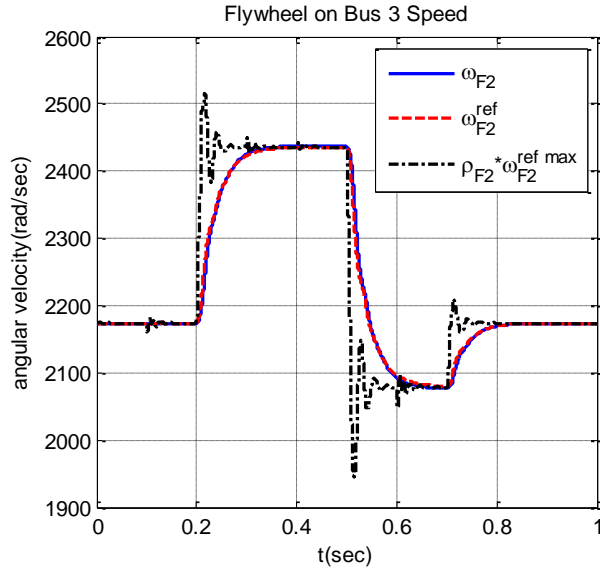
Figure 8.4: Speed of the flywheel on Bus 3 as a function of time.
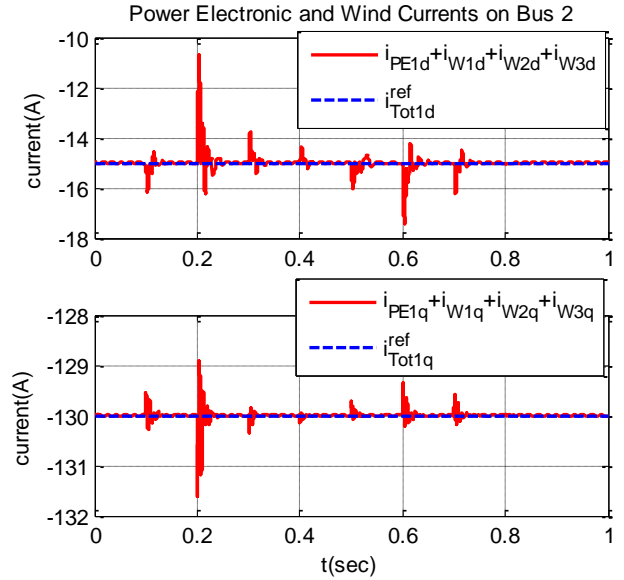
Figure 8.5: Sum of the power electronic currents and the wind generator stator currents on Bus 2, compared to the reference total currents, as function of time.

In this case, one flywheel on Bus 2 is sufficient for absorbing all three wind generator disturbances.

However, with more wind generators on the bus or larger disturbances, it may be necessary to add

multiple flywheels on the bus due to the maximum flywheel speed limit resulting from the tensile strength

of the flywheel material, as discussed in Section 6.2

Figure 8.5 and Figure 8.6 show the sum of the power electronic currents and the wind generator stator

currents, as well as the reference total currents, for Bus 2 and Bus 3 respectively. Due to the controller,

the power electronics and the wind generator together behave very nearly as a constant current source,

even with the wind power disturbances. Since the power electronic dynamics are not instantaneous, there

are some fast oscillations in the total currents after each disturbance, but the total currents quickly return

to their reference values.
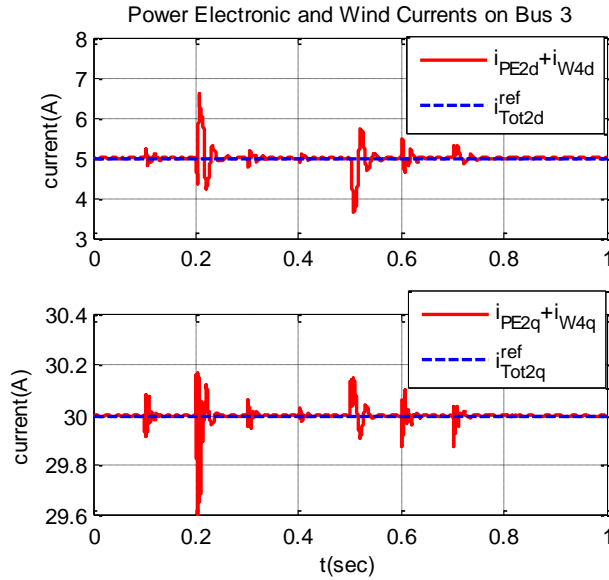
Figure 8.6: Sum of the power electronic currents and the wind generator stator currents on Bus 3, compared to the reference total currents, as function of time.
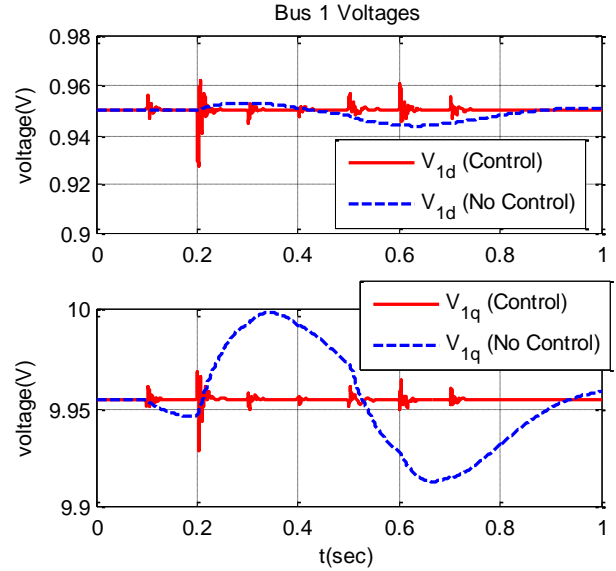
Figure 8.7: Bus 1 voltages as a function of time with control compared to without control.
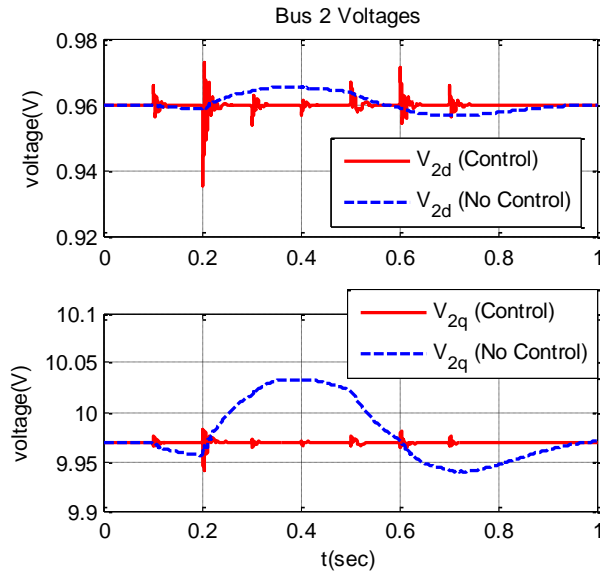
Figure 8.8: Bus 2 voltages as a function of time with control compared to without control.
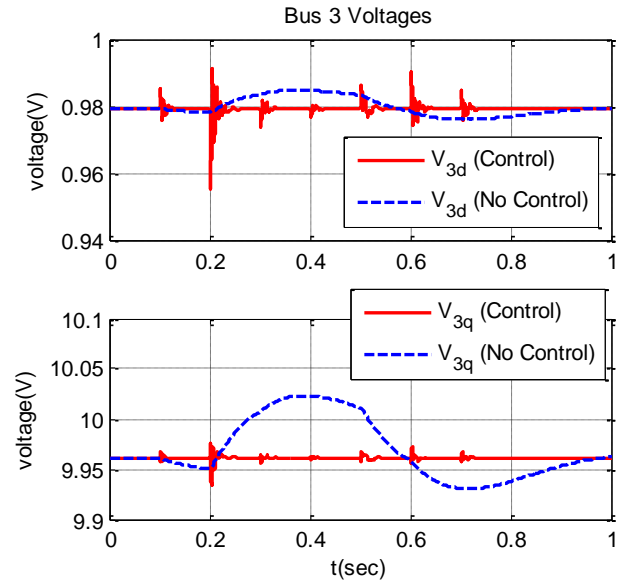
Figure 8.9: Bus 3 voltages as a function of time with control compared to without control.

The Bus 1, Bus 2, and Bus 3 voltages are shown in Figure 8.7, Figure 8.8, and Figure 8.9

respectively, both with and without the control. (In the case with no control, constant values are used for

117

the switch duty ratios.)   Due to the controller, the effect of the disturbance on the rest of the system is very minimal and lasts only a very short time. The oscillations are much smaller with the control than without the control, and also, with the control, the voltages quickly return to their pre-disturbance values after each disturbance, unlike without the control.

8.2.   Sao Miguel Power System Example

Next, the Sao Miguel island power system, which was analyzed in [79] and is shown in Figure 8.10, is considered using real-world data. Sao Miguel is the largest of the nine Azores Archipelago islands located in the middle of the North Atlantic Ocean. The Sao Miguel power system has fifteen buses, three diesel generators, two geothermal generators, and ten hydro generators.
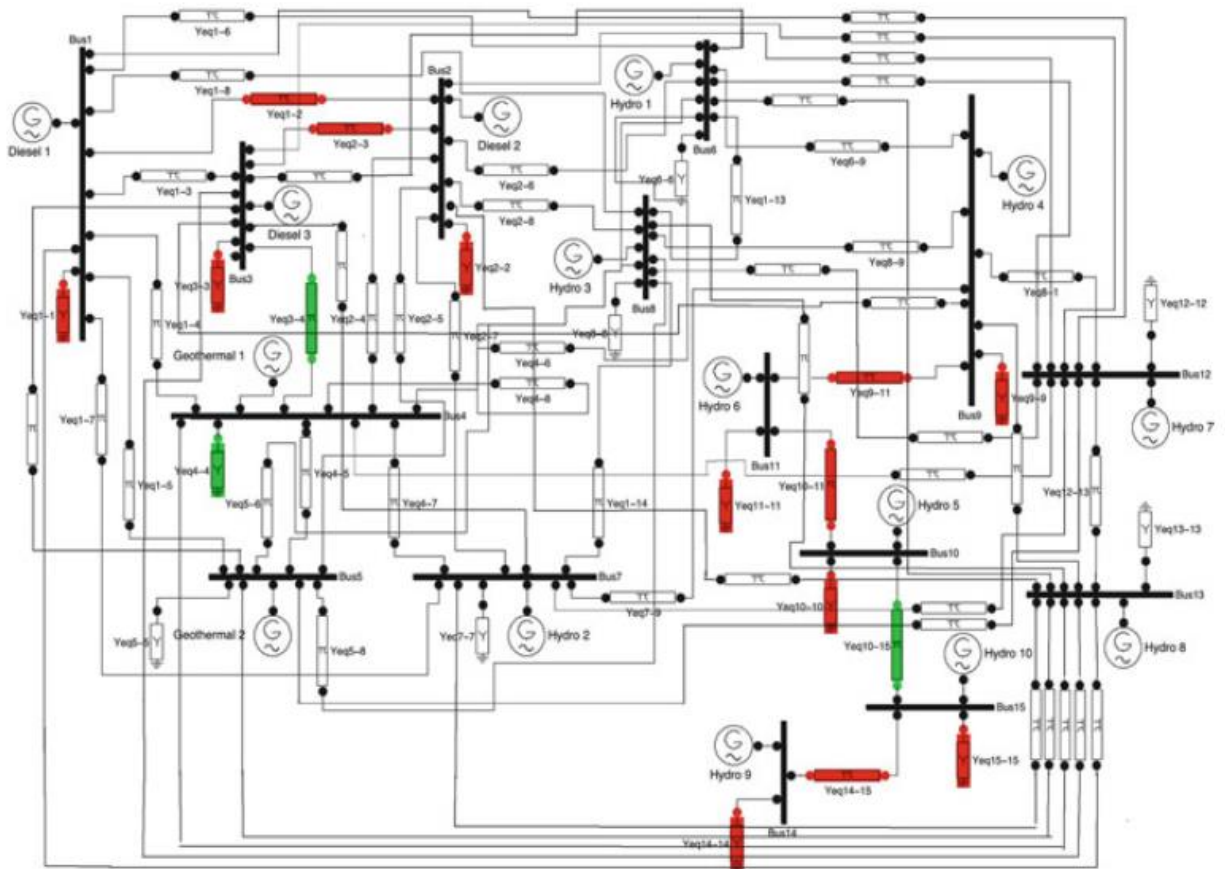
Figure 8.10: Sao Miguel power system topology.

Since diesel generators emit harmful environmental pollutants [80], it is proposed in this section to replace the three diesel generators with wind generators.   Since wind power is difficult to predict and

118

control, flywheels are added along with each wind generator. Again, the variable speed drive controller described in Chapter 5 and Chapter 6 is used so that the flywheel absorbs the wind power variation and the rest of the system is minimally affected. The flywheels help the system maintain stability and minimize voltage and frequency deviations in response to the persistent wind power deviations.

The dynamics of all components are modelled, including the loads and the transmission lines. The hydro generators are modelled as synchronous machines with governor and exciter control in order to regulate the frequency of the system to 50 Hz. (The Azores island use 50 Hz grid frequency, as Europe does, rather than the 60 Hz grid frequency used in North America.) The geothermal generators are modelled as synchronous machines without governor or exciter controllers [19]. The wind generators are again modelled as induction machines.
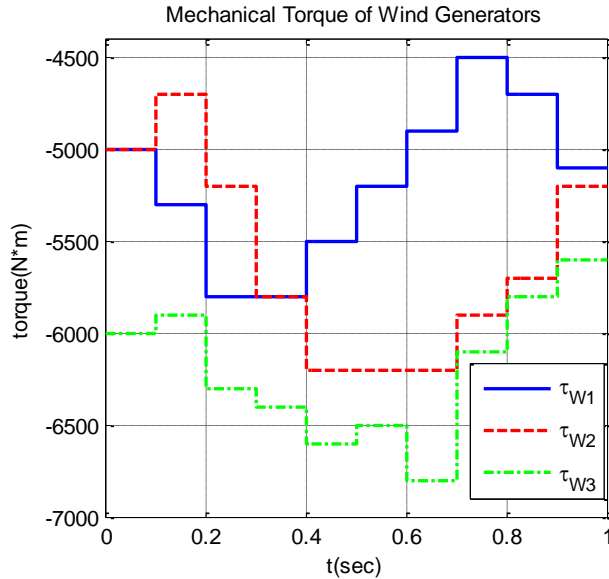
Figure 8.11: Mechanical torque disturbances of the four wind generators.
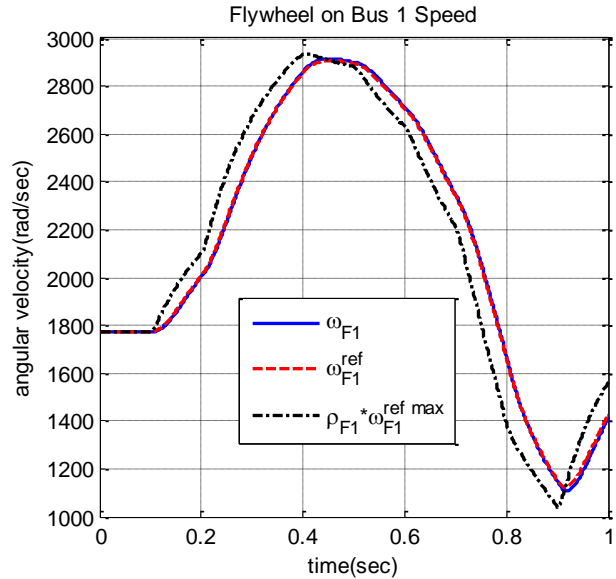
Figure 8.12: Speed of the flywheel on Bus 1 as a function of time.

The parameters used for the three wind generators and the three flywheels are given in Appendix C. The parameters for the rest of the system are based on real-world data and are given in [79]. The mechanical torque disturbances of the three wind generators are shown in Figure 8.11. The constant current source method described in Section 6.1.1 for choosing the controller set points is again used for this example. The system starts in steady-state prior to the disturbances beginning at 0.1 seconds.
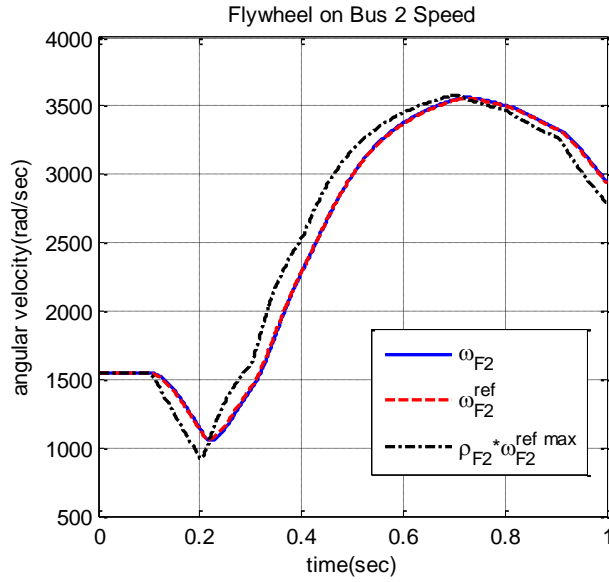
Figure 8.13: Speed of the flywheel on Bus 2 as a function of time.
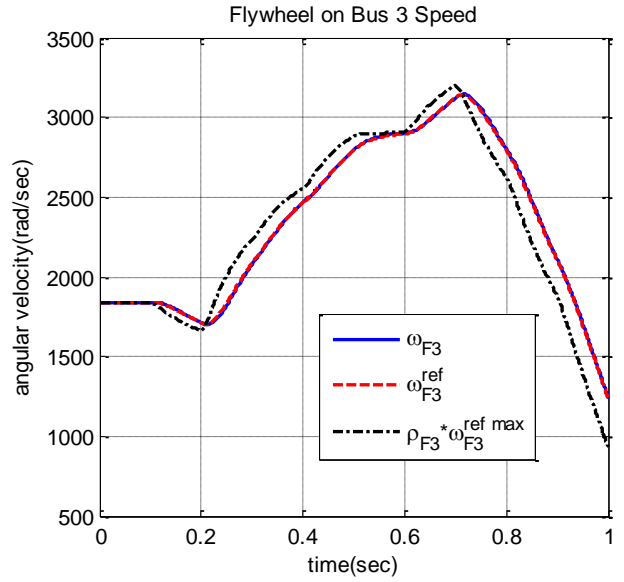
Figure 8.14: Speed of the flywheel on Bus 3 as a function of time.

Figure 8.12, Figure 8.13, and Figure 8.14 show the speeds of the flywheels on Bus 1, Bus 2 and Bus 3 respectively. Due to the persistent wind generator disturbances, the flywheel speeds never settle to a new steady-state value following the first disturbance.

Figure 8.15, Figure 8.16, and Figure 8.17 show the sum of the power electronic currents and the wind generator stator currents, as well as the reference total currents, for Bus 1, Bus 2, and Bus 3 respectively. Due to the controller, the power electronics and the wind generator together on each bus behave very nearly as a constant current source, even with the wind power disturbances. For comparison, Figure 8.15, Figure 8.16, and Figure 8.17 also show the sum of the power electronic currents and the wind generator stator currents on each bus without the controller. (In the case with no control, constant values are used for the switch duty ratios.)

The Bus 1, Bus 2, and Bus 3 voltages are shown in Figure 8.18, Figure 8.19, and Figure 8.20 respectively, both with and without the control. The voltage oscillations without the controller are relatively small in this case, but it is evident that the flywheel controller still reduces the oscillations.
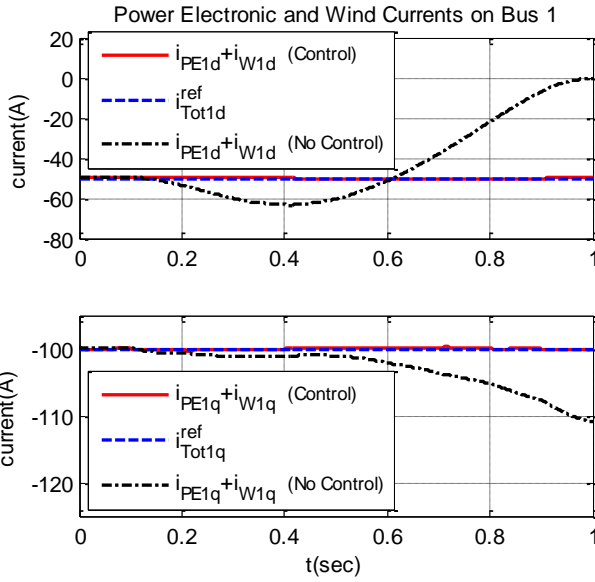
Figure 8.15: Sum of the power electronic currents and the wind generator stator currents on Bus 1 with and without control, as well as the reference total currents, as function of time.
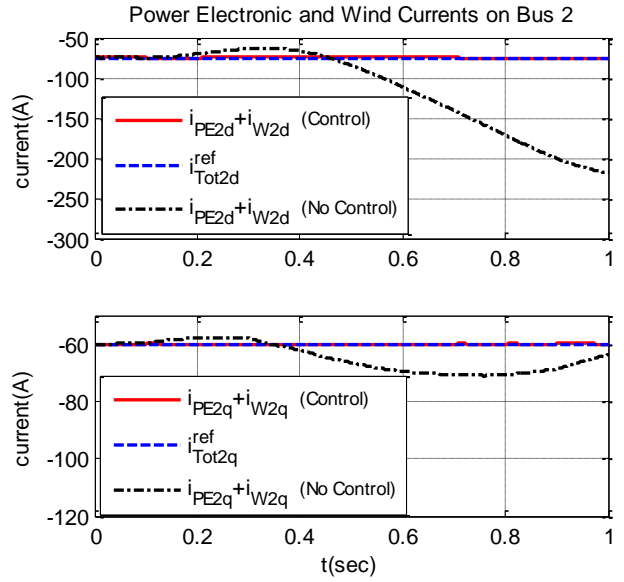
Figure 8.16: Sum of the power electronic currents and the wind generator stator currents on Bus 2 with and without control, as well as the reference total currents, as function of time.
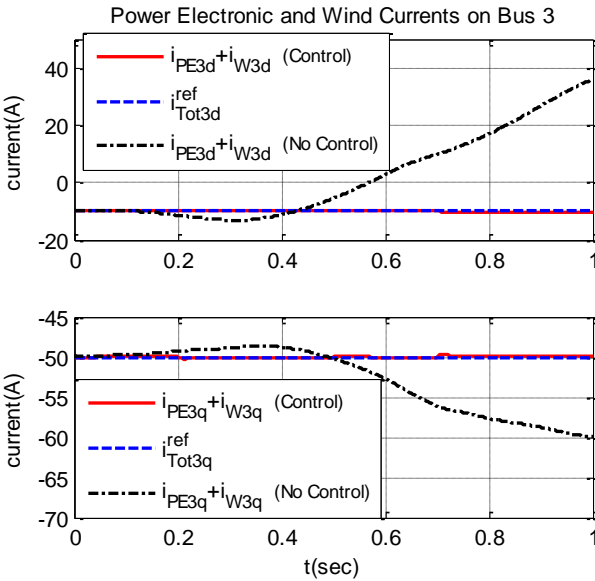
Figure 8.17: Sum of the power electronic currents and the wind generator stator currents on Bus 3 with and without control, as well as the reference total currents, as function of time.
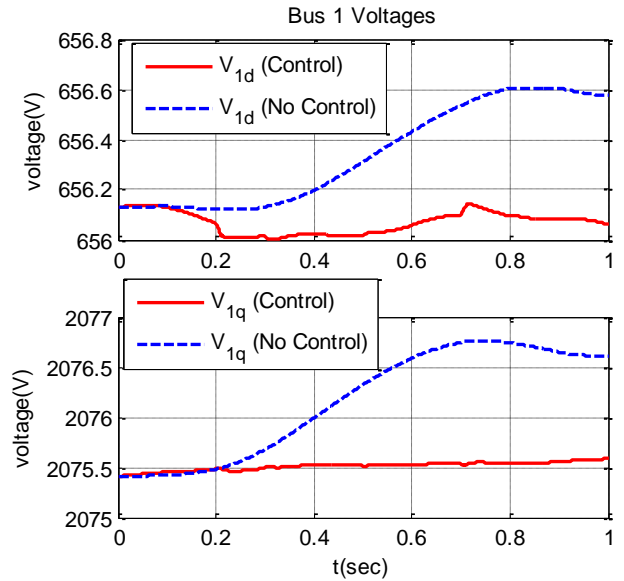
Figure 8.18: Bus 1 voltages as a function of time with control compared to without control.
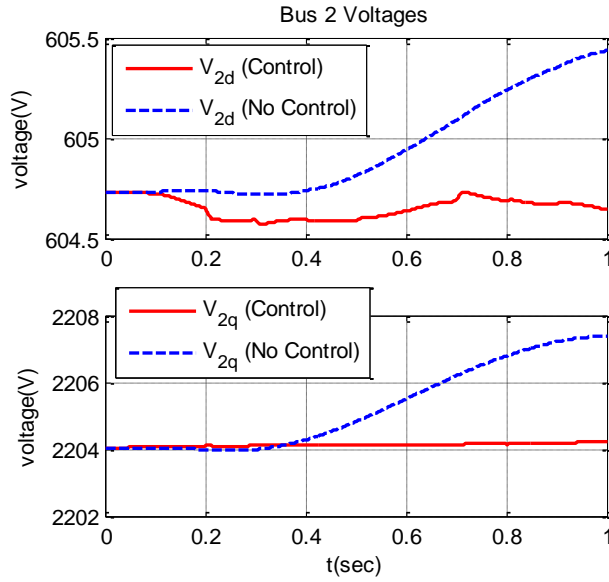
Figure 8.19: Bus 2 voltages as a function of time with control compared to without control.
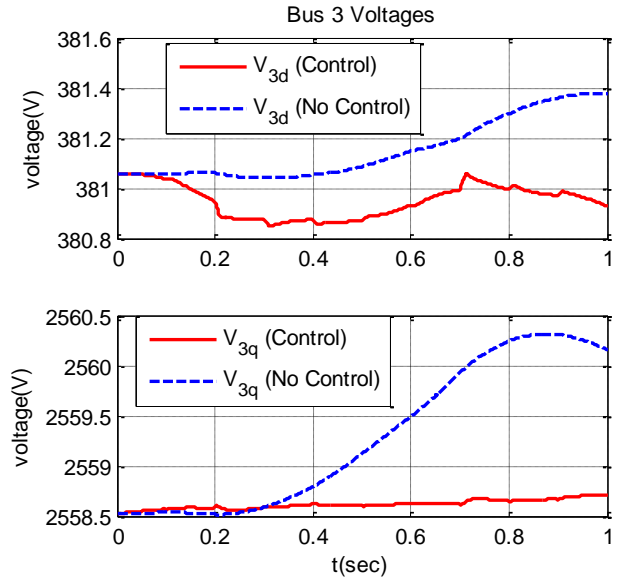
Figure 8.20: Bus 3 voltages as a function of time with control compared to without control.

8.3. Summary

This chapter demonstrated transient stabilization of larger power systems with multiple flywheels and multiple wind generators. Flywheels are placed at each bus with one or more wind generators, which are the potential disturbance locations. Further research could involve designing transient stabilization control using fewer flywheels. For example, instead of placing one flywheel at each bus with a wind generator, it would be interesting to examine if one flywheel could be responsible for absorbing the disturbance at its bus and also the disturbance at a neighboring bus with a wind generator. This would require designing cooperative control logic, as in [2].

122

9. Passive Magnetic Bearing Design

One main design challenge in the actual implementation of flywheels is to support the high-speed rotor. It is advantageous to use magnetic bearings instead of conventional mechanical bearings in order to decrease frictional energy losses. Magnetic bearings are contactless and therefore can exhibit near-zero losses. Magnetic bearings can either be active or passive. Active magnetic bearings use position sensors and electronic circuits that control electromagnets to achieve stable levitation of the rotating element. In contrast, passive magnetic bearings do not have any sensors or control. Most commercial magnetic bearings are active, but active magnetic bearings have a far higher cost than passive magnetic bearings.

A significant challenge with passive magnetic bearings is achieving stable magnetic levitation of an object in all directions. An object can be levitated using either attractive or repulsive magnetic levitation, but both methods are inherently unstable in one direction. For example, a magnet can be levitated using the repulsive force from a lower magnet. There is an equilibrium position, where the downward gravitational force on the upper magnet exactly equals the upward magnetic levitation force, but while this equilibrium is stable to vertical displacements, it is not stable to lateral displacements. Inevitably, the upper magnet will slide sideways. Alternatively, a magnet can be levitated using the attractive force from an upper magnet. There is again an equilibrium position, where the downward gravitational force exactly equals the upward magnetic levitation force, but while this equilibrium is stable to lateral displacements, it is not stable to vertical displacements. This problem is generalized further in Earnshaw's Theorem, which states that it is not possible to stably levitate an object in all directions using any configuration of only permanent magnets and fixed currents [81].

A possible approach using passive magnetic bearings pursued by Argonne National Laboratory is to use superconducting elements [82]. Because superconductors have diamagnetic properties, they evade Earnshaw's Theorem and can stably levitate an object in all directions. Diamagnets are materials with a relative magnetic permeability less than one. However, since superconductors must be kept at very low

temperatures (below -150 ˚C), it is not practical to employ superconductor passive magnetic bearings for flywheel energy storage systems.

Another possible solution pursued by Lawrence Livermore National Lab (LLNL) is to add a Halbach array stabilizer, which induces currents in stabilization coils, to the levitation magnet system [83]. Previous literature on computing the forces and stiffness for passive magnetic bearings relies on several simplifications, such as neglecting the curvature of the geometry and neglecting the higher order harmonics of the magnetic fields [83]. This chapter provides a novel, more accurate analysis which does not make these simplifying assumptions.

A passive magnetic bearing system for flywheels, based on an early LLNL design, which can stably levitate the flywheel in all directions, is shown in Figure 9.1. The resultant magnetic fields and forces for this magnetic bearing system are computed in this chapter using electromagnetic theory, demonstrating that stable levitation is achieved in all directions with this design.
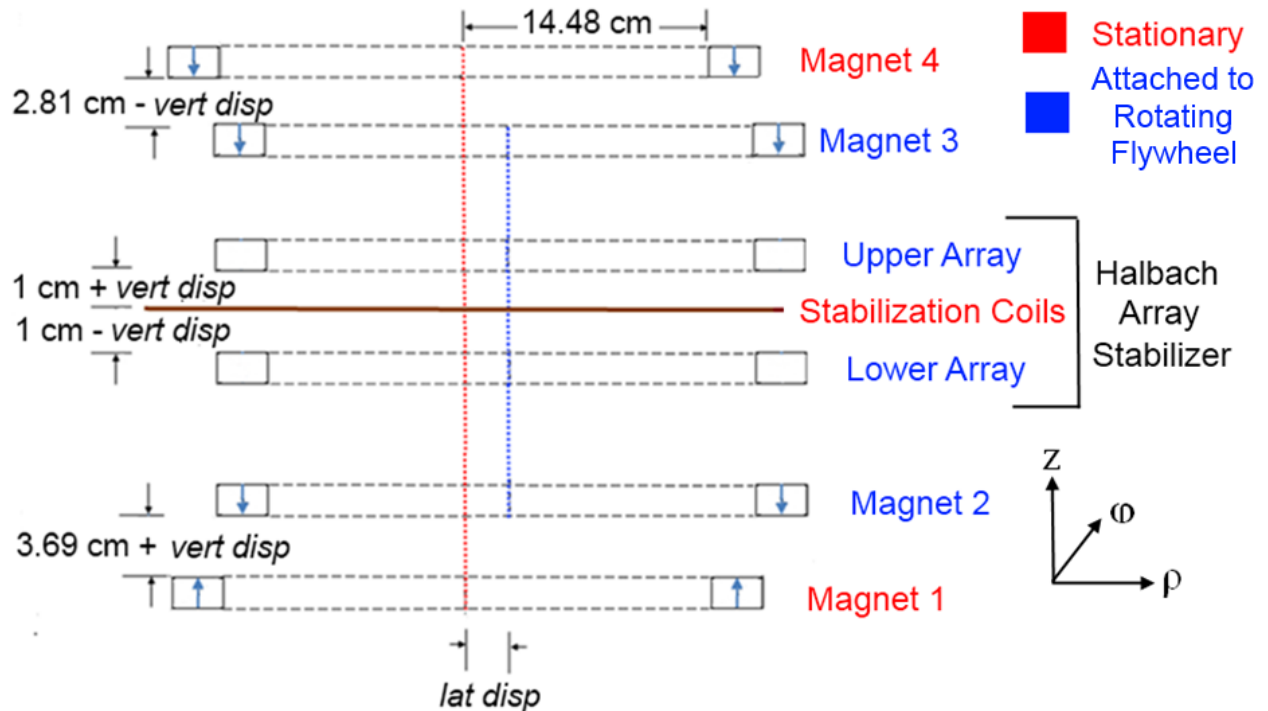
Figure 9.1: Cross-sectional view of the passive magnetic bearing geometry

9.1. Levitation Magnet System

Magnets 1-4 form the levitation magnet system. Magnets 1 and 4 are stationary while Magnets 2 and 3 are attached to the bottom and top of the rotating flywheel respectively. Neodymium permanent magnets (NdFeB) with a remanent field B_r of 1.35 T are used for all four magnets, and each magnet has the shape of an annular ring, as portrayed by Figure 9.2. For the specific example that is shown, each ring has a height h of 1.27 cm, an inner radius a of 14.48 cm, and an outer radius b of 19.56 cm. When the radial displacement of the axis of the flywheel, *lat disp*, is zero, the rotor magnets are co-axial with the stationary magnets. When the axial displacement of the flywheel, *vert disp*, is zero, the upper attracting magnets are 0.88 cm closer to each other than the lower repelling magnets,

The upper levitation magnet pair exerts an attracting upward force on the flywheel while the lower levitation magnet pair exerts a repelling upward force on the flywheel. At the equilibrium position (when *vert disp* = 0 cm and *lat disp* = 0 cm), the total upward magnetic force exactly equals the total downward gravitational force on the flywheel, 2046 N. Since the upper attracting magnets are closer than the lower repelling magnets, the levitation magnet system is stable in the lateral direction but unstable in the vertical direction.
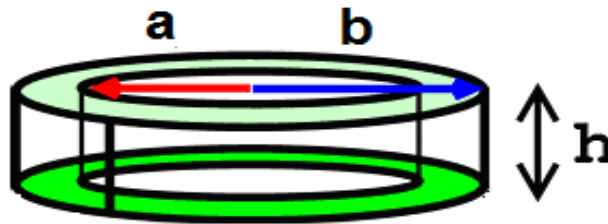
Figure 9.2: Shape of each levitation magnet

9.1.1. Magnetic Fields from Permanent Magnets

In order to calculate the magnetic levitation force from each magnet pair, it is first necessary to compute the magnetic fields from a permanent magnet. A permanent magnet can be modeled as two uniform charged surfaces using the coulombian approach [84] or equivalently as two sheets of uniform current density using the amperian current approach [85]. Using the coulombian approach, since each permanent magnet has a known magnetization, its contribution to the total field can be calculated from

patches of magnetization surface charge density at the surfaces where the magnetization is discontinuous [86]. The magnetization surface charge density at the boundary between regions 1 and 2 is

$$\rho_{sm} = \hat{a}_{n12} \bullet \mu_0 (\vec{M}_1 - \vec{M}_2) \tag{9.1}$$

where $\hat{a}_{n12}$ is the unit normal vector from region 1 to 2, $\vec{M}_1$ and $\vec{M}_2$ are the magnetization vectors in regions 1 and 2, and μ_0 is the permeability of free space: $4\pi \times 10^{-7}$ H/m. The units of ρ_{sm} are Vsec/m^2.

Therefore, an annular ring magnet that is polarized in the positive vertical direction can be modeled as a patch of positive surface charge density on the top surface of the ring and a patch of negative surface charge density on the bottom surface of the ring. Both surfaces have the shape of annuli.

In the most general formulation, the magnetic field from a patch of magnetization surface charge can be obtained by numerically integrating

$$\vec{H} = \int_S \frac{\rho_{sm}}{4\pi\mu_0 R^2} \hat{a}_R ds \tag{9.2}$$

where S is the surface of magnetic charge, ρ_{sm} is the magnetic surface charge density, R is the distance from the differential surface element to the observation point, and $\hat{a}_R$ is the unit vector pointing from the differential surface element to the observation point. This formulation is analogous to Coulomb's Law for electric charge density.

For an annular surface of charge, while no closed-form expression can be found, the double integral in (9.2) can be simplified to a single integral, as expressed in [22], which is more computationally efficient. To numerically evaluate the single integral, the MATLAB numerical integration function 'quad' is used with an error tolerance of 1e-2. The total field from an annular ring magnet is computed by summing the contributions from the two annular patches. The magnetic flux density $\vec{B}$ can then be easily obtained from the constitutive relationship

$$\vec{B} = \mu_0 (\vec{H} + \vec{M}) \tag{9.3}$$

9.1.2.   Magnetic Forces between Permanent Magnets

As described in [22], the force exerted by Magnet 1 on Magnet 2 is calculated by summing the individual force on each of the two magnetization surface charge patches on Magnet 2. While no closed-form expression can be found, the force on a patch of surface charge is computed by numerically integrating

$$\overrightarrow{F}_{1on2} = \int_{S_2} \rho_{sm2} \overrightarrow{H}_1 ds \tag{9.4}$$

where S_2 is the surface of magnetic charge on Magnet 2, $\overrightarrow{H}_1$ is the magnetic field from Magnet 1, and ρ_{sm2} is the magnetic surface charge density of the patch on Magnet 2. This formulation is analogous to Coulomb's Law for electric charge density. To numerically evaluate the double integral, the MATLAB 'dblquad' function is used with an error tolerance of 1e-3. When Magnet 2 is coaxial to Magnet 1, there is only a vertical force. However, if the axis of Magnet 2 is displaced off the axis of Magnet 1, then there is also a lateral force in the direction of displacement.

The force exerted by Magnet 4 on Magnet 3 is calculated using the same procedure. The total force exerted on the flywheel from the levitation magnet system is the sum of the force exerted by Magnet 1 on Magnet 2 and the force exerted by Magnet 4 on Magnet 3. Even though Magnets 2 and 3 are rotating in the azimuthal direction, since all the levitation magnets are symmetric in the azimuthal direction, the force is constant with time.

Figure 9.3 shows the vertical forces as a function of *vert disp* at several values of *lat disp* and Figure 9.4 shows the lateral forces as a function of *lat disp* at several values of *vert disp*. At the equilibrium position (*vert disp* = 0 cm, *lat disp* = 0 cm), there is no lateral force and the upward magnetic vertical force exactly equals the downward gravitational force of 2046 N on the flywheel. The equilibrium is stable in the lateral direction because a small increase in lateral displacement causes a negative force in the direction of displacement, which acts to move the flywheel back to its equilibrium position. However, the equilibrium is unstable in the vertical direction because a small increase in vertical displacement

causes an increase in vertical force, which acts to move the flywheel further from its equilibrium position. The instability of the levitation magnet system in one direction is consistent with Earnshaw's Theorem.
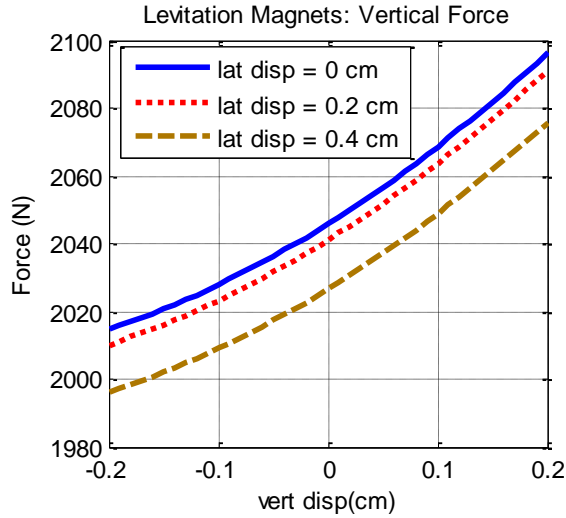
Figure 9.3: Vertical forces as a function of vertical displacement for the levitation magnets
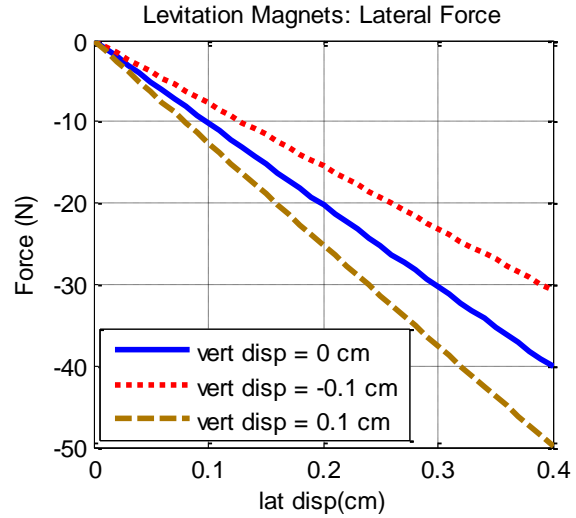
Figure 9.4: Lateral forces as a function of lateral displacement for the levitation magnets.

9.2. Halbach Array Stabilizer

The Halbach array stabilizer shown in Figure 9.1 is designed to stabilize the system in the vertical direction.   The stabilizer consists of two stationary stabilization coils centered in the vertical direction between two Halbach arrays attached to the rotating flywheel. In a Halbach array, the magnetizations rotate from one magnet to the next in order to augment the field on one side of the array while nearly cancelling the field on the other side.

Top views of the upper and lower Halbach arrays are shown in Figure 9.5. In each array, there are 24 wavelengths and 96 magnets. The magnetizations of the individual magnets rotate between the vertical (z) direction and the azimuthal (φ) direction. For the upper Halbach array, the rotation of magnetizations causes the strong side field to be below the array while for the lower Halbach array, the rotation of magnetizations causes the strong side field to be above the array. The inner radius of each array is 14.48 cm while the outer radius of each array is 19.56 cm. The height of each array (not shown by the top view)

is 1.27 cm. Neodymium permanent magnets are again used, and each individual magnet has the shape of a trapezoidal prism.

Figure 9.6 shows a top view of the two stabilization coils, which also consists of 24 wavelengths. The second stabilization coil is identical to the first coil and is placed in the same vertical plane, but the second coil is rotated one quarter of a wavelength in the counter-clockwise direction with respect to the first coil. Each stabilization coil consists of 48 straight segments and 48 semi-circular loops. There are 24 wavelengths around each coil, and the wavelength of each coil equals the wavelength of the Halbach arrays. The inner radius of each coil is 14.6 cm while the outer radius is 20.3 cm. The radius of the inner semi-circles is 0.9 cm while the radius of the outer semi-circles is 1.33 cm.
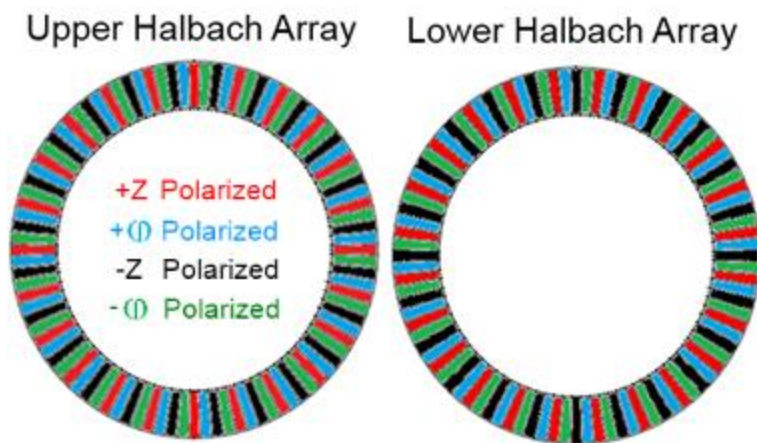
Figure 9.5: Top view of the upper and lower Halbach arrays
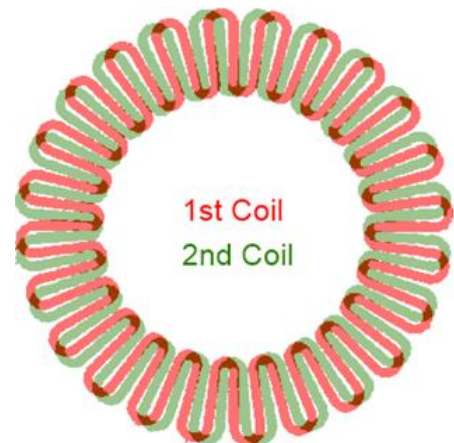
Figure 9.6: Top view of the stabilization coils

If the stabilization coils are exactly centered between the two Halbach arrays in the vertical direction, the flux through the coils from the upper array cancels the flux from the lower array and no current is induced. If, however, the flywheel is displaced in the vertical direction, the stabilization coils will no longer be exactly centered and the time-varying flux will induce a current in each coil. This current then interacts with the magnetic field of the Halbach arrays to provide a net stabilizing force in the vertical direction.

As will be shown in this chapter, the force as a function of time exerted by each stabilization coil on the Halbach arrays consists of a double frequency sinusoidal component and a constant component. Two

stabilization coils are used, so that the constant parts of the force exerted by each coil add together while the double frequency sinusoidal components cancel. Due to the mutual inductance between the two coils, the sinusoidal components do not exactly cancel, but the total force is much closer to a constant than it would be using only one coil.

9.2.1. Magnetic Fields from Halbach Arrays

A magnet in the Halbach array with polarization in the azimuthal direction is modeled as a patch of positive surface charge at the side wall where the magnetization vector terminates and a patch of negative surface charge at the side wall where the magnetization vector initiates. Both patches are rectangles and the surface charge density of each patch is determined using (9.1). For the magnetic field resulting from a rectangular patch of charge, a closed form expression of the double integral in (9.2) can be found and is given in [86].

A magnet that is polarized in the positive vertical direction is modeled as a patch of positive surface charge density on the top surface of the trapezoidal prism and a patch of negative surface charge density on the bottom surface of the prism. Both patches are trapezoids, and the surface charge density of each trapezoid is again determined using (9.1). Since a trapezoid is the sum of a rectangle and two triangles, the total magnetic field from a trapezoidal patch of charge is found by summing the contributions from the rectangular patch and the two triangular patches. For a triangular patch of charge, a closed form expression for the magnetic field can be found and is given in [24]. The total field from both Halbach arrays is computed by summing the contributions from each of the 192 rectangular patches and the 192 trapezoidal patches.

9.2.2. Magnetic Flux through Stabilization Coils

The magnetic flux from the arrays through each coil is computed by numerically integrating

$$\lambda_{Arrays,\, Coil} = \int_{S_{Coil}} \vec{B}_{Arrays} \bullet d\vec{s} \tag{9.5}$$

where S_{Coil} is the inner surface enclosed by the coil and $\vec{B}_{Arrays}$ is the total magnetic flux density from both arrays.

130

Since the surface normal to the stabilization coil is in the *z*-direction, only the *z*-component of the magnetic flux density needs to be integrated. The flux through each wavelength can be obtained by integrating the magnetic flux density over two triangular regions and two semicircular regions. As portrayed by Figure 9.7, the total flux through one wavelength is equal to the sum of the flux through regions 1, 2, and 3 minus the flux through region 4. To numerically compute the surface integrals, the "quad2d" function in MATLAB is used with an error tolerance of 1e-7.
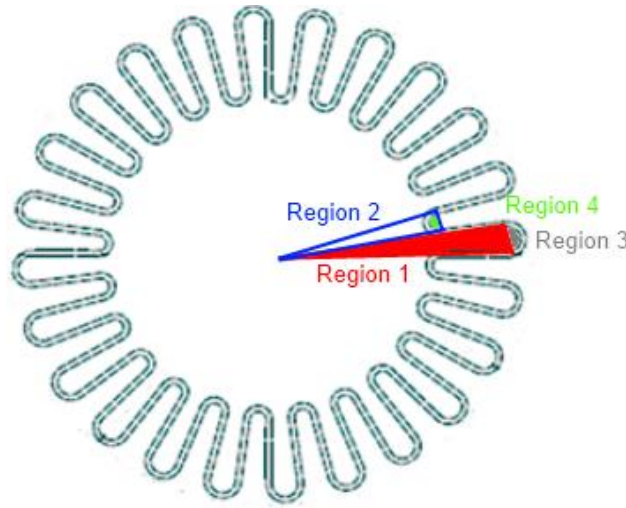
Figure 9.7: Flux through one wavelength of the stabilization coil is equal to the sum of the flux through regions 1, 2, and 3 minus the flux through region 4

If the stabilization coil is exactly centered between the two arrays (*vert disp* = 0 cm), the flux through the coil from the upper array cancels the flux from the lower array and there is zero net flux through the coil. When *vert disp* is non-zero, there is a time-varying flux through the coil since the arrays are rotating in the azimuthal direction and the arrays are not axially symmetric. The flux is, however, periodic with a period of the time it takes the arrays to rotate one wavelength. In all the simulations shown, the arrays are rotating at 1000 rpm, so the period is 2.5 ms.

When the lateral displacement of the arrays is zero, the flux through each wavelength of the coil is the same by symmetry, so it is sufficient to calculate the flux through one wavelength and then multiply by 24, the number of wavelengths, to obtain the total flux. When the arrays are displaced in the lateral direction, however, the flux through each wavelength of the coil is different, so it is necessary to compute the flux through each of the 24 wavelengths.

131

Additionally, since the second stabilization coil is rotated one quarter of a wavelength in the counter-clockwise direction with respect to the first coil, when the lateral displacement is zero, the flux through the second coil lags the flux through the first coil by exactly 90°. When the lateral displacement is non-zero, this is no longer true, although for small lateral displacements, this is still a good approximation.

As an example, Figure 9.8 shows the flux through each of the stabilization coils as a function of time for one period when the arrays are rotating at 1000 rpm, *vert disp* = 0.1 cm, and *lat disp* = 0.2 cm.
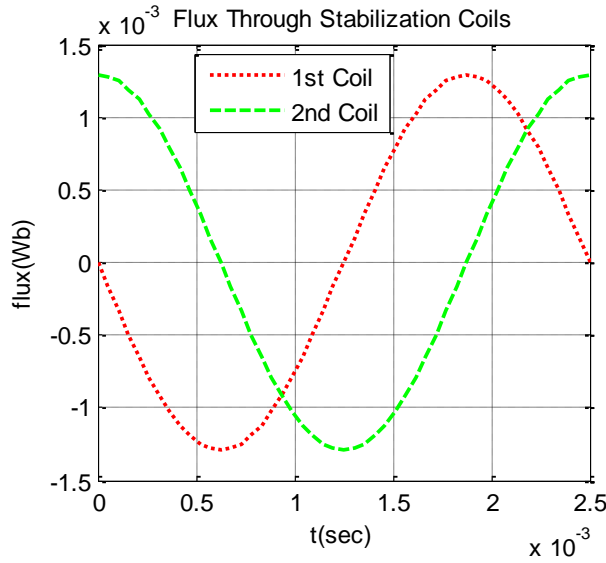
Figure 9.8: Flux as a function of time through each stabilization coil with *vert disp* = 0.1 cm, *lat disp* = 0.2 cm, and the arrays rotating at 1000 rpm
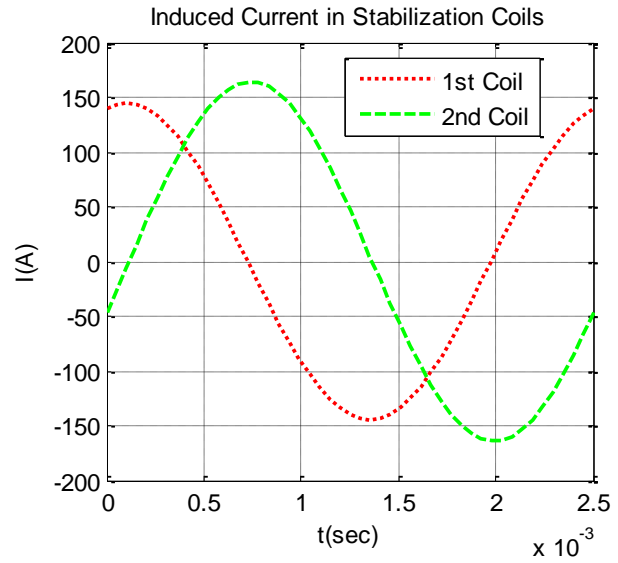
Figure 9.9: Induced current as a function of time through each stabilization coil with *vert disp* = 0.1 cm, *lat disp* = 0.2 cm, and the arrays rotating at 1000 rpm

9.2.3.   Induced Currents in Stabilization Coils

The time-varying magnetic flux induces a current in each of the stabilization coils, as described by

$$RI_{Coil\,1} + L\frac{dI_{Coil\,1}}{dt} + M\frac{dI_{Coil\,2}}{dt} = -\frac{d\lambda_{Arrays,Coil\,1}}{dt} \tag{9.6}$$

$$RI_{Coil\,2} + L\frac{dI_{Coil\,2}}{dt} + M\frac{dI_{Coil\,1}}{dt} = -\frac{d\lambda_{Arrays,Coil\,2}}{dt} \tag{9.7}$$

where *R* is the resistance of each coil, *L* is the self-inductance of each coil, and *M* is the mutual inductance between the two coils. Calculations of these parameters are described in [24].

If the mutual inductance were neglected, the induced current in the 2nd coil would merely lag the induced current in the 1st coil by 90°. However, the mutual inductance causes the amplitude of the induced current in the second stabilization coil to be slightly greater than the current in the first coil.

As an example, Figure 9.9 shows the induced current in each of the stabilization coils as a function of time for one period when the arrays are rotating at 1000 rpm, *vert disp* = 0.1 cm, and *lat disp* = 0.2 cm.

9.2.4. Magnetic Forces on Halbach Arrays

The induced current interacts with the magnetic field of the Halbach arrays to provide a net stabilizing force in the vertical direction. The most computationally efficient way to calculate the restoring force on the Halbach arrays is to first calculate the force on the stabilization coil using the Lorentz Force Law. The force on the Halbach arrays exerted by each stabilization coil is computed by numerically integrating

$$\vec{F}_{CoilOnArrays} = -\vec{F}_{ArraysOnCoil} = -\int_{C_{Coil}} I_{Coil} d\vec{l} \times \vec{B}_{Arrays} \qquad (9.8)$$

where I_{Coil} is the current in the stabilization coil, $\vec{B}_{Arrays}$ is the magnetic flux density from both arrays, and C_{Coil} is the contour of the stabilization coil.

For a nominal flywheel rotational speed of 1000 rpm, the vertical and lateral forces are periodic with period 2.5×10^{-3} s, the amount of time it takes the arrays to rotate one wavelength. As an example, Figure 9.10 and Figure 9.11 show the vertical and lateral forces exerted by each coil on the Halbach arrays as a function of time for one period when *vert disp* = 0.1 cm, *lat disp* = 0.2 cm, and the flywheel is rotating at 1000 rpm. If the mutual inductance between the two stabilization coils were neglected, the total force exerted by both coils would be a constant. However, the unequal current amplitudes due to the mutual inductance cause the total force to still have a double frequency sinusoidal component, whose amplitude is much smaller than the constant part.

133
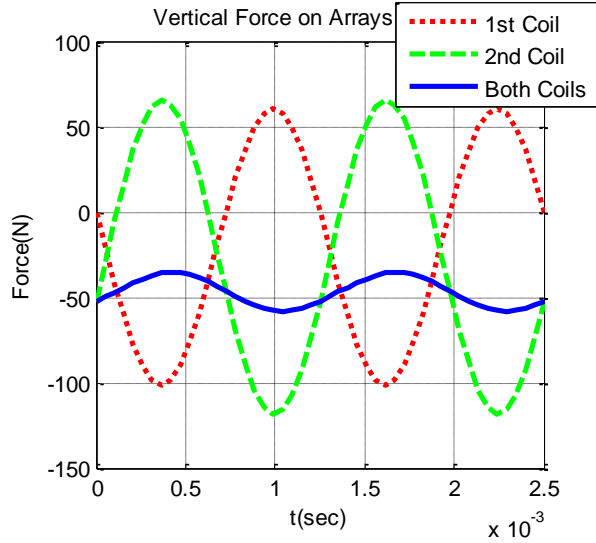
Figure 9.10: Vertical force exerted by each coil on the arrays with *vert disp* = 0.1 cm, *lat disp* = 0.2 cm, and the arrays rotating at 1000 rpm
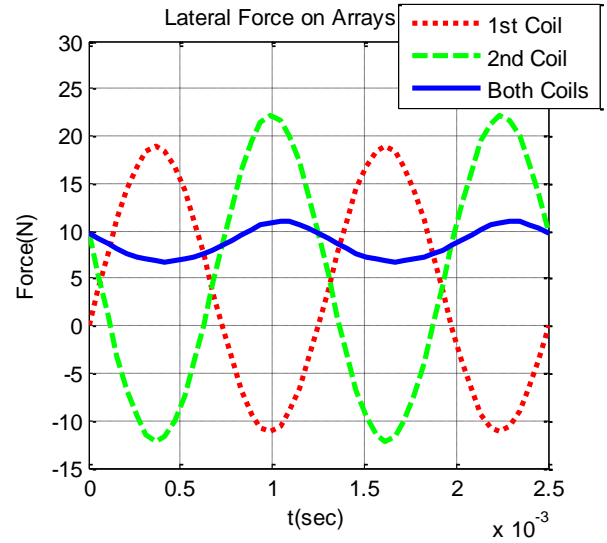
Figure 9.11: Lateral force exerted by each coil on the arrays with *vert disp* = 0.1 cm, *lat disp* = 0.2 cm, and the arrays rotating at 1000 rpm.
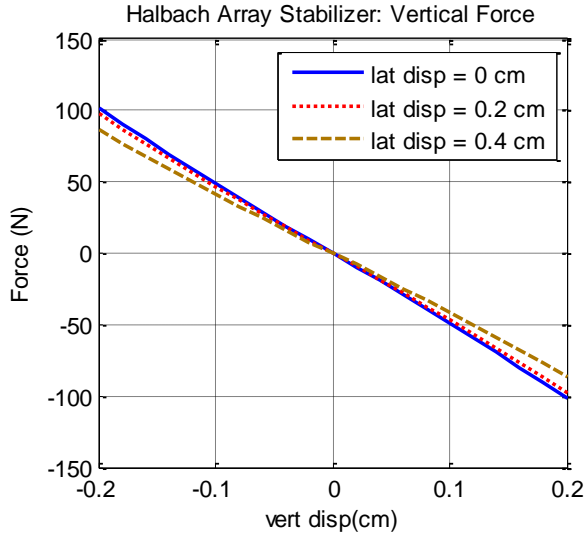
Figure 9.12: Vertical forces as a function of vertical displacement for the Halbach array stabilizer
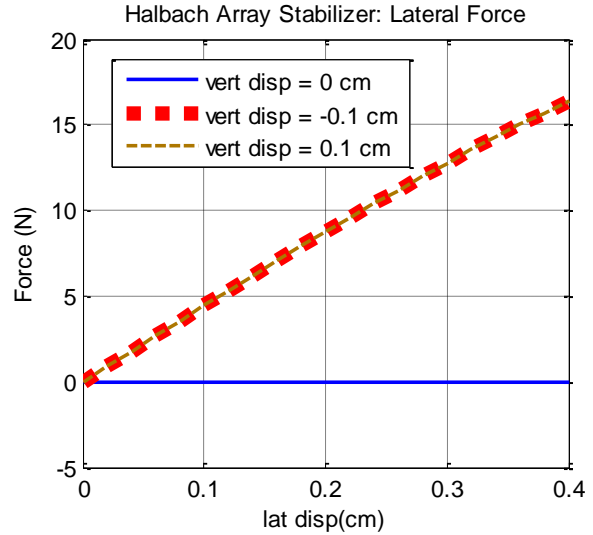
Figure 9.13: Lateral forces as a function of lateral displacement for the Halbach array stabilizer

Since the sinusoidal component of the force exerted by both stabilization coils is small and the frequency is high, time-average forces are used to analyze the force from the stabilizer as a function of vertical or lateral displacements. The total force on the flywheel is the sum of the forces from the levitation magnets and from the Halbach array stabilizer. Figure 9.12 shows the time-average vertical force as a function of *vert disp* at several different values of *lat disp* while Figure 9.13 shows the time-average lateral forces as a function of *lat disp* at several different values of *vert disp*. While the Halbach

array stabilizer provides a stabilizing force to vertical displacements, it actually provides a destabilizing force to lateral displacements from the equilibrium. However, since the levitation magnet system is stable in the lateral direction, the total magnetic bearing system consisting of both the levitation magnets and the Halbach array stabilizer is stable to lateral displacement, as will be shown in the next section

9.3. Entire Magnetic Bearing System

The total force for the entire magnetic bearing system consisting of both the levitation magnets and the Halbach array stabilizer can now be analyzed. The total force on the flywheel is the sum of the force on the flywheel from the levitation magnets calculated in Section 9.1.2 and the force on the flywheel from the Halbach array stabilizer calculated in Section 9.2.4. Figure 9.14 shows the total time-average vertical force as a function of *vert disp* at several different values of *lat disp* while Figure 9.15 shows the total time-average lateral force as a function of *lat disp* at several different values of *vert disp*.
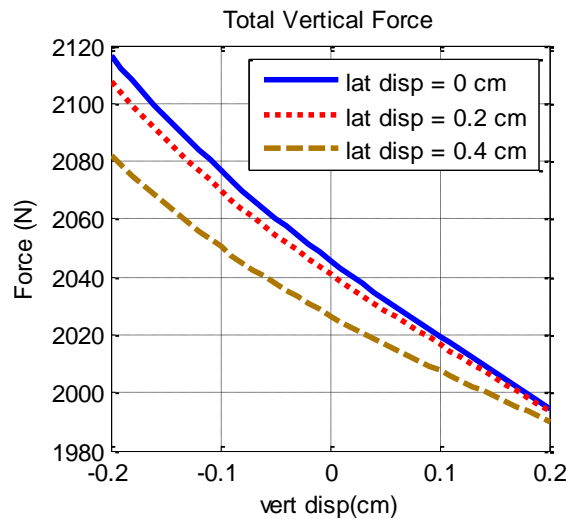
Figure 9.14: Vertical forces as a function of vertical displacement for the entire bearing system
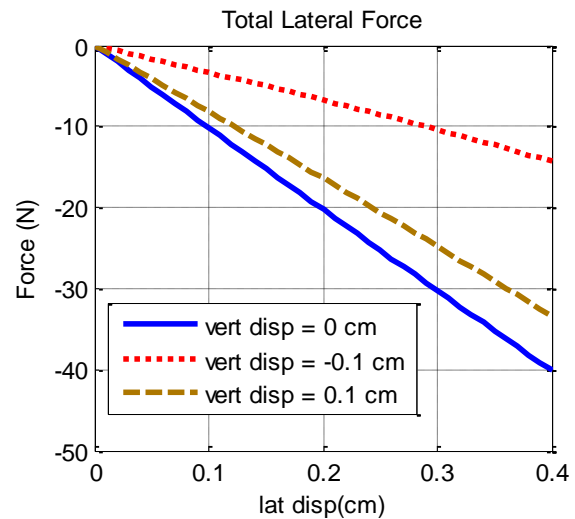
Figure 9.15: Lateral forces as a function of lateral displacement for the entire bearing system

The equilibrium position occurs when *vert disp* = 0 cm and *lat disp* = 0 cm. At this position, there is no lateral force and the upward magnetic vertical force exactly equals the downward gravitational force of 2046 N. The equilibrium is stable in the lateral direction because a small increase in lateral displacement causes a negative force in the direction of displacement, which acts to move the flywheel back to its equilibrium position. The equilibrium is also stable in the vertical direction because a small increase in

vertical displacement causes a decrease in vertical force, which acts to move the flywheel back to its equilibrium position.

9.4. Summary

This chapter presented a novel, more accurate analysis of a passive magnetic bearing design that can stably levitate the flywheel in all directions. The bearing system consisted of levitation magnets coupled with a Halbach array stabilizer, which induces currents in stabilization coils, in order to overcome the inherent instability of a system composed only of permanent magnets. Electromagnetic theory was used to compute the magnetic fields, forces, and stability of the bearing system.

Further research could involve combining the magnetic forces computed in this chapter with the gyroscopic dynamics of the flywheel to assess the tilt stability of the magnetic bearing system. Further research could also include an analysis of the drag torque on the flywheel, which adds to the frictional losses of the system. The drag torque occurs only when the flywheel is displaced in the vertical direction and currents are induced in the stabilization coils. In order to increase the efficiency of the flywheel, the drag torque should be made as low as possible. In this design, Halbach arrays are used for the stabilizer in order to make the stabilizer very stiff to vertical displacements from the equilibrium position. This serves to keep the stabilization coils very close to the null flux plane, which minimizes the losses from induced currents in the stabilization coils

10. Conclusions and Future Work

Since wind power is difficult to predict and control, large sudden disturbances in wind power generation can cause high deviations in frequency and voltage or even transient instabilities Current industry practices for transient stabilization are inefficient or do not guarantee stability. A potential solution examined in this thesis is to add flywheel energy storage systems, along with the renewable energy sources, into future power grids. Flywheels can respond faster than conventional generators and could stabilize the system in response to wind power disturbances until slower generators can respond. The work in this thesis analyzes the design, modeling, and power electronic control for using flywheels for transient stabilization of power grids.

The following approach for transient stabilization using flywheels is described. First, the state space model for the interconnected system is obtained so that control using the flywheel can be designed and tested for provable performance. Next, flywheels are placed at each bus with wind generators, which are the potential disturbance locations.   Then, a novel variable speed drive controller for flywheels is developed using passivity-based control logic in order to minimize the effect of the large sudden wind power disturbances on the rest of the system. New contributions are also made in determining the size of the power electronic parameters, given a certain range of disturbances. Due to the complex nature of large interconnected power systems, novel computer-aided methods are implemented both for symbolically deriving the state space model of the interconnected system and for symbolically deriving the passivity-based control law given desired closed-loop energy functions.

A variable speed drive controller for flywheels is developed using time-scale separation and this automated passivity-based control logic. Switches in the power electronics interfacing between the flywheel and the rest of the power grid are controlled in order to regulate both the flywheel speed and the power electronic currents to desired set points. When using this controller for transient stabilization of an interconnected power system in response to wind power disturbances, the controller set points are chosen so that the flywheel absorbs this disturbance and the rest of the system is minimally affected. Simulation results are shown demonstrating the effectiveness of flywheels and this control logic for transient

stabilization of interconnected power systems in response to large sudden wind power disturbances for several examples, including the real-world Sao Miguel power system.

Finally, a novel analysis of a passive magnetic bearing design for flywheels is presented, where currents are induced in stabilization coils in order to achieve stable levitation of the flywheel in all directions. Passive magnetic bearings have far less frictional energy losses than mechanical bearings and are less expensive than active magnetic bearings because sensors and feedback control systems are not necessary to install.

This thesis assumed that the locations of the disturbances were known (the locations with the wind generator). Additional research is needed to design a more general flywheel controller for situations where the locations of the disturbances are not known. For example, short circuits could potentially happen anywhere on the grid. This would require designing cooperative control, as in [2], where a flywheel in one region could be used to transiently stabilize the grid in response to a disturbance or fault in another region. Further research could also involve combining the fast dynamics and control in this thesis with a higher level feedforward control, such as economic dispatch at the market level. In this case, the controller set points for the flywheel variable speed drive controller would be determined based on optimal power flow determined by the market. Also, assessing the effect of state estimation error on the proposed control methods is another open question for future work. In this thesis, it was assumed that all state variables could be sensed perfectly.

.

Appendices

A. Parameters Used in Two-Bus Power System Example

The parameters used for the two-bus transient stabilization example in Chapter 6 are given in Table

A.1-Table A.8.

Table A.1: Synchronous generator parameters

Symbol	Quantity	Value
L_R	Self-inductance of the rotor winding	5 μH
L_S	Self-inductance of the stator windings	5 μH
L_{SS}	Mutual inductance between the stator windings	1 μH
M	Mutual inductance between the stator and rotor windings when parallel	4 μH
R_R	Resistance of the rotor winding	2×10^{-2} Ω
R_S	Resistance of the stator windings	1×10^{-3} Ω
J	Inertia of the rotor	3×10^{-2} kg m^2
B	Damping coefficient of the rotor	1×10^{-3} N m s

Table A.2: Governor and exciter controllers for synchronous generator

Symbol	Quantity	Value
ω^{ref}	Reference speed for governor controller	377 rad/sec
K_P	Proportional gain for governor controller	1
K_I	Integral gain for governor controller	20
T_u	Time-constant for the mechanical torque	0.01
T_g	Time-constant for the valve position	0.001
K_t	Gain for the mechanical torque	400
r	Gain for the valve position	200
$v_{Terminal}^{\ ref}$	Terminal reference voltage for exciter controller	2 V
K_e	Gain for exciter controller	500

Table A.3: Transmission line parameters

Symbol	Quantity	Value
L_{TL}	Self-inductance of the transmission line	1×10^{-6} H
R_{TL}	Resistance of the transmission line	1×10^{-4} Ω
C_{TL}	Shunt capacitance of the transmission line	1×10^{-2} F

Table A.4: Load parameters

Symbol	Quantity	Value
L_L	Self-inductance of the load	1×10^{-4} H
R_L	Resistance of the load	1×10^{-2} Ω

Table A.5: Wind generator parameters

Symbol	Quantity	Value
L_R	Self-inductance of the rotor windings	2×10^{-5} H
L_{RR}	Mutual inductance between the rotor windings	4×10^{-6} H
L_S	Self-inductance of the stator windings	2×10^{-5} H
L_{SS}	Mutual inductance between the stator windings	2×10^{-6} H
M	Mutual inductance between the stator and rotor windings when parallel	1×10^{-5} H
R_R	Resistance of the rotor winding	2×10^{-3} Ω
R_S	Resistance of the stator windings	1×10^{-3} Ω
J	Inertia of the rotor	4×10^{-5} kg m^2
B	Damping coefficient of the rotor	1×10^{-4} N m s

Table A.6: Flywheel parameters

Symbol	Quantity	Value
L_{R2}	Self-inductance of the rotor winding	5 μH
L_{S2}	Self-inductance of the stator windings	5 μH
L_{SS2}	Mutual inductance between the stator windings	1 μH
M_2	Mutual inductance between the stator and rotor windings when parallel	4 μH
R_{R2}	Resistance of the rotor winding	2×10^{-3} Ω
R_{S2}	Resistance of the stator windings	1×10^{-3} Ω
V_{R2}	Voltage applied to the rotor winding	1 V
J_2	Inertia of the rotor	1×10^{-4} kg m^2
B_2	Damping coefficient of the rotor	2×10^{-5} N m s
τ_{M2}	Mechanical torque applied to the rotor	0 N m

Table A.7: Power electronics parameters

Symbol	Quantity	Value
C_1	Capacitance of dc-link capacitor	2 F
L_1	Inductance of power electronics inductor	0.01 μH
R_1	Resistance in series with inductor	0.01 mΩ
R_{C1}	Resistance of resistor in parallel with capacitor	25 Ω

Table A.8: Flywheel controller gains

Symbol	Quantity	Value
K_P	Proportional gain in the speed controller	0.03
K_I	Integral gain in the speed controller	0.3
K_S	Gain for the flywheel speed set point dynamics	30
ρ	Percent of maximum reference speed $\omega_2^{ref\ max}$ that is desired to obtain	95%

B. Parameters Used in Three-Bus Power System Example

The parameters used for the three-bus transient stabilization example in Chapter 8 are given in Table B.1-Table B.10.

Table B.1: Synchronous generator parameters

Symbol	Quantity	Value
L_R	Self-inductance of the rotor winding	5 μH
L_S	Self-inductance of the stator windings	5 μH
L_{SS}	Mutual inductance between the stator windings	1 μH
M	Mutual inductance between the stator and rotor windings when parallel	4 μH
R_R	Resistance of the rotor winding	2×10^{-2} Ω
R_S	Resistance of the stator windings	1×10^{-3} Ω
J	Inertia of the rotor	3×10^{-2} kg m^2
B	Damping coefficient of the rotor	1×10^{-3} N m s

Table B.2: Governor and exciter controllers for synchronous generator

Symbol	Quantity	Value
ω^{ref}	Reference speed for governor controller	377 rad/sec
K_P	Proportional gain for governor controller	1
K_I	Integral gain for governor controller	20
T_u	Time-constant for the mechanical torque	0.01
T_g	Time-constant for the valve position	0.001
K_t	Gain for the mechanical torque	400
r	Gain for the valve position	200
$v_{Terminal}^{ref}$	Terminal reference voltage for exciter controller	2 V
K_e	Gain for exciter controller	500

Table B.3: Parameters for all three transmission lines

Symbol	Quantity	Value
L_{TL}	Self-inductance of the transmission line	1×10^{-6} H
R_{TL}	Resistance of the transmission line	1×10^{-4} Ω
C_{TL}	Shunt capacitance of the transmission line	1×10^{-2} F

Table B.4: Parameters for both loads

Symbol	Quantity	Value
L_L	Self-inductance of the load	1×10^{-4} H
R_L	Resistance of the load	1×10^{-2} Ω

Table B.5: Parameters for the three wind generators on Bus 2

Symbol	Quantity	Value
L_R	Self-inductance of the rotor windings	2×10^{-5} H
L_{RR}	Mutual inductance between the rotor windings	4×10^{-6} H
L_S	Self-inductance of the stator windings	2×10^{-5} H
L_{SS}	Mutual inductance between the stator windings	2×10^{-6} H
M	Mutual inductance between the stator and rotor windings when parallel	1×10^{-5} H
R_R	Resistance of the rotor winding	2×10^{-3} Ω
R_S	Resistance of the stator windings	1×10^{-3} Ω
J	Inertia of the rotor	4×10^{-5} kg m^2
B	Damping coefficient of the rotor	1×10^{-4} N m s

Table B.6: Parameters for the wind generator on Bus 3

Symbol	Quantity	Value
L_R	Self-inductance of the rotor windings	2×10^{-5} H
L_{RR}	Mutual inductance between the rotor windings	4×10^{-6} H
L_S	Self-inductance of the stator windings	2×10^{-5} H
L_{SS}	Mutual inductance between the stator windings	2×10^{-6} H
M	Mutual inductance between the stator and rotor windings when parallel	1×10^{-5} H
R_R	Resistance of the rotor winding	2×10^{-3} Ω
R_S	Resistance of the stator windings	1×10^{-3} Ω
J	Inertia of the rotor	4×10^{-4} kg m^2
B	Damping coefficient of the rotor	1×10^{-4} N m s

Table B.7: Bus 2 flywheel parameters

Symbol	Quantity	Value
L_{R2}	Self-inductance of the rotor winding	5 μH
L_{S2}	Self-inductance of the stator windings	5 μH
L_{SS2}	Mutual inductance between the stator windings	1 μH
M_2	Mutual inductance between the stator and rotor windings when parallel	4 μH
R_{R2}	Resistance of the rotor winding	2×10^{-3} Ω
R_{S2}	Resistance of the stator windings	1×10^{-3} Ω
V_{R2}	Voltage applied to the rotor winding	1 V
J_2	Inertia of the rotor	1×10^{-4} kg m^2
B_2	Damping coefficient of the rotor	5×10^{-5} N m s
τ_{M2}	Mechanical torque applied to the rotor	0 N m

Table B.8: Bus 3 flywheel parameters

Symbol	Quantity	Value
L_{R2}	Self-inductance of the rotor winding	5 μH
L_{S2}	Self-inductance of the stator windings	5 μH
L_{SS2}	Mutual inductance between the stator windings	1 μH
M_2	Mutual inductance between the stator and rotor windings when parallel	4 μH
R_{R2}	Resistance of the rotor winding	2×10^{-3} Ω
R_{S2}	Resistance of the stator windings	1×10^{-3} Ω
V_{R2}	Voltage applied to the rotor winding	1 V
J_2	Inertia of the rotor	1×10^{-4} kg m^2
B_2	Damping coefficient of the rotor	7×10^{-5} N m s
τ_{M2}	Mechanical torque applied to the rotor	0 N m

Table B.9: Power electronics parameters on both Bus 2 and Bus 3

Symbol	Quantity	Value
C_1	Capacitance of dc-link capacitor	2 F
L_1	Inductance of power electronics inductor	0.01 μH
R_1	Resistance in series with inductor	0.01 mΩ
R_{C1}	Resistance of resistor in parallel with capacitor	25 Ω

Table B.10: Flywheel controller gains on both Bus 2 and Bus 3

Symbol	Quantity	Value
K_P	Proportional gain in the speed controller	0.03
K_I	Integral gain in the speed controller	0.3
K_S	Gain for the flywheel speed set point dynamics	30
ρ	Percent of maximum reference speed $\omega_2^{ref\,max}$ that is desired to obtain	95%

C. Parameters Used in Sao Miguel Power System Example

The parameters used for the three wind generators and the three flywheels in the Sao Miguel power system are given in Table C.1-Table C.4. The parameters for the rest of the system are based on real-world data and are given in [79].

Table C.1: Parameters for the three wind generators

Symbol	Quantity	Value
L_R	Self-inductance of the rotor windings	2 mH
L_{RR}	Mutual inductance between the rotor windings	0.4 mH
L_S	Self-inductance of the stator windings	2 mH
L_{SS}	Mutual inductance between the stator windings	0.2 mH
M	Mutual inductance between the stator and rotor windings when parallel	1 mH
R_R	Resistance of the rotor winding	0.2 Ω
R_S	Resistance of the stator windings	0.1 Ω
J	Inertia of the rotor	15 kg m^2
B	Damping coefficient of the rotor	0.1 N m s

Table C.2: Parameters for three flywheels

Symbol	Quantity	Value
L_{R2}	Self-inductance of the rotor winding	0.5 mH
L_{S2}	Self-inductance of the stator windings	0.5 mH
L_{SS2}	Mutual inductance between the stator windings	0.1 mH
M_2	Mutual inductance between the stator and rotor windings when parallel	0.4 mH
R_{R2}	Resistance of the rotor winding	0.2 Ω
R_{S2}	Resistance of the stator windings	0.1 Ω
V_{R2}	Voltage applied to the rotor winding	1000 V
J_2	Inertia of the rotor	1 kg m^2
B_2	Damping coefficient of the rotor	0.02 N m s
τ_{M2}	Mechanical torque applied to the rotor	0 N m

Table C.3: Power electronic parameters for the three flywheels

Symbol	Quantity	Value
C_1	Capacitance of dc-link capacitor	0.2 F
L_1	Inductance of power electronics inductor	1 μH
R_1	Resistance in series with inductor	1 mΩ
R_{C1}	Resistance of resistor in parallel with capacitor	50 kΩ

Table C.4: Controller gains for the three flywheels

Symbol	Quantity	Value
K_P	Proportional gain in the speed controller	300
K_I	Integral gain in the speed controller	3000
K_S	Gain for the flywheel speed set point dynamics	30
ρ	Percent of maximum reference speed $\omega_2^{ref\,max}$ that is desired to obtain	95%

Bibliography

[1] P. Denholm, E. Ela, B. Kirby, and M. Milligan, "The Role of Energy Storage with Renewable Electricity Generation," National Renewable Energy Laboratory, Technical Report NREL/TP-6A2-47187, January 2010.

[2] M. Cvetkovic, "Power-Electronics-Enabled Transient Stabilization of Power Systems," Carnegie Mellon University, Pittsburgh, Ph.D. Dissertation 2013.

[3] P. Kundur, G. K. Morison, and L. Wang, "Techniques for on-line transient stability assessment and control," in *IEEE Power Engineering Society Winter Meeting*, 2000, pp. 46 - 51.

[4] J. Wen and P. Arons, "Implementation of Centralized Remedial Action Scheme - An Important Step towards WAMPAC," in *IEEE PES General Meeting*, 2011.

[5] M. Ilić and J. Zaborsky, *Dynamics and Control of Large Electric Power Systems*. New York: John Wiley & Sons, 2000.

[6] J. Judson. (2011, June) Beacon Power Corporation Comments to California Public Utilities Commission. [Online]. http://www.cpuc.ca.gov/NR/rdonlyres/706E0452-3533-48FE-ABAC-B49D8D8105ED/0/BeaconPowerpresentationforCPUC62811.pdf

[7] A. Ter-Gazarian, *Energy Storage for Power Systems*.: Institution of Engineering and Technology, 1994.

[8] M. Cvetkovc, K. Bachovchin, and M. Ilic, "Transient Stabilization in Systems with Wind Power," in *Engineering IT-Enabled Sustainable Electricity Services: The Tale of Two Low-Cost Green Azores Islands*.: Springer, 2013, ch. 19.

[9] V. Utkin, J. Guldner, and J. Shi, *Sliding Mode Control in Electromechanical Systems*. London: Taylor & Francis, 1999.

[10] S. Talebi, B. Nikbakhtan, and H.A. Toliyat, "Analytical Model-Based Analysis of High-Speed Flywheel Energy Storage Systems for Pulsed Power Applications," in *Proceedings of ESTS 2009*, Baltimore, MD, 2009.

[11] P. Tsao, "An integrated flywheel energy storage system with homopolar inductor motor/generator and high-frequency drive," University of California Berkeley, Berkeley, CA, Ph.D. dissertation 2003.

[12] K. D. Bachovchin and M. D. Ilić, "Automated Modeling of Power System Dynamics Using the Lagrangian Formulation," *International Transactions on Electrical Energy Systems*, 2014.

[13] S. Banerjee, *Dynamics for Engineers*. London: John Wiley & Sons, 2005.

[14] R. Ortega, A. Loria, P. Nicklasson, and H. Sira-Ramirez, *Passivity-based Control of Euler-Lagrange Systems: Mechanical, Electrical and Electromechanical Applications*. New York: Springer Verlag, 1998.

[15] K. D. Bachovchin and M. D. Ilić, "Automated Modular Approach to Common Information Modeling of Large-Scale Power System Dynamics and Control," Carnegie Mellon University, EESG Working Paper No. R-WP-2-2014 2014.

[16] K. D. Bachovchin and M. D. Ilić, "Automated Computer-Aided Symbolic Derivation of Passivity-Based Control Law for Electrical Systems and Demonstration on Three-Phase AC/DC/AC Converter," Carnegie Mellon University, EESG Working Paper No. R-WP-5-2014 August 2014.

[17] K. D. Bachovchin and M. D. Ilić, "Passivity-Based Control Using Three Time-Scale Separations of Variable Speed Drives for Flywheel Energy Storage Systems," Carnegie Mellon University, EESG Working Paper No. R-WP-6-2014 2014.

[18] D. Zhu, "Multi - Timescale Control of Energy Storage Enabling the Integration of Variable Generation," Carnegie Mellon University, Ph.D. Dissertation 2014.

[19] Q. Liu, M. Cvetkovic, and M. Ilic, "Stabilization and Regulation of Small Frequency Fluctuations by Means of Governor and Flywheel Control," in *Engineering IT-Enabled Sustainable Electricity Services: The Tale of Two Low-Cost Green Azores Islands*.: Springer, 2013, ch. 15.

[20] K. D. Bachovchin and M. D. Ilić, "Transient Stabilization of Power Grids Using Passivity-Based Control with Flywheel Energy Storage Systems," in *IEEE Power & Energy Society General Meeting*, Denver, 2015.

[21] D. Jeltsema and J.M.A. Scherpen, "Multidomain modeling of nonlinear networks and systems," *IEEE Control Systems*, vol. 29, no. 4, pp. 28-59, Aug. 2009.

[22] K. D. Bachovchin, J. F. Hoburg, and R. F. Post, "Magnetic Fields and Forces in Permanent Magnet Levitated Bearings," *IEEE Transactions on Magnetics*, vol. 48, no. 7, pp. 2112-2120, July 2012.

[23] K. D. Bachovchin, J. F. Hoburg, and R. F. Post, "Stable Levitation of a Passive Magnetic Bearing," *IEEE Transactions on Magnetics*, vol. 49, no. 1, pp. 609-617, Jan. 2013.

[24] K.D. Bachovchin, "Magnetic Fields and Forces in an Ambient Temperature Passive Magnetically Levitated Bearing System," Carnegie Mellon University, Pittsburgh, PA, M.S. dissertation 2011.

[25] K. D. Bachovchin and M. D. Ilic, "Centralized Automated Dynamic Model Derivation for Electric Circuits and Power Systems using the Lagrangian and Hamiltonian Approaches," provisional patent application, April 2013.

[26] G. J. Sussman, J. Wisdom, and M. E. Mayer, *Structure and Interpretation of Classical Mechanics*.: MIT Press, 2001.

[27] K. D. Bachovchin and M. D. Ilić, "Automated Modeling of Electric Circuit Dynamics Using the Lagrangian and Hamiltonian Formulations," Carnegie Mellon University, EESG Working Paper No. R-WP-1-2013 2013.

[28] J.M.A. Scherpen, D. Jeltsema, and J.B. Klaassens, "Lagrangian modeling of switching electrical networks," *Systems & Controls Letters*, vol. 48, no. 5, pp. 365-374, 2003.

[29] L.O. Chua and J. McPherson, "Explicit topological formulation of Lagrangian and Hamiltonian equations for nonlinear networks," *IEEE Transactions on Circuits and Systems*, vol. 21, no. 2, pp. 277-286, March 1974.

[30] J. Attia, *PSPICE and MATLAB for Electronics: An Integrated Approach*.: CRC Press LLC, 2002.

[31] J. Zhang, "Research on Flywheel Energy Storage System Using in Power Network," in *International Conference on Power Electronics and Drives Systems*, 2005, pp. 1344-1347.

[32] R. Takahashi and J. Tamura, "Frequency Stabilization of Small Power System with Wind Farm by Using Flywheel Energy Storage System," in *IEEE International Symposium on Diagnostics for Electric Machines, Power Electronics and Drives*, 2007, pp. 393-398.

[33] N. Hamsic et al., "Increasing Renewable Energy Penetration in Isolated Grids Using a Flywheel Energy Storage System," in *International Conference on Power Engineering, Energy and Electrical Drives*, 2007, pp. 195-200.

[34] S.A Belfedhal, S. Kouadria, E. Berkouk, and Y. Meslem, "Flywheel energy storage system with induction machine associated to a variable-speed wind generator," in *8th International Conference and Exhibition on Ecological Vehicles and Renewable Energies (EVER)*, 2013, pp. 1-6.

[35] T. Kailath, *Linear Systems*. New Jersey: Prentice Hall, 1980.

[36] H. Kwakernaak and R. Sivan, *Linear Optimal Control Systems*. New York: Wiley Interscience, 1972.

[37] R. A. Layton., *Principles of Analytical System Dynamics*. New York: Springer, 1998.

[38] H. H. Woodson and J. R. Melcher, *Electromechanical Dynamics, Part I: Discrete Systems*. New York: Wiley, 1968.

[39] K. S. Suresh Kumar, *Electric Circuits and Networks*. India: Pearson Education, 2009.

[40] P.T. Krein, J. Bentsman, R.M. Bass, and B.C Lesieutre, "On the use of averaging for the analysis of power electronic systems," *IEEE Transactions on Power Electronics*, vol. 5, no. 2, pp. 182-190, April 1990.

[41] T.S. Lee, "Lagrangian modeling and passivity-based control of three-phase AC/DC voltage-source converters," *IEEE Transactions on Industrial Electronics*, vol. 51, no. 4, pp. 892-902, Aug. 2004.

[42] G. Verghese, M. Ilic-Spong, and J. Lang, "Modeling and Control Challenges in Power Electronics," in *Proceedings of the 25th IEEE Conference on Decision and Control*, Athens, Greece, 1986, pp. 39-45.

[43] A. Fitzgerald, C. Kingsley Jr., and S. Umans, *Electric Machinery*. Piscataway, NJ: McGraw-Hill, 2003.

[44] J. H. Lang, G. C. Verghese, and M. D. Ilic, "Electrical Machine Systems: Dynamics, Estimation, and Control," MIT, Cambridge, MA, Lecture Notes 2005.

[45] V. Staudt, "AC machine dynamics described by space vectors using state-space notation," *European Transactions on Electrical Power*, vol. 9, no. 1, pp. 17-25, 1999.

[46] P. M. Anderson and A. A. Fouad, *Power System Control and Stability*. India: IEEE Press, 2003.

[47] P. C. Krause, O. Wasynczuk, and S.D. Sudhoff, *Analysis of Electric Machinery and Drive Systems John Wiley & Sons, 2002*. India: John Wiley & Sons, 2002.

[48] D. C. White and H. H. Woodson, *Electromechanical Energy Conversion*. New York: John Wiley & Sons, 1959.

[49] R. D. Robinett and D. G. Wilson, *Nonlinear Power Flow Control Design Utilizing Exergy, Entropy, Static and*

Dynamic Stability, and Lyapunov Analysis. London: Springer-Verlag , 2011.

[50] R. F. Post, "An Improved Electrostatic Generator/Motor," U.S. Patent 7,834,513, Nov. 16, 2010.

[51] K. D. Bachovchin, M. Cvetkovic, and M. D. Ilic, "Automated Modular Derivation of Electric Energy System Dynamics for Power System Control," provisional patent application, April 2013.

[52] I.A. Hiskens and P.J. Sokolowski, "Systematic modeling and symbolically assisted simulation of power systems," *IEEE Transactions on Power Systems*, vol. 16, no. 2, pp. 229-234, May 2001.

[53] M.A. Pai, *Power Circuits and Electromechanics*. Champaign: Stipes Publishing L.L.C., 2007.

[54] G. Abad, J. López, M. Rodríguez, L. Marroyo, and G. Iwanski, *Doubly Fed Induction Machine: Modeling and Control for Wind Energy Generation*.: Wiley-IEEE Press, 2011.

[55] P. Kundur, *Power System Stability and Control*. New York: McGraw-Hill, 1994.

[56] A. Bergen and V. Vittal, *Power Systems Analysis*.: Prentice Hall, 1999.

[57] K. D. Bachovchin and M. D. Ilić, "Automated and Distributed Modular Modeling of Large-Scale Power System Dynamics," Carnegie Mellon University, Pittsburgh, EESG Working Paper No. R-WP-8-2014 2014.

[58] S. Fukuda, "LQ control of sinusoidal current PWM rectifiers," *IEE Proceedings - Electric Power Applications*, vol. 144, no. 2, pp. 95-100, March 1997.

[59] V. Blasko and V. Kaura, "A new mathematical model and control of a three-phase AC-DC voltage source converter," *IEEE Transactions on Power Electronics*, vol. 12, no. 1, pp. 116-123, Jan 1997.

[60] H. Komurcugil and O. Kukrer, "Lyapunov-based control for three-phase PWM AC/DC voltage-source converters," *IEEE Transactions on Power Electronics*, vol. 13, no. 5, pp. 801-813, Sept. 1998.

[61] D.C Lee, G.M. Lee, and K.D. Lee, "DC-bus voltage control of three-phase AC/DC PWM converters using feedback linearization," *IEEE Transactions on Industry Applications*, vol. 36, no. 3, pp. 826-833, May 2000.

[62] H. Sira-Ramírez and R. Ortega, "Passivity-based controllers for the stabilization of DC-to-DC power converters," in *Proceedings of the 34th IEEE Conference on Decision and Control*, 1995, pp. 3471-3476.

[63] D. Jeltsema, "Modeling and control of nonlinear networks: a power-based perspective," Delft University of Technology, Ph.D. dissertation 2005.

[64] D. del Puerto-Flores et al., "Passivity-Based Control by Series/Parallel Damping of Single-Phase PWM Voltage Source Converter," *IEEE Transactions on Control Systems Technology*, vol. 22, no. 4, pp. 1310-1322, July 2014.

[65] R. Ortega and G. Espinosa, "Torque regulation of induction motors," *Automatica*, vol. 29, no. 3, pp. 621-633, 1993.

[66] J. Linares-Flores, J. Reger, and H. Sira-Ramírez, "Load Torque Estimation and Passivity-Based Control of a Boost-Converter/DC-Motor Combination," *IEEE Transactions on Control Systems Technology*, vol. 18, no. 6, pp. 1398-1405, Nov. 2010.

[67] R. Ortega, A. van der Schaft, and I. Mareels, "Energy shaping control revisited," in *Advances in the Control of Nonlinear Systems*.: Springer-Verlag London, 2001, pp. 277-307.

[68] R. Ortega, A. van der Schaft, B. Maschke, and G. Escobar, "Interconnection and damping assignment passivity-based control of port-controlled Hamiltonian systems," *Automatica*, vol. 38, no. 4, pp. 586-596, 2002.

[69] J. Slotine and W. Li, *Applied Nonlinear Control*.: Prentice-Hall, 1991.

[70] N. C. Rana and P. S. Joag, *Classical Mechanics*.: Tata McGraw-Hill Publishing Company, 1991.

[71] D. Neascu, "Space Vector Modulation - An Introduction," in *27th Annual IEEE Industrial Electronics Society Conference*, 2001, pp. 1583-1592.

[72] M.M. Flynn, P. McMullen, and O. Solis, "High-Speed Flywheel and Motor Drive Operation for Energy Recovery in a Mobile Gantry Crane," in *Twenty Second Annual IEEE Applied Power Electronics Conference*, 2007, pp. 1151-1157.

[73] H. Akagi, E. Watanabe, and M. Aredes, *Instantaneous power theory and applications to power conditioning*.: Wiley-IEEE Press, 2007.

[74] A. von Meier, *Electric Power Systems: A Conceptual Introduction*.: Wiley-IEEE Press, 2006.

[75] F. W. Grover, *Inductance Calculations*.: Dover Publications, 2004.

[76] D. Cheng, *Field and Wave Electromagnetics*.: Addison-Wesley, 1989.

[77] P. Scherz, *Practical electronics for inventors*. New York: McGraw-Hill, 2007.

[78] V. K. Mehta and R. Mehta, *Basic Electrical Engineering*.: S. Chand Publishing, 2008.

[79] M. Ilic, L. Xie, and Q. Liu, *Engineering IT-Based Electricity Services of the Future: The Tale of Two Low-cost Green Azores Islands*.: Springer, 2013.

[80] N. Awofeso, "Generator Diesel Exhaust: a Major Hazard to Health and the Environment in Nigeria," *American Journal of Respiratory and Critical Care Medicine*, vol. 183, no. 10, p. 1437, 2011.

[81] S. Earnshaw, "On the Nature of the Molecular Forces which Regulate the Constitution of the Luminiferous Ether," *Trans. Cambridge Phil. Soc.*, vol. 7, pp. 97-112, 1842.

[82] B. R. Weinberger, L. Lynds, J. R. Hull, and U. Balachandran, "Low friction in high temperature superconductor bearings," *Applied Physics Letters*, vol. 59, pp. 1132-1134, 1991.

[83] R. F. Post and D. D. Ryutov, "Ambient-Temperature Passive Magnetic Bearings: Theory and Design Equations," in *Proceedings of the Sixth International Symposium on Magnetic Bearings*, 1998, pp. 110-122.

[84] R. Ravaud, G. Lemarquand, V. Lemarquand, and C. Depollier, "Analytical calculation of the magnetic field created by permanent-magnet rings," *IEEE Transactions on Magnetics*, vol. 44, no. 8, pp. 1982-1989, Aug. 2008.

[85] E. P. Furlani, S. Reznik, and A. Kroll, "A three-dimensional field solution for radially polarized cylinders ," *IEEE Transactions on Magnetics*, vol. 31, no. 1, pp. 844–851, Jan. 1995.

[86] J. F. Hoburg, "Modeling Maglev Passenger Compartment Static Magnetic Fields From Linear Halbach Permanent-Magnet Arrays," *IEEE Transactions on Magnetics*, vol. 40, no. 44, Jan. 2004.